

Λ Polarization in Lead-Lead Collisions

Cover: 'Visitation' of Domenico Ghirlandaio (1486-1490), Fresco in the Capella Tornabuoni, Santa Maria Novella, Florence.

© Copyright Eelco Schillings

Λ Polarization in Lead-Lead Collisions

Λ Polarisation in Lood-Lood Botsingen

(met een samenvatting in het Nederlands)

Proefschrift

TER VERKRIJGING VAN DE GRAAD VAN DOCTOR
AAN DE UNIVERSITEIT UTRECHT
OP GEZAG VAN DE RECTOR MAGNIFICUS, PROF. DR. W.H. GISPEN,
INGEVOLGE HET BESLUIT VAN HET COLLEGE VOOR PROMOTIES
IN HET OPENBAAR TE VERDEDIGEN OP
WOENSDAG 28 MEI 2003 DES OCHTENDS TE 10.30 UUR

DOOR

Eelco Schillings

GEBOREN OP 24 MEI 1973, TE MAASTRICHT

promotoren: **Prof. Dr. R. Kamermans**
Faculteit Natuur- & Sterrenkunde
Universiteit Utrecht

copromotor: **Dr. P.G. Kuijer**
Nationaal Instituut voor Kernfysica en
Hoge-Energiefysica, Amsterdam

Dit werk is een onderdeel van het onderzoeksprogramma van de “Stichting voor Fundamenteel Onderzoek der Materie” (FOM), financieel gesteund door de “Nederlandse Organisatie voor Wetenschappelijk Onderzoek” (NWO).

Contents

1	Introduction	1
1.1	Transverse Hyperon Polarization	2
1.2	Strangeness enhancement in the NA57 experiment	4
1.3	Purpose of this thesis	6
1.4	Outline of this thesis	7
2	Theory	9
2.1	Perturbative QCD based model	10
2.2	Semi-classical models	12
2.2.1	The Thomas Precession model	13
2.2.2	The Berlin model	15
2.2.3	The Troshin-Tyurin model	17
2.3	Polarization in Heavy Ion collisions	19
2.3.1	Transverse polarization	19
2.3.2	Longitudinal polarization	21
2.4	Summary	21
3	Experimental Setup	25
3.1	The SPS accelerator	26
3.2	The NA57 Experiment	26
3.2.1	Collision systems	29
3.2.2	Trigger	30
3.2.3	Multiplicity Strip Detector	31
3.2.4	Silicon Telescope	31
4	Track Reconstruction	39
4.1	Track reconstruction in ORHION	40
4.1.1	Track recognition: the ST-processor	42
4.1.2	The track improvement: the XC-processor	43
4.1.3	Reconstruction of V^0 candidates: the V0 processor	44
4.2	The micro-strips in the reconstruction software	44
4.2.1	Hit reconstruction	44
4.2.2	The hit assignment algorithm	48
4.2.3	Track extrapolation results	50

4.2.4	Reconstruction efficiencies	60
5	Reconstruction of Λ, $\bar{\Lambda}$ and K_S^0 particles	63
5.1	V^0 selection procedure	64
5.1.1	Variables of a V^0 decay	64
5.1.2	Particle identification	66
5.2	Final selection results	68
5.2.1	The Pb-Pb data at 158 AGeV/c taken in 1998.	68
5.2.2	The Pb-Pb data at 40 AGeV/c taken in 1999.	72
5.2.3	The Pb-Pb data at 158 AGeV/c taken in 2000.	76
6	Data Analysis	83
6.1	Weighting procedure	84
6.2	Deconvolution	85
6.2.1	Discretization	86
6.2.2	Unfolding without regularization	87
6.2.3	Unfolding with regularization	89
6.3	Determination of the centrality	91
6.4	Monte Carlo input for the unfolding	92
6.4.1	Simulation results	94
7	Inverse slopes and yields	103
7.1	Deconvolution procedure	104
7.1.1	Discretization	104
7.1.2	Bin definition	106
7.1.3	Stability check	108
7.2	Inverse slopes	108
7.2.1	Inverse slope parameters as function of centrality	110
7.3	Yields	114
8	Polarization	119
8.1	Deconvolution procedure	120
8.1.1	Angular distributions	120
8.1.2	Deconvolution	122
8.2	K_S^0 polarization	123
8.2.1	Transverse polarization	124
8.2.2	Longitudinal polarization	126
8.3	Λ and $\bar{\Lambda}$ polarization	126
8.3.1	Transverse polarization	128
8.3.2	Systematic effects	135
8.3.3	Longitudinal polarization	142
8.4	Conclusion	144
A	Appendix	147
	Bibliography	151

Contents	vii
Summary	157
Samenvatting	159
Dankwoord	161
Curriculum Vitae	163

1

Introduction

In 1976 a remarkable discovery was done at FNAL in the measurement on the production of Λ particles. In p-Be reactions at a proton beam of 300 GeV/c a large polarization was found perpendicular to the production plane for the produced Λ hyperons [1]. This effect, which is called transverse Λ polarization, was unexpected since it is reasonable to assume that in the collision of two unpolarized objects, the produced particles originate from different inelastic channels, which should have random magnitudes and signs. Consequently the inclusive reaction, a combination of all channels summed, should give an average zero result. Because of this puzzling behavior, the transverse Λ polarization has been occupying experimentalists and theorists for the last two decades. Nowadays a large amount of significant polarization data has been collected, as well in meson induced reactions as in hadron and nucleus induced reactions. Nevertheless the origin of the effect has not been uncovered. In this thesis the polarization of the Λ hyperons will be investigated for a completely new type of reaction. This will be done by using the data of Pb-Pb collisions at a beam energy of 158 AGeV/c collected by the NA57 experiment. This experiment aims to investigate the production of particles containing strange quarks (called hyperons) in heavy ion collisions. In this chapter an overview of the characteristics of the Λ polarization will be given in section 1.1 and furthermore the NA57 experiment will be introduced (section 1.2). Then the purpose of this thesis will be given (section 1.3). The last section consists of the outline of this thesis.

1.1 Transverse Hyperon Polarization

The transverse polarization of the Λ has been measured to be dependent on the transverse momentum (p_T) and the *Feynman-x* (x_F) of the produced Λ . The latter kinematic variable is defined as $x_F \equiv \frac{2p_L^{cms}}{\sqrt{s}}$ where p_L^{cms} is the momentum of the Λ in the direction of the projectile in the center of mass of the collision system and \sqrt{s} is the energy of a single nucleon in the beam. Hence this quantity gives information about the fraction of the original momentum of the projectile which is transferred to the produced Λ .

The dependence of the transverse Λ polarization on the transverse momentum can be seen in figure 1.1. In this overview results for both p-p [2] and p-Be [3] collisions are depicted and for each system the p_T -dependence for different regions of x_F are given. The polarization with respect to p_T can be characterized to show the following behavior:

- The transverse polarization is negative with respect to the production plane, i.e. $\vec{n} = \vec{p}_{beam} \times \vec{p}_\Lambda$.
- For $p_T < 1$ GeV/c the polarization increases linearly with p_T . The slope is dependent on x_F .
- For $p_T > 1$ GeV/c the polarization seems constant with p_T and is only dependent on x_F . The magnitude of the polarization is measured to be independent of p_T up to 3.5 GeV/c [3].

As can be seen from the p_T dependence, the x_F of the Λ is also a relevant variable for the polarization. When only the data are considered for $p_T > 1$ GeV/c, which is the region where the p_T dependence is flat, the dependence of the transverse polarization on x_F also has been determined. In figure 1.2 part of the data shown before and also data from p-Pb [4], p-Be at another beam energy of 800 GeV/c [3] and Au-Au collisions [5] are depicted.

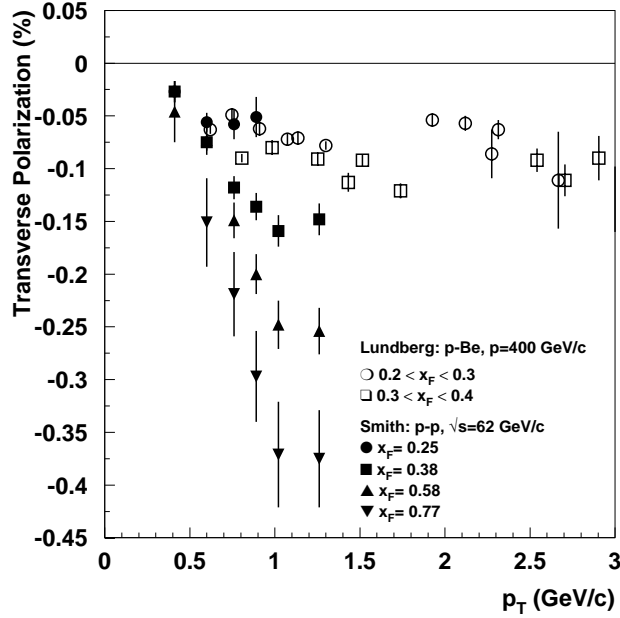


Figure 1.1: The dependence of the transverse Λ polarization on transverse momentum p_T . The data shown are from [2] and [3].

The behavior of the polarization with respect to x_F has the following characteristics:

- The polarization increases almost linearly with x_F .
- The polarization is almost independent on beam energy.
- The polarization is almost independent on the type of collision system.

The polarization effect is the largest at large x_F and can reach values of 40% there. In exclusive reactions like $pp \rightarrow p(\Lambda K^+)$ the polarization has been measured to be even of the order of -60% [6], which is an indication that spin effects are dominant in the production of particles in this range. Also for other hyperons the polarization has been determined (for an extensive overview of polarization effects for different hyperons and different collision systems see [7] and [8]): the transverse polarization of Σ^\pm is of the same order but of opposite sign, while the Ξ^- and Ξ^0 polarizations are of the same sign. In contrast to what is seen for the Λ , the polarization for the Σ^+ decreases with x_F while the polarization of the Ξ 's is x_F independent. The polarization of the anti-particles of the Λ and Ξ^0 is zero which led to the belief that polarization only arises when a hyperon is formed as a fragment of the incoming proton. However, for other anti-particles this is not the case: $P_{\Xi^+} \sim P_{\Xi^-}$ and $P_{\Sigma^-} \sim P_{\Sigma^+}$. This behavior of hyperon polarization is very puzzling and with the recent discovery of large polarization effects in heavy ion collisions [5] a new physics window was opened to investigate this effect.

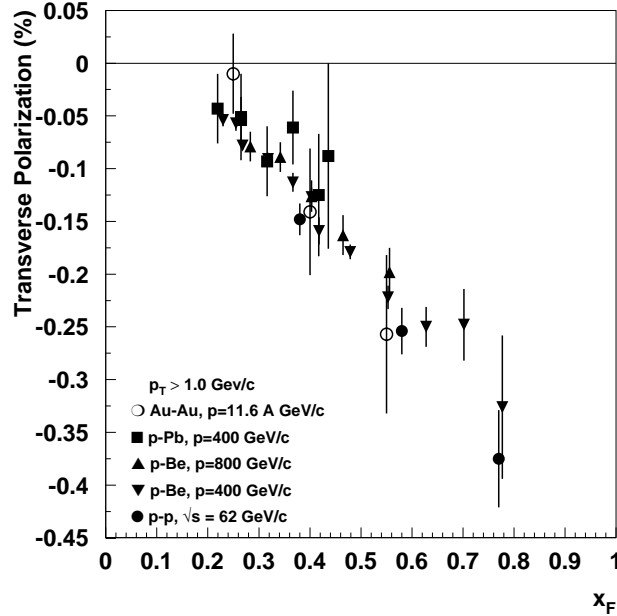


Figure 1.2: The dependence of the transverse Λ polarization on x_F . The data shown are from [2]- [5].

Relativistic heavy ion collisions are a good tool to investigate the creation of a new state of matter: the Quark Gluon Plasma (QGP). This state can be created by a phase transition from hadronic matter when this is heated and/or compressed. This process can be compared with phase transitions like that from ice to water and water to steam. In normal hadronic matter quarks and gluons are held together by the strong force, which becomes asymptotically large when quarks are pulled away from each other. Only at conditions where large energy densities occur the boundaries between individual particles may disappear and the quarks and gluons are expected to move around freely. This condition is thought to be reached in the collision of two heavy ions, where at the impact of the nucleons the matter is compressed and the kinetic energy is converted into heat.

One of the probes proposed for the investigation of the creation of the QGP is *Strangeness Enhancement* and the measurement of this effect is the main goal of the NA57 experiment. The data of this experiment are analyzed in this thesis and therefore in the next section this experiment is introduced.

1.2 Strangeness enhancement in the NA57 experiment

In the WA97 experiment, the predecessor of NA57, the production of strange and multi-strange particles around mid-rapidity at a beam energy of 158 GeV/c per nucleon has been studied. The

rapidity variable y is the longitudinal variable defined as:

$$y = \frac{1}{2} \ln \frac{E + p_l}{E - p_l}, \quad (1.1)$$

where E is the energy and p_l is the longitudinal component of the momentum. Mid-rapidity refers to the rapidity region which corresponds to the center of mass of the system. It was measured that the production of strange hadrons in Pb-Pb collisions was enhanced with respect to proton induced reactions (p-Be and p-Pb) [9]. This effect is called *Strangeness Enhancement* and was predicted to be a signature of a QGP [10].

The NA57 experiment extends the scope of WA97 [11]. In order to study the evolution of the strangeness enhancement pattern as a function of the beam energy NA57 has measured strangeness production at both 40 AGeV/c and 158 AGeV/c. Furthermore it aims to investigate the dependence of the enhancement on the interaction volume by increasing the centrality range, resulting in a lower limit of 50 wounded nucleons, while WA97 could only measure down to 100. The word *centrality* denotes a measure of the type of collision, which ranges from peripheral (glancing collisions) to central (head-on collisions). The wounded nucleons are those nucleons which undergo at least one primary inelastic collision with another nucleon and they are a good reference for the centrality of the collision. The determination of the number of wounded nucleons of the reaction will be described in section 6.3.

The analysis of the first run taken in 1998, Pb-Pb collisions at 158 AGeV/c, has confirmed the

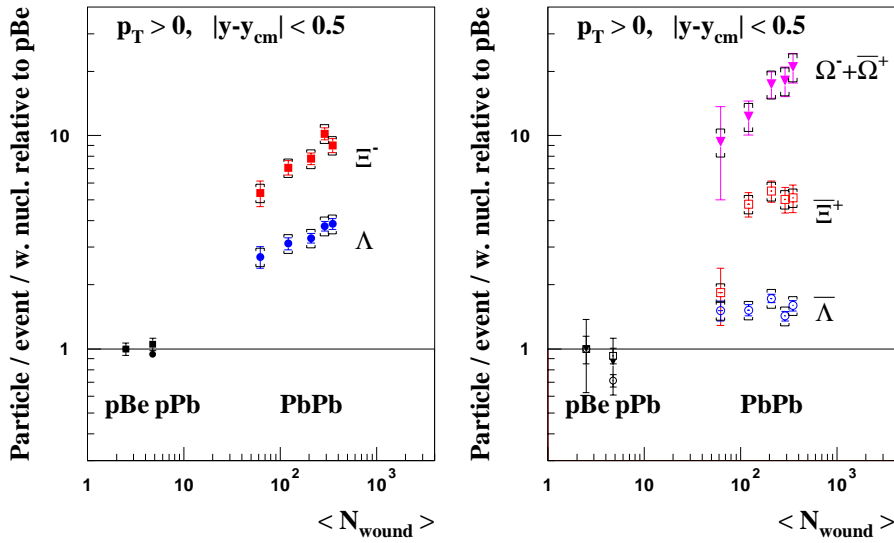


Figure 1.3: Yield per event divided by $\langle N_{wound} \rangle$ and relative to p-Be interactions as a function of the number of wounded nucleons. To the left the relative yields are depicted for the particles which have at least one valence quark in common with the incoming nucleons. The plot to the right shows the particles which have no valence quark in common.

results from WA97. In figure 1.3 the yield per event divided by the number of wounded nucleons relative to the p-Be yield is plotted against the average number of wounded nucleons $\langle N_{wound} \rangle$. At the lower scale the relative yield for the proton induced reactions are depicted. The average number of wounded nucleons in the p-Be and p-Pb systems are equal to 2.5 and 4.75 respectively. At the higher scale the results from the Pb-Pb are plotted and they are divided in five centrality dependent samples: the most central events have an average of around 400 wounded nucleons and the most peripheral events are characterized by around 60 wounded nucleons. The four most central samples were also used in WA97, where the most peripheral sample is the new contribution from NA57. The plot shows that the production of hyperons is enhanced with respect to the proton induced reactions:

$$E(\Lambda) < E(\Xi) < E(\Omega) ,$$

in which E is the value of the enhancement. The number of strange quarks contained by the hyperons increases from one in the Λ to three in the Ω . For the Ω the enhancement amounts to a factor 15 with respect to the linearly scaling of the particle production with the number of wounded nucleons. This linearly scaling is shown to occur for particles which contain no strange quarks like pions [12]. The enhancements measured for the new centrality sample seem to be related to the more central samples by a power law and only the Ξ result shows a significant change. This kind of threshold effect could be an indication that in the peripheral collision the interaction region is too small to create a QGP. Since this threshold effect is not seen for the other particles it is difficult to draw conclusions. Therefore it is interesting to see the results from the 40 AGeV/c runs. At a lower beam momentum the energy input could also be too small for the creation of a QGP. The enhancement analysis at this lower energy is not yet completed.

1.3 Purpose of this thesis

In addition to looking at strangeness enhancement it is interesting to investigate for the 1998 data another proposed signature of the QGP: the disappearance of transverse Λ polarization around mid-rapidity [13]. This is because in a QGP the memory of the direction and polarization of quarks is erased. By measuring at mid-rapidity only processes from the interaction region are considered and no influence from the fragmentation region is expected. However, near mid-rapidity (which corresponds to $x_F \sim 0$) the polarization should vanish also for proton induced collisions. This can be seen from the symmetry argument which states that the magnitude of the transverse polarization is asymmetric in x_F : $P(x_F) = -P(-x_F)$ and hence $P(0) = 0$. Therefore it is more interesting to do a measurement in the region between mid-rapidity and the fragmentation region ($x_F \sim 0.15$): the polarization still has some (small) value and one can still hope to look directly at the interaction region. The measurement of the transverse Λ polarization in this intermediate region is the goal of this thesis. In this way it can be investigated whether the system size, combined with the high beam energy has an influence on the transverse polarization and whether information of the incoming projectile is lost. Although the effect is small (of the order of 5%) this may be counterbalanced by the large statistics of the Λ sample. Furthermore the division of the data in centrality samples enables to look at the polarization as a function of centrality. In addition to the determination of the transverse polarization also the longitudinal polarization will be looked at. A measurement of the longitudinal polarization could say something about the feed-down of (anti)- Ξ s in our sample of Λ s.

1.4 Outline of this thesis

This thesis is devoted to the determination of the transverse Λ polarization around mid-rapidity in Pb-Pb collisions at $158 A\text{GeV}/c$. In order to explain the transverse polarization of Λ hyperons in hadronic reactions several theoretical models have been proposed. In chapter 2 an overview of the models is given. The data used in this thesis were taken with the NA57 experimental setup, which is described in chapter 3. The event reconstruction is discussed in the next chapters. It is divided in two parts: the track reconstruction (chapter 4) and the particle recognition (chapter 5). In these chapters also the influence of the Silicon Strip detectors, developed by the institute of Subatomic Physics at Utrecht University/NIKHEF, on the reconstruction results is shown. The data have to be corrected for detector effects and in this thesis the deconvolution method described by Blobel [14] is used. The description of this method is given in chapter 6. This method is first applied to the determination of the inverse slopes and yields (chapter 7) and finally the results of the polarization analysis are presented in chapter 8.

2

Theory

Since the discovery of a large transverse Λ polarization in p-Be reactions at a proton beam energy of 300 GeV/c at FNAL in 1976 [1], many models have been proposed to explain this effect. Since then the data set on hyperon polarization has been expanded seriously and in parallel also the number of theoretical models has been increasing. From the semi-classical models, proposed in the beginning, like the LUND model [25] and the Grand-Mietinen model [26], the focus has changed to more complicated quantum mechanical models. This last shift has also been influenced by the recent discovery of large left-right asymmetries in pion production in experiments with polarized proton beams [15]. These large asymmetries found in meson and hyperon production were thought to have a common origin and therefore new models have been put forward which tried to explain all these effects together. Some good reviews of the currently available models have been published recently [16,17,18,19].

In the next sections different models explaining the transverse Λ polarization are described: first the result from straightforward pQCD calculations is given (section 2.1) after which semi-classical models are discussed (section 2.2). The influence of the creation of a QGP on the polarization is discussed in section 2.3. Finally a summary of all the models and their relevance for the analysis done here is given in section 2.4.

2.1 Perturbative QCD based model

In order to explain polarization effects in hyperon production, the most reasonable approach is to make use of perturbative QCD calculations, which have been able to describe the unpolarized cross-sections of meson and hyperon production in hadron-hadron collisions very well. It has been shown in the past that for high p_T particles and jets the inclusive cross section for hadron production can be factorized [20]. This results in a convolution of three components: the momentum distribution functions of the constituents (quarks, anti-quarks, gluons) in the colliding hadrons; the cross-section for the elementary hard scattering between the constituents of the two colliding hadrons; and the fragmentation function of the scattered constituent. If one considers the process $A + B \rightarrow C + X$, shown in figure 2.1, the cross section can be written schematically as

$$\sigma_{A+B \rightarrow C} = \sum_{abcd} \phi_{a/A}(x_a) \otimes \phi_{b/B}(x_b) \otimes \hat{\sigma}_{a+b \rightarrow cd} \otimes D_{c \rightarrow C}(z), \quad (2.1)$$

where \sum_{abcd} represents the sum over the parton flavor of the quarks, anti-quarks and gluons involved. The functions $\phi_{a/A}(x_a)$ and $\phi_{b/B}(x_b)$ are the parton distribution functions of the constituent a in hadron A and that of b in B , where x_a and x_b are the momentum fractions of the hadron carried by the constituents. The cross-section $\hat{\sigma}_{a+b \rightarrow c}$ is the elementary scattering process $a + b \rightarrow c + d$, which can be calculated by perturbative QCD. Finally $D_{c \rightarrow C}$ is the fragmentation function which describes the fragmentation of parton c into hadron C , where z is the momentum fraction of c obtained by C . One must take into account that pQCD calculations are only valid for processes with a high momentum transfer and thus cover the region of high p_T ($p_T > 5$ GeV/c) and in the following a large value of p_T is assumed.

The transverse polarization of the final particle C can be calculated from the polarized cross sections $\sigma_{A+B \rightarrow C^\uparrow}$ and $\sigma_{A+B \rightarrow C^\downarrow}$ by the following equation:

$$P_C = \frac{d\sigma_C^\uparrow - d\sigma_C^\downarrow}{d\sigma_C^\uparrow + d\sigma_C^\downarrow} \quad (2.2)$$

Using the general optical theorem this yields for the polarization [16]:

$$P_C \propto \Im(F_{nf} F_f^*) \quad (2.3)$$

where F_{nf} is the amplitude for the forward helicity non-flip process $ab\bar{c}_\lambda \rightarrow ab\bar{c}_\lambda$, with $\lambda = \pm$ on both sides. The amplitude F_f is the forward helicity flip amplitude $ab\bar{c}_\lambda \rightarrow ab\bar{c}_{-\lambda}$. To get a non-zero polarization it is necessary that the helicity flip amplitude is non-zero and that the phases of helicity flip F_f and non-flip F_{nf} are different. If the transverse spin asymmetry is related to the initial spin of the particles A or B it is called the analyzing power (A_N).

For the explicit calculation of the polarization from the factorized cross sections the three factors, which have to be convoluted, must be taken into account. If one makes the following assumptions:

- the distribution functions of the constituents in the nucleon are assumed to be symmetric in intrinsic transverse motion and not to be dependent on k_T , and
- the fragmentation function is independent of the spin of the quarks,

the polarization can only originate from the elementary scattering process.

The effect of this process on the transverse polarization has been determined by Kane, Pumplin and Repko [21] by the following argument. When the particles are massless, helicity is conserved and the helicity flip amplitude must be zero. In the case the mass is non-zero the flip amplitude is proportional to the mass and because in the Born approximation the amplitudes are real, the imaginary part can only be produced by a one-loop diagram. This introduces the coupling constant α_s , and results in the following relation for the polarization:

$$P_C \propto \frac{\alpha_s m_q}{\sqrt{s}} \quad (2.4)$$

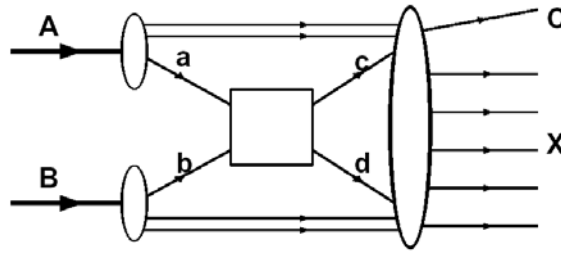


Figure 2.1: Schematic illustration of factorization theorem in $A + B \rightarrow C + X$. The square in the center of the figure represents the elementary process $a + b \rightarrow c + d$, which can be calculated using perturbative QCD.

Since we are considering hard processes which have a large value for \sqrt{s} (and also $p_T \sim \sqrt{s}$, the small values for the current quark mass m_q and α_s result in a vanishing polarization. This is in disagreement with the data, which show that the polarization persists at high p_T (see for example [3]).

One of the problems arising from the approach used above is that it only can be applied for the hard scattering region which encompasses the kinematical region of high p_T and $x_F \sim 0$. The variable $x_F = \frac{2p_L^G}{\sqrt{s}}$ is the fraction of the beam momentum carried by the Λ in its center of mass frame in the longitudinal direction. However, the highest polarization effects have been measured in the beam fragmentation region ($x_F > 0.3$ and moderate p_T), which is connected with lower momentum transfer and is dominated by 'soft' processes. Therefore modifications to the hard scattering scheme were proposed in order to be able to take into account the large asymmetries found: higher twist parton distributions [22] and spin dependent fragmentation functions [23]. The first modification shows no agreement with the data and the latter modification has to cope with other problems: measurements of transverse Λ polarization in e^+e^- annihilation in hadrons have shown that the polarization is consistent with zero [24]. In this case only fragmentation effects contribute and this indicates that the spin dependence of fragmentation functions is weak.

Another argument against these modifications is that they are put in by hand, which is unsatisfactory for the physical understanding of the polarization effects. Therefore another approach would be to consider more phenomenological models, which are described in the next section.

2.2 Semi-classical models

In all the following models the static quark model is used for explaining the transverse Λ polarization. This assumes that Λ s are built up from the SU(6) wave function. It can be produced by replacing an u-quark of the incoming proton with an s-quark from the sea of the target. The remnant ud-diquark of the proton is assumed to be in the spin-zero state ($I=S=0$), which implies that the spin of the Λ is determined by the spin of the s-quark, which is also responsible for a large transverse momentum contribution. One of the earliest models trying to explain the transverse polarization with this assumption is the LUND model [25]. Here the s-quark of the Λ becomes polarized by compensation for the orbital momentum of the $s\bar{s}$ -pair created by the breaking of the string force field. This orbital momentum originates from the fact that the quark and anti-quark have to be produced a certain distance from each other due to energy and momentum conservation. The energy between them can be transformed in the transverse mass of the pair and it is assumed that if the string has no transverse degrees of freedom, the pair will obtain an orbital momentum perpendicular to the string. Although this model is qualitatively in agreement with the data, quantitatively the results are not correct. This is because it is assumed that there is no x_F -dependence of the transverse polarization, which is not the case. In the next sections three semi-classical models are given which give a reasonable description of the x_F -dependence of the transverse polarization. This makes it possible to compare the measurement presented in this thesis with the predictions of these models.

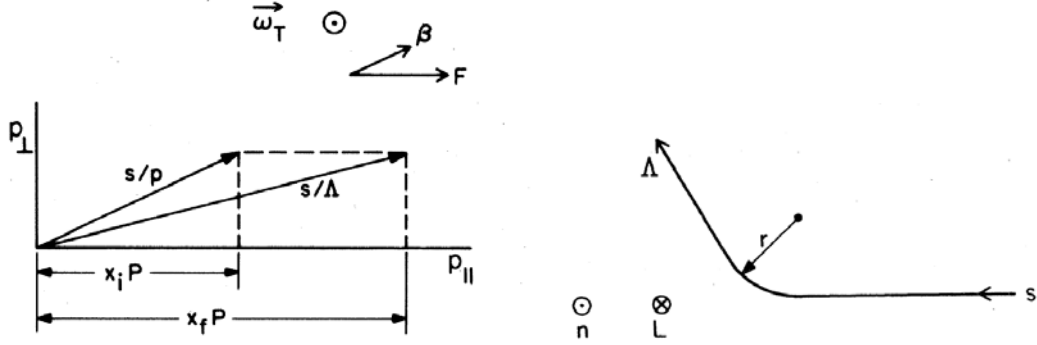


Figure 2.2: Left: Momentum vectors for the s quark in the scattering plane in the sea of the proton (s/p) and in the Λ (s/Λ). The recombination force is along the beam direction and the Thomas frequency $\vec{\omega}_T$ is out of the scattering plane. Right: the curved trajectory of the s -quark due to the recombination force and the corresponding orbital momentum vector \vec{L} . Also depicted is the normal of the production plane \vec{n} .

2.2.1 The Thomas Precession model

The model proposed by DeGrand and Miettinen [26], tries to explain the transverse Λ polarization using the following argument. A fast ud -diquark from the proton recombines with a slow s -quark from the sea, which consequently has to be accelerated in the longitudinal direction. At the same time the s -quark carries transverse momentum: on average, $p_T(s \text{ in proton}) \sim p_T(s \text{ in } \Lambda) \sim \frac{1}{2}p_T(\Lambda)$. So the velocity vector of the s -quark is not parallel to the change in momentum induced by recombination and the spin of the quark feels the effect of the Thomas precession given by [27]

$$\vec{\omega}_T = \frac{\gamma}{\gamma + 1} \frac{\vec{F}}{m_q} \times \vec{v}, \quad (2.5)$$

where $\vec{\omega}_T$ is the Thomas frequency, \vec{v} is the velocity of the s -quark and \vec{F} is the color force applied by the attraction of the di-quark. The concept is depicted in the left picture of figure 2.2. The Thomas frequency enters the effective Hamiltonian in combination with the spin of the s -quark \vec{S}

$$U = \vec{S} \cdot \vec{\omega}_T = -\frac{1}{r} \frac{\delta V}{\delta r} \vec{L} \cdot \vec{S}, \quad (2.6)$$

with \vec{L} the s -quark's orbital angular momentum in the potential $V(r)$. If this potential is attractive then $\vec{L} \cdot \vec{n} < 0$, where $\vec{n} = \vec{p}_{beam} \times \vec{p}_\Lambda$ is the normal to the production plane (see the right side of figure 2.2). In order to minimize the energy $\vec{S} \cdot \vec{\omega}_T$, the condition $\vec{L} \cdot \vec{n} < 0$ must apply, and consequently $\vec{n} \cdot \vec{S} < 0$. This explains the negative transverse polarization, observed in Λ polarization so far. The value of the polarization is derived to be [26]:

$$\mathcal{P}_\Lambda = \frac{3}{\Delta x_0} \frac{(1 - 3\xi)}{[(1 + 3\xi)/2]^2} \frac{1}{M^2} p_T, \quad (2.7)$$

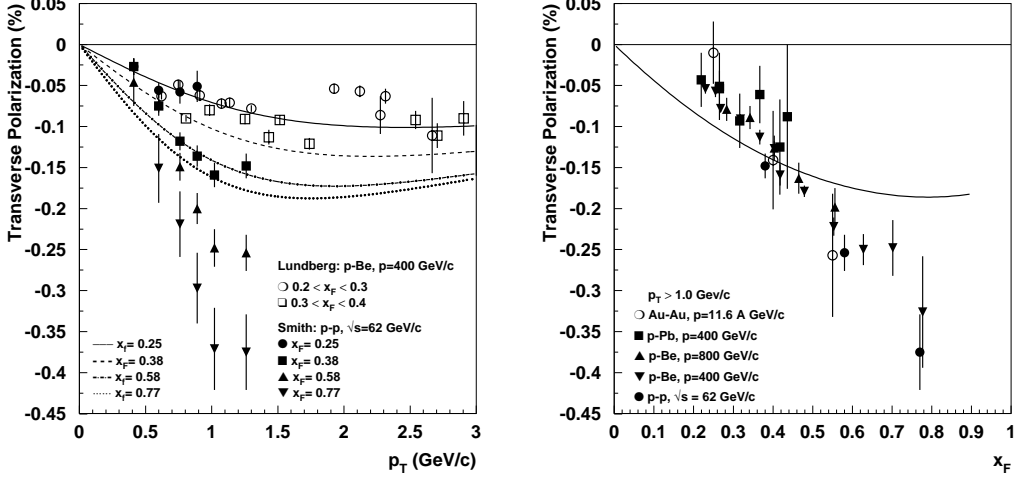


Figure 2.3: Dependence of the polarization on p_T (left) and x_F for $p_T > 1$ GeV/c (right). The predictions drawn are from the Thomas Precession model. With respect to the p_T -dependence the predictions are given for the four x_F values corresponding with the data. For the x_F -dependence the model is calculated at $p_T = 1$ GeV/c.

with $M^2 = \left[\frac{m_D^2 + p_{TD}^2}{1-\xi} + \frac{m_s^2 + p_{Ts}^2}{\xi} - m_\Lambda^2 - p_\Lambda^2 \right]$, where D denotes the ud-diquark.

In the simplest parameterization the x_F dependence can be characterized by $\xi = \frac{1}{3}(1 - x_F) + 0.1x_F$. Now the following values are set: $m_s = \frac{1}{2}$ GeV/c², $m_D = \frac{2}{3}$ GeV/c² and $\langle p_{TD}^2 \rangle = \frac{1}{4}p_{T\Lambda}^2 + \langle k_T^2 \rangle$, with $\langle k_T^2 \rangle = 0.25$ GeV²/c². With this parameterization a fit to the data can be made for the polarization versus p_T at fixed x_F (left plot of figure 2.3) and the x_F -dependence of the polarization for $p_T > 1$ GeV/c (right plot). This results in a normalization parameter given by $\Delta x_0 = 5$ GeV⁻¹, which is a typical recombination scale. The model manages to reproduce the shape of the p_T -dependence for the lower x_F region. For the high x_F region the model is inaccurate: the x_F -dependence shows a saturation of the polarization at high x_F which is not the case for the data.

Other parameterizations for $\xi(x_F)$ by recombination functions have been proposed and their x_F -dependence have been considered for the low p_T data (see figure 2.4) [29]. In this model, however, the saturation occurs even at lower values of x_F , which makes it more improbable.

Also the polarization of other hyperons and other types of collisions have been predicted [28]. The sign can be predicted in this model with the simple rule: slow partons preferentially recombine with their spins down in the scattering plane while fast partons recombine with their spins up (this is because now the parton is the attractive potential and hence the orbital momentum \vec{L} changes sign). The predicted sign is always correct, but unfortunately the magnitude cannot be predicted correctly. For example, the model predicts the same polarization for $p \rightarrow \Lambda$ as for $p \rightarrow \Xi^-$, but in real life the latter is two times smaller. Similarly, the $K^- p \rightarrow \Lambda$ has twice as large a polarization as the process $p \rightarrow \Lambda$, while the same magnitude is predicted. Furthermore in this approach

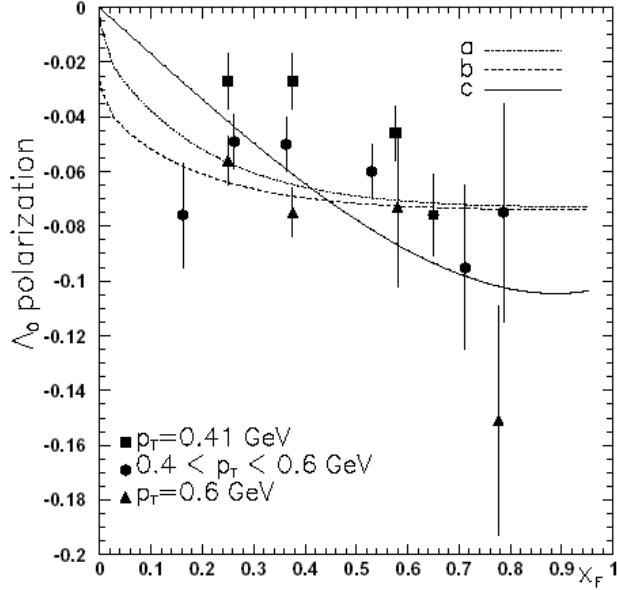


Figure 2.4: Polarization of Λ , P_Λ , as a function of x_F for three p_T intervals. Data are taken from [2,3,4], while the curves are from [29].

anti-hyperons should not be polarized in p-p collisions, because they are built up completely from sea-quarks (and no acceleration will take place), which is true for the $\bar{\Lambda}$, but not for the $\bar{\Xi}$.

In conclusion, the Thomas Precession model seems to be able to predict many features of hyperon polarizations and it manages to reproduce the data for lower x_F correctly. Since this is the region where our measurements are performed this model is an important reference.

2.2.2 The Berlin model

This model [30] states that a hadron is polarized *if and only if* its valence quarks are polarized, and due to a significant surface effect only valence quarks retain information about the polarization. In order to explain the Λ polarization the existence of a large A_N was assumed, where the analyzing power A_N is defined as:

$$A_N = \frac{d\sigma_{A^\dagger+B \rightarrow C^\dagger} - d\sigma_{A^\dagger+B \rightarrow C^\downarrow}}{d\sigma_{A^\dagger+B \rightarrow C^\dagger} + d\sigma_{A^\dagger+B \rightarrow C^\downarrow}} \quad (2.8)$$

It is shown that this large value of A_N is due to the orbital motion of valence quarks in the original projectile and it can be described by the following points, where the subscripts v and s denote a valence or a sea quark. Superscripts P and T refer to a quark from the projectile or the target:

- (I) Mesons (M) and baryons (B) produced through $q_v^P + \bar{q}_s^T \rightarrow M$ and $q_v^P + (q_s q_s)^T \rightarrow B$ have a large probability to go left (w.r.t. the collision axis looking downstream) if q_v^P is upwards

polarized (w.r.t. the production plane).

- (II) Baryons produced through $(q_v q_v)^P + q_s^T \rightarrow B$ are associated with $(q_v^a)^P + \bar{q}_s^T \rightarrow M$ and have a large probability to move in the opposite transverse direction w.r.t. the collision axis as M does. Here $(q_v^a)^P$ is the remaining quark from the projectile not used in the baryon production.

Accordingly the Λ can be produced in direct fusion by means of 3 processes:

- An $(u_v d_v)$ diquark from the projectile P picks up a s_s quark associated with the target T and forms a Λ : $(u_v d_v)^P + s_s^T \rightarrow \Lambda$.
- An u_v valence quark from the projectile picks up a $(d_s s_s)$ diquark from the target: $u_v^P + (d_s s_s)^T \rightarrow \Lambda$.
- The same as process b but now a valence quark d_v from the projectile is taken: $d_v^P + (u_s s_s)^T \rightarrow \Lambda$.

These processes have different x_F regions where they dominate. In the lowest x_F region ($x_F < 0.3$) the largest contribution to the cross-section is from non-direct formation, which comes from the interactions of the seas of the colliding hadrons. In the largest region ($x_F > 0.6$) process

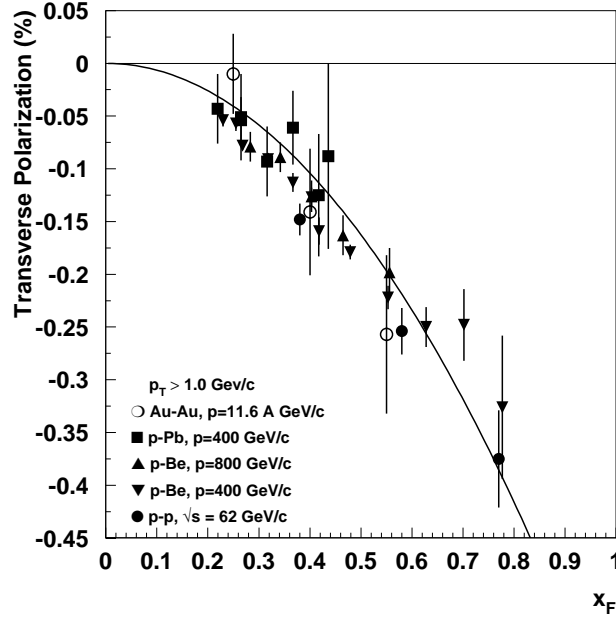


Figure 2.5: The Berlin model prediction for the transverse Λ polarization as a function of x_F for $p_T > 1$ GeV/c.

(a) dominates and in the intermediate region the direct formation processes (b) and (c) are the most important. So, for example, to explain the large left-right asymmetry A_N found in polarized proton beam experiments at large x_F process (a) has to be looked at. If we now take the diquark $(u_v d_v)$ to have spin zero, the polarization of the proton has to be carried by the remaining valence quark u_v^a . When this fuses with a suitable anti-sea-quark of the target to form an associated meson (II), according to (I) it has a large probability to obtain an extra transverse momentum to the left. Momentum conservation causes the Λ to have a large probability to be produced to the right, contributing negatively to A_N .

The explanation for the transverse Λ polarization is similar. In this case the polarization of the Λ is provided by the s-quark which obtains a negative polarization through the following mechanism: according to (II) an associated K^+ is produced by $(u_v^a)^P + \bar{s}_s^T \rightarrow K^+$. Now if the Λ going to the left is considered, the associatively produced K^+ has a large probability to go right, which implies from (I), that it is most likely to be downward polarized. Since the K^+ is a pseudo-scalar its spin should be zero, which demands that the \bar{s}_s^T is upward polarized. By assuming that the sea $s\bar{s}$ pair is not transversely polarized the corresponding s_s^T should be downward polarized which finally yields a negatively polarized Λ . Note that if the left going Λ is produced by process (b) or (c), the valence quark used should have a large probability to be upwards polarized. This however says nothing about the polarization of the Λ , which is completely defined by process (a). Therefore, also in this case the largest polarization is at the large x_F region where this process dominates.

By making use of number density functions, which were shown to give a good description of the cross-section [31], a quantitative estimation has been made. This can be seen in figure 2.5 where the dependence of the transverse Λ polarization on x_F is depicted. As explained above, in this model only at large x_F the polarization is significant. Although the fit looks quite reasonable, there are many properties of this model which are not attractive: there are many assumptions (like associative production and transversely unpolarized $s\bar{s}$ -pair). Moreover it provides no prediction for a p_T dependence and there are no predictions for anti-hyperons.

2.2.3 The Troshin-Tyurin model

In this approach the transverse momentum of the Λ is introduced by the orbital momentum of quark-antiquark pairs inside the hadron [32]. Here the picture of hadrons consisting of constituent quarks embedded in a cloud of sea-quarks is used. In a hadron-hadron collision overlapping between peripheral clouds occurs at the first stage of the collision. Under these conditions the cloud is excited and as a result quasi-particles (massive quarks) appear in the overlapping region. Furthermore the constituent quarks located in the central part of the hadron are supposed to scatter quasi-independent by the mean field generated by the appearance of the massive quarks. The inclusive production of Λ hyperons then results from two mechanisms:

- (a) Recombination of constituent quarks with virtual massive strange quarks. These are soft interactions which occur at low p_T (say $p_T < 1.0 \text{ GeV}/c$).
- (b) Single or multiple scattering of the constituent quark in the generated mean field, excitation of this constituent quark, the appearance of a strange quark as a result of the decay of the constituent quark, and subsequent fragmentation of strange quarks into the Λ . This mechanism is determined by the interactions at distances smaller than the constituent quark radius, and is therefore associated with hard interactions ($p_T > 1.0 \text{ GeV}/c$).

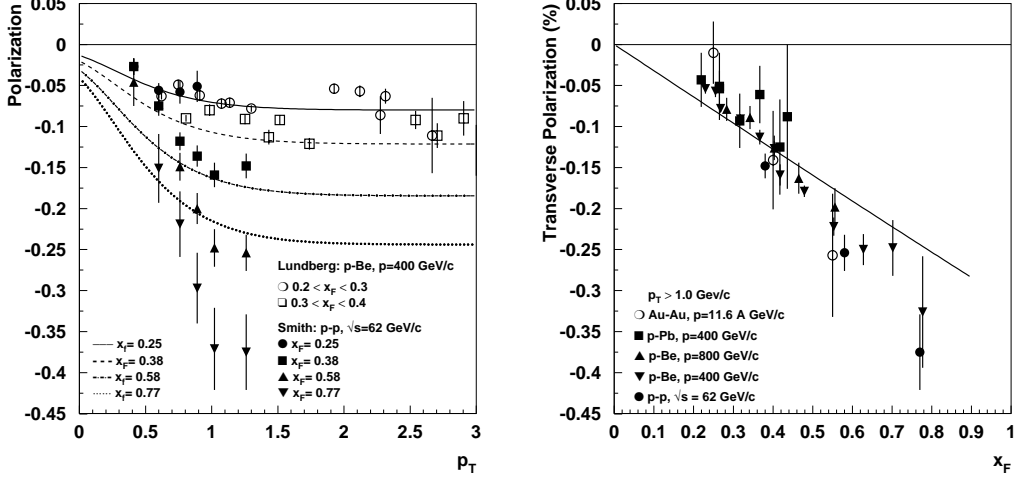


Figure 2.6: The prediction of the Troshin-Tyurin model for the polarization as function of p_T (left) and x_F (right). The p_T dependence is given for the four x_F values of the data.

The polarization now originates from the multiple scattering by the mean field of the parent constituent quark. Since it has non-zero mass it becomes negatively polarized [33] and this polarization results in a polarization of produced strange quarks and the occurrence of the corresponding angular momentum. An analytic expression for the Λ polarization is derived:

$$P(x_F, p_T) = \sin(P_q(x_F)\alpha\langle L_{q\bar{q}}\rangle) \frac{C(x_F) \exp(p_T/m_s)}{(p_T^2 + \Lambda_\chi^2)^2 + C(x_F) \exp(p_T/m_s)}. \quad (2.9)$$

In this derivation the average orbital momentum $\langle L_{q\bar{q}}\rangle$ is the contribution of the quark-anti-quark pairs to the spin of the proton. This is estimated to be 0.4 from DIS data [34,35]. The parameter α is the fraction of the orbital momentum due to the strange quarks. Finally $P_q(x_F)$ is the polarization obtained by the constituent quark by the multiple scattering. In the simplest possible parameterization the dependence of the polarization on x_F is taken to be linear:

$$P_q(x_F) = P_q^{max} x_F, \quad (2.10)$$

where $P_q^{max} = -1$. In the p_T -dependence term the constant $\Lambda_\chi \sim 1$ GeV/c is the scale of spontaneous breaking of chiral symmetry [19]. Since the size of the constituent quark is determined by this scale ($R_Q \simeq \frac{1}{\Lambda_\chi}$), it defines the region where the (hard) interactions feel the presence of internal momenta in the constituent quark and hence where the polarization is expected to be significant. So at $p_T > \Lambda_\chi$ the polarization is independent of p_T and only the x_F dependent term of expression 2.9 has to be applied. The fit of this part to the data (which can be seen in the right plot of figure 2.6) gives $\alpha = 0.8$ and shows that the x_F dependence can be reproduced well. Now, if $p_T < \Lambda_\chi$, mechanism (a) mentioned above starts to dominate, and since this yields unpolarized Λ s

the polarization goes to zero for $p_T \rightarrow 0$. This can be seen in the fit on the left side of figure 2.6, where the shape of the p_T -dependence is more or less reproduced. The prediction of the model for various x_F values has been plotted with $m_s = 0.2 \text{ GeV}/c^2$ and $C(x_F) = 0.2$, where the last parameter was determined from a fit to p-p data at $x_F = 0.44$. For the lower two x_F values the calculation seems to be good, but for higher x_F values the model underestimates the data. Also this model relies heavily on many assumptions like the linear dependence on x_F and the occurrence of polarization due to multiple scattering. Finally the model gives no predictions for other hyperons.

2.3 Polarization in Heavy Ion collisions

If a QGP has been created, zero polarization is expected for Λ s originating from this region. In the Troshin-Tyurin model this can occur by assuming that in a QGP chiral symmetry is restored, while in the models exploiting confinement, like the LUND and Thomas Precession model the reference production plane disappears. In a QGP the information on the direction of the incoming projectile (and consequently the ud-diquark) is lost. The production of a particle is then similarly to the production out of sea-quarks in p-p collisions. Hence the Λ production will be similar to $\bar{\Lambda}$ production in hadron-hadron collisions, which are not polarized. Following this argument several authors have proposed to use the vanishing of transverse Λ polarization in heavy-ion collisions as a signature of the creation of a QGP [13,36,19]. However, this does not always imply that in experiments no polarization at all should be seen. This will be shown for the transverse polarization, as well as for the longitudinal polarization in the next two subsections.

2.3.1 Transverse polarization

In nucleon-nucleon collisions there are three effects which can possibly introduce a diminishing of the Λ polarization [13]:

- (1) Secondary Λ production by pion-nucleon scattering.
- (2) Λ production from a QGP
- (3) Secondary scattering of leading Λ hyperons with nucleons within the interaction zone.

The first effect should become important in collisions of large nuclei at high energy, because of the increase of the pion production cross section under these conditions. However the Λ s produced in this process are usually confined within the non-free nucleon-nucleon phase space kinematical limit and at low laboratory momenta. Therefore they can be excluded from the polarization analysis by applying kinematical cuts. The second effect should yield zero polarization as mentioned before, while the third effect is estimated to be a small effect by Panagiotou [13]. Recently, however, a new model has been proposed in which it is stated that secondary scattering (on the contrary) even can enhance the polarization [36]. They argued that secondary elastic scattering of Λ 's with nucleons can influence the final polarization measurements by producing

- (a) a shift in the longitudinal Λ momentum
- (b) a shift in the transverse Λ momentum

(c) a flip in the original Λ spin direction.

For the first two effects they make a quantitative estimation, while they omit effect (c), because no good estimate is possible for this effect due to lack of experimental data. The production of Λ hyperons in Pb-Pb collisions is described, which is assumed to be driven by two contributions. The first contribution is from Λ s produced in the interaction region where the density is not high enough to deconfine quarks and gluons. This should occur in peripheral collisions (with high impact parameter b). They use the recombination model of section 2.2.1 to account for the production of Λ s in this domain. The second contribution is from the region where a QGP is created (supposedly at small b), where coalescence of independent slow quarks takes place. These two contributions thus depend on the type of collisions. This can be shown in an estimate of the dependence of the cross section on the impact parameter b (figure 2.7).

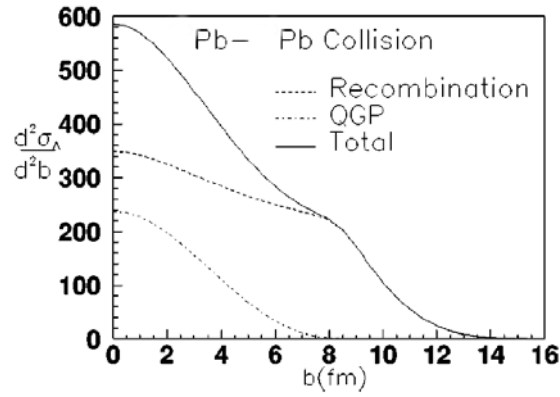


Figure 2.7: Λ production as a function of the impact parameter in a QGP (dash-dotted line) and in the periphery (dashed line). The solid line represents the total Λ production cross section.

With both contributions taken into account, the Λ polarization is calculated using the b -dependent differential cross sections. The result of this can be seen in figure 2.8. Here the clear Thomas Precession-like p_T dependence of the polarization can be seen. In this case however, it is shown for different impact parameters, where the magnitude of the Λ polarization for the most central collisions ($b = 0$ fm) and the most peripheral ($b > 9$ fm) differ by a factor of 2.

In addition to this, also the effect on the polarization of secondary scattering of the Λ in the nuclear medium is determined (figure 2.9). For the low p_T region there is a significant increase of the polarization, the largest a factor 5 for the case $b = 0$ fm. Furthermore the most centrally produced Λ s show a larger increase of the polarization than the more peripheral ones. Unfortunately only the lower p_T region is shown in this figure taken from [36], so it is not clear whether at high p_T the values of the polarization with and without in-medium effects converge. It is interesting to see the maximum value of the polarization caused by these effects.

A disadvantage of this model is, that the cross sections are only taken to be dependent on impact parameter b and not on x_F . In this way it is not clear what the polarization effects are at mid-rapidity as opposed to the fragmentation region.

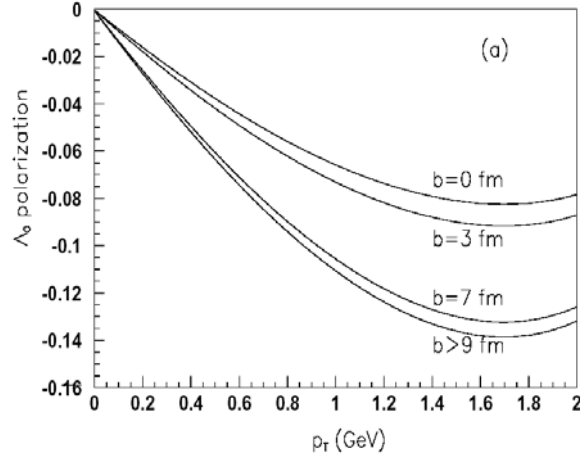


Figure 2.8: Transverse Λ polarization as function of p_T for different impact parameters of the collision.

2.3.2 Longitudinal polarization

The presence of longitudinal polarization in a sample of Λ hyperons could be due to the Λ s that are decay products of the Ξ . If the Ξ is unpolarized, the parity violation in the Ξ decay will induce a non-vanishing longitudinal polarization in the Λ . For the Λ s which are longitudinally polarized the asymmetry found in the internal decay θ angle of the proton in the longitudinal direction amounts to:

$$\frac{dN}{d\cos\theta} = \frac{1}{4\pi} [1 + \alpha_\Lambda \alpha_\Xi \cos\theta] \quad (2.11)$$

where $\alpha_\Lambda = -0.642$ and $\alpha_\Xi = -0.456$ are the Λ and Ξ decay parameters. The same relation is valid for the anti-particles and because of the abundance of multi-strange anti-baryons in a QGP, the longitudinal polarization of the $\bar{\Lambda}$ has been proposed as a probe for the creation of a QGP. The longitudinal asymmetry is estimated to be of the order [37]:

$$\frac{N_\uparrow - N_\downarrow}{N_\uparrow + N_\downarrow} = \frac{1}{2} \left[\frac{N_{\Xi}}{N_{\bar{\Lambda}}} \right] \alpha_\Lambda \alpha_\Xi \quad (2.12)$$

where N_\uparrow and N_\downarrow are the particles produced 'above' and 'below', with respect to the plane normal to the Λ momentum. The term in the square brackets is the relative abundance of all polarized $\bar{\Lambda}$ hyperons to the total number measured $\bar{\Lambda}$ particles. This value is predicted to have a value to be approximately $\frac{1}{2}$, which implies a longitudinal polarization of 7%. This is 5 times more than is seen in pp interactions [38].

2.4 Summary

The transverse polarization determined from straightforward pQCD calculations shows that at high p_T it vanishes. This is in disagreement with the data. Because the polarization effect seems to arise

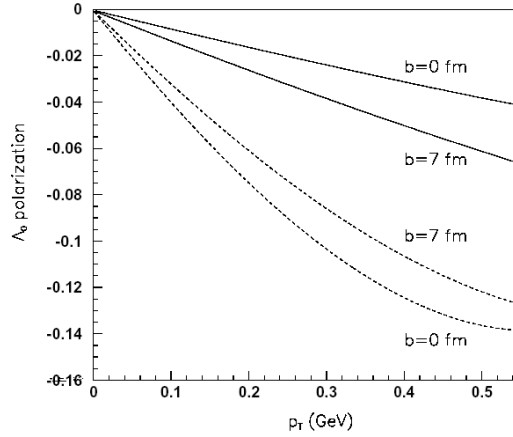


Figure 2.9: *The influence of secondary scattering in the nuclear medium on the transverse Λ polarization for two different values of the impact parameter. The straight line gives the result without secondary scattering and the dashed lines give results, affected by the secondary scattering of the Λ in the medium.*

from the non-perturbative region, modifications to the pQCD based models have been proposed. Although these modifications manage to introduce polarization effects, there are some large disadvantages: for the higher twist effects the quantitative description is not yet accurate enough and for the polarized fragmentation functions the contribution from the hadron fragmentation to the polarization seems to be overestimated. Furthermore, both the modifications are put in by hand and hence they lack physical rigour.

Alternatively semi-classical models are used, which all have some predictive power. In these models the p_T dependence of the polarization is explained by assuming that the polarization of the Λ arises from the spin of the s-quark (in a SU(6) picture). This s-quark obtains transverse momentum when it is created by breaking a color string, which results in a rotating $s\bar{s}$ -pair (Lund model); it obtains transverse momentum by the orbital motion of valence quarks in the projectile (Berlin model) or the orbital motion of quark-antiquark pairs in the hadron (Troshin-Tyurin model). The x_F dependence is provided by the ud-diquark which creates the color string with the target (LUND model), the di-quark that attracts the sea-quark, whose spin feels the influence of the Thomas Precession (Thomas Precession model) and for the Berlin model the polarization process dominates at large x_F with respect to the non-polarizing creation processes of the Λ . In the Troshin-Tyurin model the polarization is introduced by multiple scattering which will be larger at high x_F .

The LUND model does not predict a dependence on x_F and therefore is not considered here. The Thomas Precession model and the Troshin-Tyurin model manage to give a good description of the p_T -dependence for the x_F -region up to 0.5 and hence serve as a good reference for the data investigated in this thesis, which are taken at this region. The Berlin model gives no quantitative prediction for the p_T dependence, but its x_F dependence is accurate and can also be used here.

Finally the transverse polarization in heavy ion collisions is predicted to be suppressed for

central collisions (Ayala et al.) or even to vanish (Panagiotou). Since the NA57 experiment is able to determine the centrality of the collision this dependence can be investigated. The longitudinal Λ polarization can give information on the Ξ production and hence can give additional information on strangeness production in heavy ion collisions.

3

Experimental Setup

The data analyzed in this thesis were collected at CERN (Centre Europeenne de Recherche Nucleaire) laboratory in Geneva. In the SPS (Super Proton Synchrotron) accelerator protons and lead ions were accelerated and collided on a fixed target. The particles coming out of the collision were detected in the NA57 detector. In this chapter the SPS accelerator is described briefly, after which the NA57 detector setup is described.

3.1 The SPS accelerator

In figure 3.1 a view of the CERN accelerator complex is given. The largest component is the former LEP (Large Electron Positron collider) ring, currently being transformed to house the LHC (Large Hadron Collider). The particles used in the LEP ring were injected by the SPS accelerator. At the same time this accelerator was able to produce independent beams of protons and heavy ions, which continued after the shutdown of LEP. The proton beam can have an energy of up to $450 \text{ GeV}/c$, while the heavy ions can have an energy between 100 and $400 \text{ GeV}/c$ per accelerated proton.

The heavy ions used for the collisions are first ionized in the Electron Cyclotron Resonance (ECR) source and then selected in Pb^{27+} charge state only. These ions are then further stripped by Strippers to the final Pb^{82+} state and in between accelerated in the LINAC (Linear Collider), the Proton Synchrotron Booster (PSB) and the Proton Synchrotron (PS). The heavy ions provided by the PS are delivered in four ion cycles of 1.2 s each within a supercycle of 19.2 s. They have an energy of $4.25 \text{ AGeV}/c$ and then are accelerated in the SPS to a maximum energy of $400 \times 82/208 = 158 \text{ AGeV}/c$. After the SPS has increased the beam energy to the required value, the beam is delivered to the North Area target hall, where a splitter fills 6 beam-lines simultaneously. Of these the H4 beam line is used by the NA57 experiment. The typical ion flux on the target is of the order of 1×10^6 ions per spill. A description of the NA57 experimental setup is given in the next section.

3.2 The NA57 Experiment

The NA57 experiment has been designed to measure (multi)strange hadrons (Λ , Ξ^- and Ω^- hyperons and their anti-particles) for different collision systems at different beam energies. These hadrons can be identified by recording the tracks of their (charged) decay particles. The reconstruction of the decay particles is troubled by the low production probabilities of the strange hadrons, which asks for a high event rate. This can be obtained by a large acceptance and therefore detectors have to be placed close to the target. This introduces a large number of background particles and in order to be able to still reconstruct the decay particles of the original hadrons the two-track resolution of the detectors has to be very good. The requirement of a good resolution (of the order of tens of microns) and use at high event rate can be met by silicon pixel detectors.

In figure 3.2 an overview of the apparatus is shown. In the NA57 definition, the beam direction is taken as the X-axis, while the Z-direction is taken in the direction of the magnetic field. The Y-axis is then chosen to give an right-handed coordinate system. The whole setup is positioned in the Goliath Magnet, which has a maximum magnetic field of 1.4 T along the vertical direction. In this way the momentum of the particles produced in the reaction can be determined. In addition to the tracking device, comprising of the silicon pixel detectors, also other elements are included. The

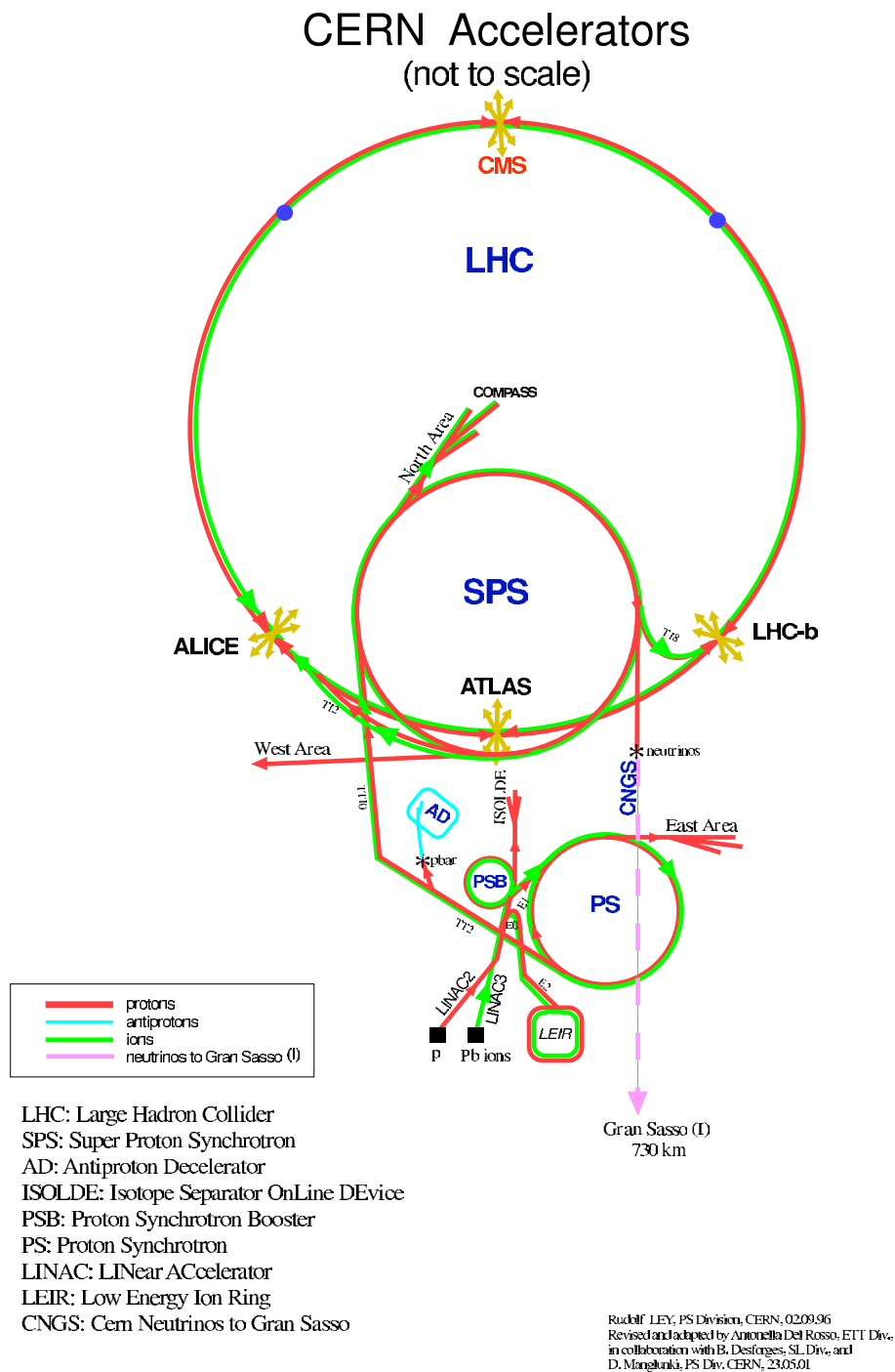


Figure 3.1: The SPS accelerator complex at CERN.

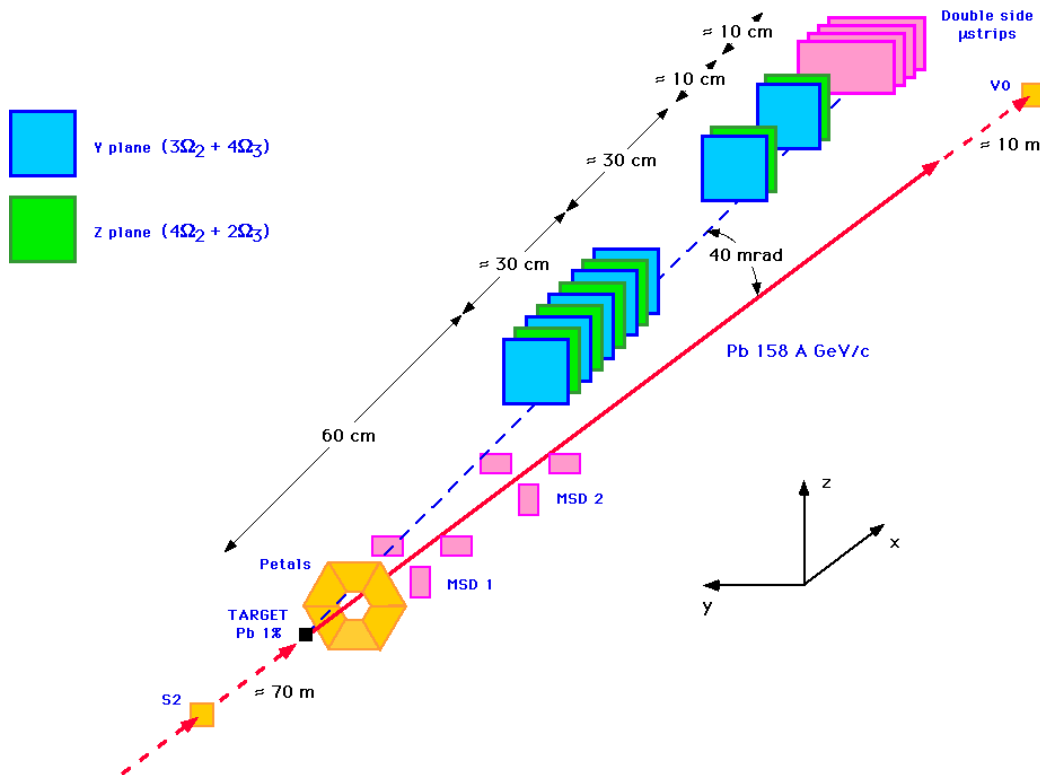


Figure 3.2: Schematical view of the NA57 experiment setup (not drawn to scale) for the 158 A GeV/c data-taking period of 1998. The beam particles are coming from the left. The Silicon Compact Telescope consists of Y and Z pixel planes alternately (see the end of subsection 3.2.4).

target region can consist of different targets. These are discussed in subsection 3.2.1 together with the possible beams. A sample of scintillator detectors are placed in the beam line and positioned behind the target for the trigger purposes. This is explained in subsection 3.2.2. Multiplicity Strip Detectors (MSD) are placed behind the target to measure the number of particles produced in the collision, which can be taken as a measurement of the centrality of the collision (section 3.2.3). The silicon pixel detectors are grouped together in a central tracking device: the *Silicon Telescope* (section 3.2.4). The silicon telescope is suspended from the so called *Optical bench*, from which also the *Lever Arm* is suspended. This lever arm can consist both of silicon pixel detectors and silicon double-sided micro-strip detectors. This last type of detector was developed and maintained by the University of Utrecht. Therefore more attention is paid to the description of this part of the setup (section 3.2.4), especially as in the next chapter the performance of the lever arm with these detectors included will be discussed.

3.2.1 Collision systems

Table 3.1: Overview of the data runs taken by the NA57 experiment.

Data taking	System	Beam momentum	\sqrt{s} (AGeV/c)	Sample size (events)
1998	Pb-Pb	158 AGeV/c	17.3	230 M
1999	p-Be	40 GeV/c	8.8	60 M
1999	Pb-Pb	40 AGeV/c	8.8	260M
2000	Pb-Pb	158 AGeV/c	17.3	230 M
2001	p-Be	40 GeV/c	8.8	100M

The physics goal of NA57 is to extend the scope of the WA97 experiment. This made the first collision system studied at NA57 a 158 AGeV/c Pb beam on a Pb-target. In this way a cross check of the results of WA97 could be obtained and an extra multiplicity bin could be added. This measurement was repeated in 2000 in order to increase the statistics for Ω^- and Ξ^- hyperons in the lowest multiplicity bin. Between these periods, in 1999, also measurements were done with a beam energy of 40 AGeV/c, both for a p-Be and a Pb-Pb system. At this energy the center of mass energy for the Pb-Pb collision is $\sqrt{s} = 8.8$ AGeV/c which is approximately half the center of mass value of the system at 158 AGeV/c ($\sqrt{s} = 17.3$ AGeV/c). Considering the fact that the value achieved at the Alternating Gradient Synchrotron (AGS) at BNL is 4.7 AGeV/c, with the 40 AGeV/c runs it is possible to measure in a new range and the dependence of the strangeness production of the energy of the collision system can be investigated. The p-Be run at 40 GeV/c is necessary to give reference data for a smaller collision system. Since the cross sections for the Ω^- and Ξ^- are very low for this collision system, in 2001 the experiment for the p-Be system at 40 GeV/c was repeated to increase statistics. In table 3.1 an overview is given of the collision systems together with the number of events collected. In order to enable different collision types the target could be removed and changed. For the lead induced collisions a target with a thickness of 0.4 mm was installed, which is 1% of the interaction length for Pb-Pb interactions. The number of particles in the beam provided by the SPS amounts to 1×10^6 ions/burst, giving around 1×10^4 interactions every 19.2 seconds. For the proton beam data a Beryllium target with an interaction length of 8% has been used. Furthermore during all periods runs were taken with the target removed to determine the empty-target contamination. In the following the data samples will be indicated by their year and their system: e.g the lead run in 1998 will be indicated by Pb1998, while the proton run in 2001 is denoted as p2001.

In the chapters on the track recognition and the particle selection the data from the Pb1999 and Pb2000 runs will be used. In the analysis of the yields and the polarization only the Pb1998 data is considered in this thesis. Therefore in the next sections only the setup for the lead runs will be discussed.

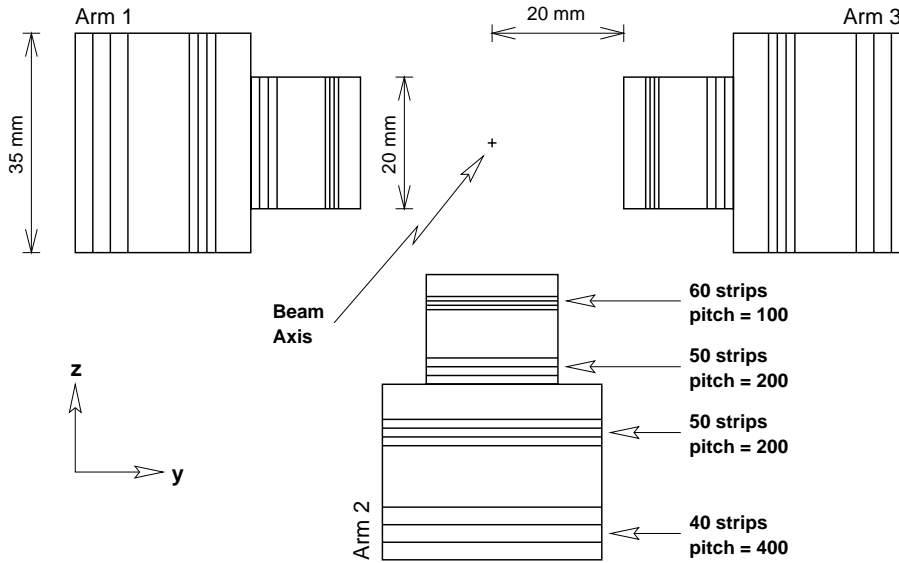


Figure 3.3: Front view of a Multiplicity Strip Detector (MSD) station. The pitch of the strips is given in μm .

3.2.2 Trigger

The NA57 experiment has two kind of collision systems: the proton and the lead induced reactions. This will give rise to two different multiplicities of particles which asks for a different trigger logic. In the following only the setup used for the lead interactions is considered. The basic part of the trigger is to check whether an interaction has taken place in the target. In order to determine whether an interaction has occurred, beam counters have been placed in the beam line, as can be seen in figure 3.2. Counter S2 is placed around 70 m upstream of the center of the magnet, which is 60 cm from the target. This counter measures the passage of a beam particle. At 9 m behind the target the V0 counter is placed. This counter is used as a so called 'veto counter'. This means that in case of an interaction in the target, it is assumed that no beam particle can be measured by V0.

$$\text{BEAM} = \text{S2} \cdot \overline{\text{V0}}.$$

The S2 and V0 counters consist of quartz Čerenkov detectors. In case the counter is passed by two ions at the same time, the signal will be higher and because of this the trigger logic also produces a second output for the S2 counter: S2D. The trigger should reject these events and therefore a veto is demanded. The lead trigger should select the 50 to 60% most central nucleus-nucleus collisions and therefore a large number of particles will come out of the interaction region. The petals, scintillators which are arranged around the beam line (at 2.4 cm) like their flower-counterparts around the bud, provide a fast measure of the centrality of the collision. The Petals

cover the pseudo-rapidity in the region $1 < \eta < 2$, where the pseudo-rapidity is defined as:

$$\eta = -\ln \tan \frac{\theta}{2}, \quad (3.1)$$

in which θ is the angle between the momentum of the particle and the beam axis. The resultant trigger can be defined to select on the most central events:

$$\text{INT} = \text{BEAM} \cdot \overline{\text{S2D}} \cdot \text{PT}(5/5).$$

where it is demanded that in addition to a BEAM event, also all (5 out of 5) petals have fired. There are only 5 petals included because one petal scintillator detector was not functioning during the Pb1998 period. Even when during the 1999 and 2000 data-taking this petal was repaired, the requirement for 5 hits was kept for compatibility. When all the requirements are met, the trigger signals for the detectors to be read out. During the readout a dead time signal is generated which acts as a veto for following events. The length of the dead time signal is determined by the slowest component in the readout, which was either the pixel or double-sided micro-strip detectors. This dead time had a value of around 1 ms. For a more detailed description of the trigger logic see [45,46].

3.2.3 Multiplicity Strip Detector

The Petals give a rough estimation of the event centrality and are ideal for trigger purposes because of their fast response. In order to have a precise measurement for off-line analysis the Multiplicity Strip Detector (MSD) is added. This MSD consists of two identical stations which are positioned at 20 and 55 cm from the target. The front view of a station can be seen in figure 3.3. The station consists of three independent arms which are positioned below and at both sides of the beam line at a distance of 2 cm. Each arm is built of four parts, which are silicon micro-strip detectors with different pitches for the strips. The first station measures the multiplicity of charged particles in the pseudo-rapidity region $1.88 < \eta < 2.99$, while the second measures in the range $2.87 < \eta < 4.00$. This amounts to a total azimuthal coverage of 34%. Note that the MSD is only installed during the lead data-taking.

3.2.4 Silicon Telescope

The tracking device of the setup consists of a spectrometer, the *Silicon Telescope*, which is an array of silicon detectors suspended from an optical bench. This bench points back at the target and is placed completely inside the magnet. It can be inclined in order to measure hyperons around mid-rapidity and at medium transverse momentum. The inclination angle of the bench and the distance from the first detector to the target depend on the beam energy. For the case of a lead beam at an energy of 158 AGeV/c the inclination angle is 41 mrad and the distance is 60 cm. For the 40 AGeV/c setup the angle and the distance amount to 72 mrad and 40 cm.

The detectors are suspended from the bench in such a way that their lower edge is on a straight line pointing to the target and that they are placed symmetrically with respect to the beam. This gives the same geometric acceptance for particles and anti-particles.

The silicon telescope can be divided in two parts: the *Compact Telescope* and the *Lever Arm* (see figure 3.2). These are described in the following sections. A schematic overview of the precise configuration of the telescope for each run period is given in appendix A.

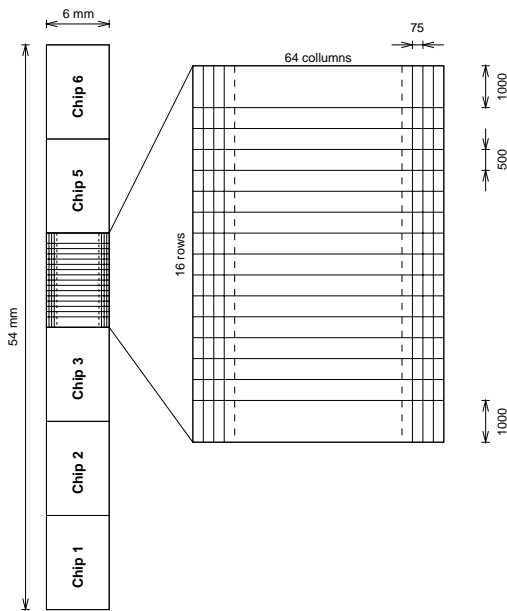


Figure 3.4: Top view of a silicon detector ladder from the Omega2 detectors. A part of the ladder is magnified. The pixel sizes are given in μm .

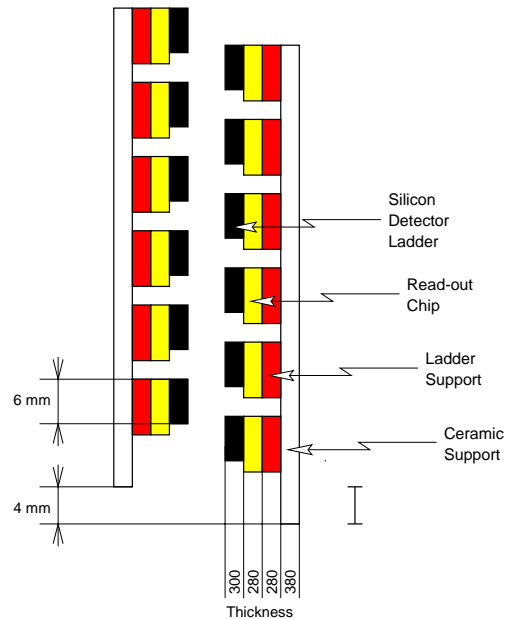


Figure 3.5: Schematic side view of the two arrays composing a logical plane of a pixel detector. The thicknesses are given in μm .

Compact Telescope

The compact part of the telescope is used for the track reconstruction and can be considered as a vertex detector. Therefore it is placed close to the target. In order to make precise measurements of the particle trajectories this part only consists of silicon pixel detectors, which have a high granularity. The number of pixel detectors used during the data-taking periods has ranged from 9 to 11. The detectors are placed 2 cm from each other giving a total length of around 30 cm for the whole compact part. In the following the silicon pixel detectors will be described in detail.

Silicon Pixel Detectors

The silicon pixel detectors have been developed by WA97 in collaboration with the CERN RD19 group. The NA57 experiment makes use of two different types of pixel planes: one based on the Omega2 front-end chip [40,41,42] and one on the newer Omega3 chip [43]. The difference between these types lies in the granularity, while their cross section is the same: they both have a sensitive area of $53 \times 55 \text{ mm}^2$. The thickness of the planes is kept small to make the detector transparent. This results in a layer of $300 \mu\text{m}$ thickness.

The Omega2 based planes are comprised of ladders, which are silicon wafers with an area of $54 \times 6 \text{ mm}^2$. Each ladder is built of 96 columns and 64 rows of rectangular diodes (pixels) which

have a size of $500 \times 75 \mu\text{m}^2$. Figure 3.4 gives an overview of a ladder. The pixels are read out digitally by chips, each containing 16 times 64 read out cells, yielding 6 chips per ladder. Six ladders are glued side by side on a ceramic support with an inter-spacing of a couple of mm's to create an array. The array consequently does not cover the $5 \times 5 \text{ cm}^2$ surface with sensitive material and therefore an identical array is mounted behind it, but shifted by 4 mm (fig. 3.5). In this way the whole area is completely covered and ladders even overlap, which is useful for alignment purposes. The two planes together are considered to be one pixel detector and the total number of pixels amounts to: $96 \times 64 \times 12 = 73728$.

The Omega3 detectors have the same structure but instead of the pixels of size $500 \times 75 \mu\text{m}^2$, the new chips employ pixels of size $500 \times 50 \mu\text{m}^2$. Furthermore the chips contain 16 columns by 127 rows, giving the equivalent of 4 ladders in one array. This improvement has the result that the same sensitive area is now covered by 98 thousand pixels. Because of the fact that the pixels are rectangular, they will give greater resolution along one direction than the other. In order to have good resolution in both directions planes are rotated with respect to each other. The set of detectors can be split up in Y- and Z-planes, with the better resolution in the corresponding direction. In figure 3.2 the different detectors are denoted by different shades of grey. As can be seen they alternate in the setup.

Lever Arm

The lever arm is installed to improve the momentum resolution of the high momentum charged particles in the bending plane. Therefore the detectors used need to have a high resolution in the Y-direction of the experiment. This requirement can be met by silicon micro-strip detectors. These have been included in the lever arm in addition to pixel detectors for the Pb1998 run and from 1999 on were the only detectors in the lever arm. The lever arm was positioned around 30 cm from the last pixel detector for all experiments.

Silicon Micro-strip Detectors

The silicon micro-strip detectors were developed and built at the institute of Sub Atomic Physics at Utrecht University/NIKHEF, and they are prototypes for the detectors which will be used in the ALICE experiment. In the period from 1998 to 2001 two different kinds of micro-strip detectors have been employed: double- and single-sided detectors. Because the single sided detectors are similar to the double sided detectors, but just have a more simple structure only a description of the double sided detectors is given.

The micro-strip detectors are placed further away from the target than the compact tracker. Due to the magnetic field particles have moved away from the beam line axis in the bending plane. In order to have a reasonable acceptance for charged particles the micro-strip detectors are wider than the pixel planes: the planes measure $75 \times 42 \text{ mm}^2$, with an active area of $73 \times 40 \text{ mm}^2$.

The double sided micro strip detectors have a bulk of N-type Si with a thickness of $300 \pm 15 \mu\text{m}$ in which strips, which are $0.5 \mu\text{m}$ thin, are implanted on both sides. The strips have a pitch of $95 \mu\text{m}$. In figure 3.6 the cross section of a double sided detector is shown. The strips implanted on the junction side are made of P+ doped silicon and therefore this side will be referred to as the P-side. These strips are covered by a SiO_2 dielectric with a thickness of $0.3 \mu\text{m}$, which is spread over the whole active surface. On this layer, which acts as a insulator, $1 \mu\text{m}$ thick aluminum strips are placed above the implanted strips. In this way for each strip a capacitor is formed, which

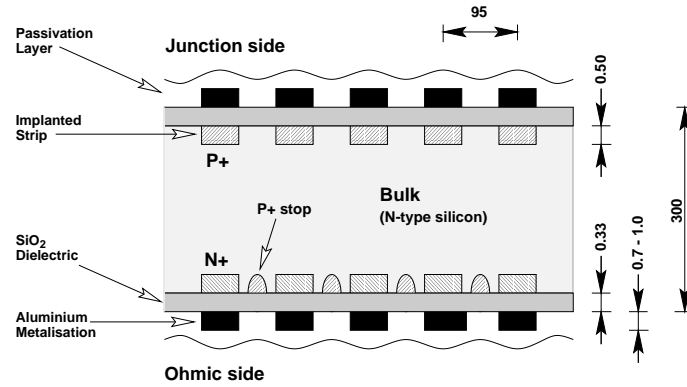


Figure 3.6: Cross section along the long side of a double-sided strip detector (not drawn to scale). The dimensions are given in μm .

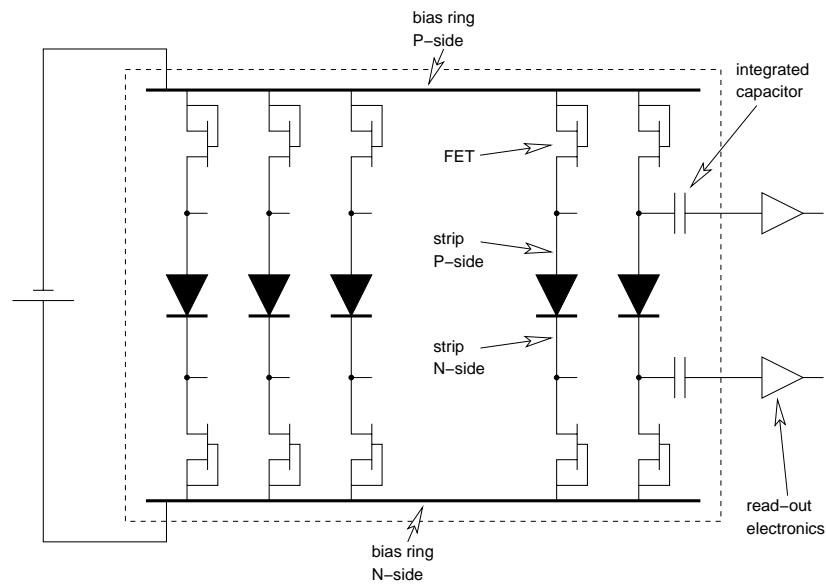


Figure 3.7: Electrical diagram of a double-sided strip detector. For clarity the integrated capacitors and read-out electronics are only depicted once.

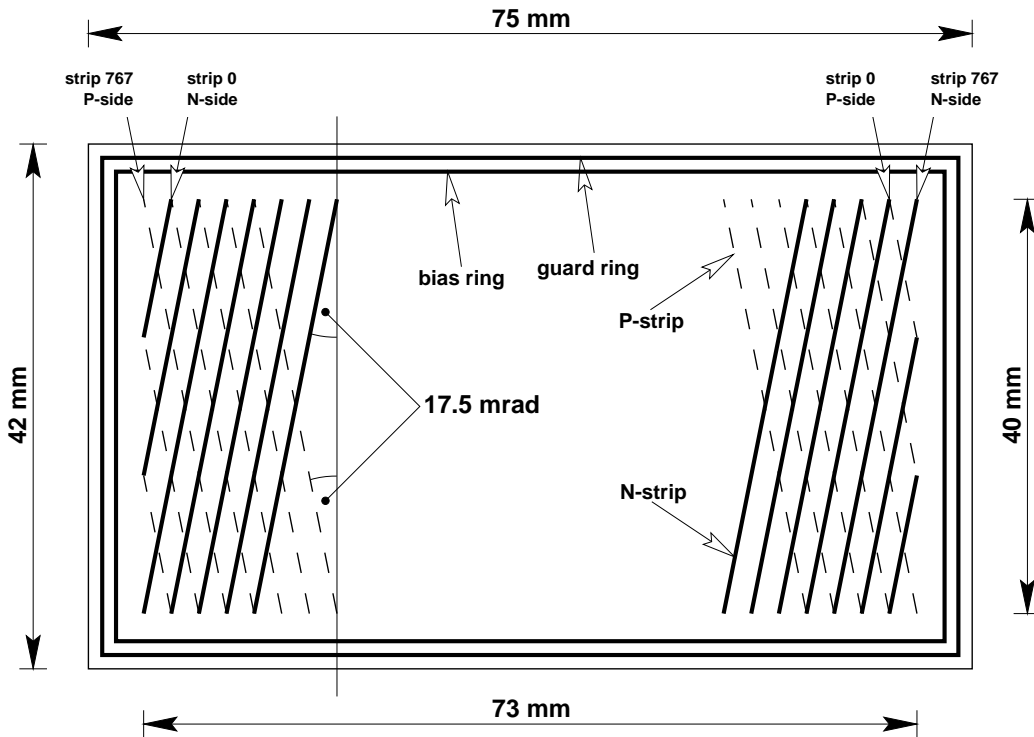


Figure 3.8: Layout of a silicon strip detector, as seen from the N-side. The strips on the N-side are drawn as solid lines, while the strips on the P-side are indicated with dashed lines (the angle is not drawn to scale).

separates the leakage current of the strips from the input signals of the read-out chip. The capacitor furthermore enables an AC coupling of the detector with the electronics. To protect the detector against electrical, chemical and mechanical damage a passivation layer finally covers the complete surface. The same structure is made at the Ohmic side (N-side). On this side though the strips are N+ doped and they are insulated from each other by P+ doped stops. The active surface is surrounded by two heavily doped implantates: the guard ring which separates the active area from the edges of the detector, which might have been damaged by the cutting process, and the bias ring which guides the operating voltage to the strips. This can be seen in the electrical diagram which is shown in figure 3.7.

Each detector-side has 768 strips implanted and they are tilted by a small angle (see fig. 3.8). By combining strips from both sides it is possible to extract two-dimensional information from hits. In order to keep the resolution the best in the direction of the bending plane, the strips are tilted with respect to the vertical direction by a small angle of only 17.5 mrad. This amounts to a stereoscopic angle of 35 mrad between a strip from the P-side and one from the N-side and gives a RMS resolution of at most $\approx 27 \mu\text{m}$ in the horizontal direction. Due to the analogue readout this

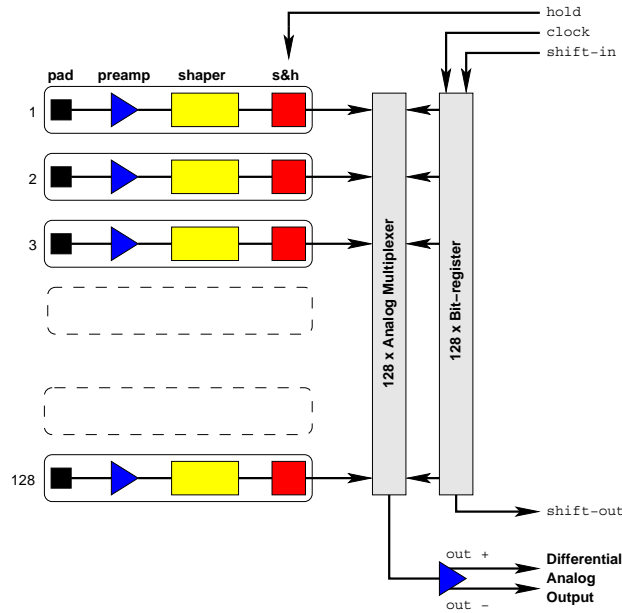


Figure 3.9: Working principle of the VA chip.

resolution is even better, since the charge distributed over different strips enables a more precise hit reconstruction (see section 4.2.3). For the vertical direction this implies a resolution of about 1 mm. The values for the resolution in the Y-direction and Z-direction are set by the requirements on the precision of the ALICE inner tracker [44]. The strips are numbered from left to right and counted from 0 to 767. The seven strips on the left have a smaller length than the other, but are still read out. This is not the case for the seven strips in the right lower corner (strip 768-774) which can not be connected to the read-out chips.

The strips are readout by the Viking VA chips [47,48], whose working diagram is depicted in figure 3.9. The VA consists of 128 identical parallel charge sensitive amplifiers. Each channel will integrate the signal collected from the detector for about $1 \mu s$. After this period (the peaking time), the `hold` signal is applied to sample the value. The output of each channel then enters a 128 channel multiplexer, whose switches are controlled by a bit register which runs in parallel. A `shift-in` activates the output bit register which is steered by the `ckb` clock signal. The output of the multiplexer goes directly out of the chip via the output buffer: the signal is distributed over a positive (`out+`) and negative (`out-`) differential output. After all channels are readout a `shift-out` is generated which stops the read-out process.

This process is repeated for all 6 chips of one side, where the `shift-out` of the preceding chip is the `shift-in` of the new chip read out. The first `shift-in` is provided by the *sequencer*, which steers the whole readout of all detectors after it has received the trigger signal. After all chips at one side have been read-out the final (`out+`) and (`out-`) output signals are composed

of the 768 sequential signals of one detector side. These two signals are sent to an Analogue to Digital Converter (ADC), where they are combined. This is steered by the `convert` signal from the sequencer.

The digital values from the ADCs are read out by a VME processor, which is controlled by the central data-acquisition system. In order to limit the amount of data and to select only the most interesting hits, a hardware threshold is set by the DAQ. This threshold is typical for each strip and its determination is described in subsection 4.2.1.

In the next chapter it will be shown how the data collected from the silicon telescope will be used to perform the off-line track reconstruction.

4

Track Reconstruction

The NA57 experimental setup has been designed to measure strange particles. In order to translate the information extracted from the detectors to the characteristics of physical particles an off-line reconstruction of the raw data has to be done. This is divided in two parts: first the hits recorded in the detectors are translated to tracks of the particles and the momenta of these tracks are determined. This reconstruction part is performed by the program ORHION (**O**mega **R**econstruction code for **H**eavy **I**ON experiments [52]). The information on the track momenta which is stored by this program is then used in the second phase where the particle identification is done. This analysis, which is done by the ANALYZE program, is discussed in the next chapter. In this chapter the track reconstruction done by ORHION is described, which is the subject of section 4.1. The micro-strip detectors (see section 3.2.4) were no part of the WA97 setup and since their characteristics are different from the detectors used before the ORHION reconstruction code had to be adapted. The implementation of the micro-strips in the ORHION code is described in section 4.2

4.1 Track reconstruction in ORHION

The tracking device in NA57 consists of the telescope, which is divided in two parts: the compact part and the lever arm. The track recognition is performed only in the compact part of the telescope. The lever arm is used to improve the momentum resolution of the higher momentum tracks found by the compact telescope. The reconstruction program ORHION has been designed to perform these two tasks. Its track finding algorithm is based on the following idea: because it is not possible to detect the multi-strange particles themselves with tracking, it is easier to find them indirectly i.e. to reconstruct them by finding their decay products. These decay products are charged and therefore their momentum can be determined by applying a magnetic field over the detector setup. When the charged particles traverse the detectors their curved trajectories can be followed. An example of a hyperon decay can be seen in figure 4.1, where the decay of an Ω in a magnetic field is rendered schematically. In order to reconstruct the Ω , first two oppositely charged decay tracks of the Λ have to be combined. This resultant Λ has to be recombined with the K^- track to yield the Ω . The decay of the Λ in this picture is called a V^0 decay. There are two possible decay topologies: the cowboy and the sailor topology which are schematically drawn in figure 4.2. The case shown in the Ω decay is the cowboy topology. In the case the decay particles do not have their tracks pointed at each other one has a sailor topology. In these topologies the

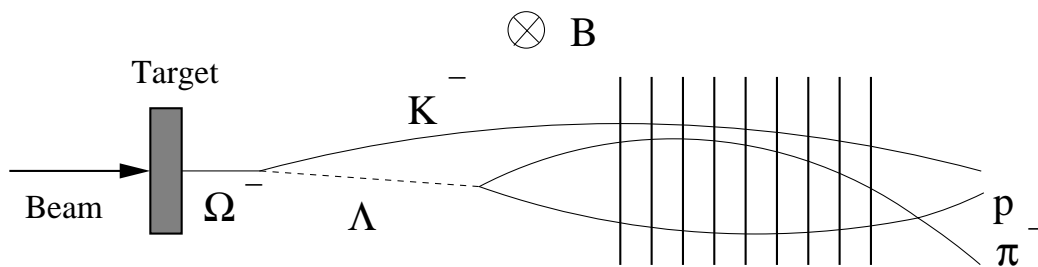


Figure 4.1: Decay of an Ω into charged particles inside a magnetic field. The tracks of the charged particles are crossing the silicon telescope.

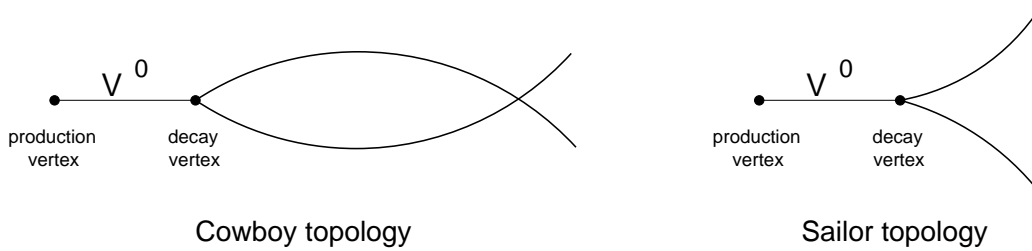


Figure 4.2: *The Cowboy and Sailor topology of a V^0 decay.*

point of decay is called the decay vertex or secondary vertex, where the point of the production of the main particle is the production vertex or primary vertex.

In the NA57 experiment only particles decaying in the cowboy topology are considered. This is due to the small acceptance of the NA57 detectors. ORHION first reconstructs all the tracks in the detectors from the hit information. Then all possible combinations of oppositely charged tracks are matched. By applying some rough selection cuts, a first sample of V^0 candidates is selected. In order to handle these different tasks the ORHION program consists of different subroutines which are referred to as processors. These processors are described briefly, after which the processors which are necessary for the track reconstruction are described in more detail.

The processors are:

- OR: this is the main processor, which steers the program.
- ST: this processor performs the track recognition in the compact telescope.
- XC: here the tracks found in the ST processor are extrapolated to the lever arm which contributes to the track fit.
- TF: this is used for track parameter fits and track extrapolations.
- V0: this performs the first selection of V^0 candidates.
- MD: multiplicity detector reconstruction.

Note that the TF processor is a service processor, which only provides utilities for other processors. In order to understand how the track reconstruction is done, the ST and XC processor are described in more detail. First the track recognition procedure in the ST processor is described in section 4.1.1 after which the use of the lever arm is discussed in section 4.1.2. The selection procedure of a first sample of V^0 candidates will be explained in section 4.1.3. The MD processor is responsible for the translation of the MSD detector hits (section 3.2.3) to information on the centrality of the collision. This analysis is independent of the strange particle reconstruction and therefore will not be presented in this chapter. The analysis of the MSD data is described in section 6.3. The assignment algorithm developed to include the micro-strips in ORHION is discussed in section 4.2.

4.1.1 Track recognition: the ST-processor

In the NA57 experiment only the hit information from the compact part of the telescope is used for track recognition. This part consists solely of silicon pixel detectors with a high granularity (see section 3.2.4). In these detectors hits of tracks are reconstructed from the pixels, small patches of silicon which are read out digitally. This means that only a hit is recorded when a signal larger than the threshold is measured. ORHION translates these hit positions to three-dimensional space points with a good resolution (in the order of tens of μm) and therefore a three-dimensional track-finding procedure can be utilized for the recognition of tracks. This track-finding procedure consists of a combinatorial approach: hits on the two outer planes of the compact telescope are combined to make candidate tracks in the non-bending direction. The hits on the inner planes are then used as a confirmation of the initially chosen pair of hits. Since most of the tracks come out of the target region, this combinatorial approach can also be used with the hits on the first plane replaced by the center of the target. By first searching for tracks with the center of target as constraint, many ghost combinations can be avoided and consequently in the track finding is started with this approach. In the following the track recognition will be described in more detail. After the two starting points have been selected the track finding is done in three steps:

- Step 1 Track recognition in the (X,Z) projection. Since this plane is parallel to the magnetic field direction, the projection of the tracks on this plane should follow straight trajectories. Hence the chosen hits are combined to define a straight line, which as a condition should have its slope in the acceptance range. The intersection of this straight line with the other planes is taken as a prediction and the closest hit on the pixel plane (i.e. within the resolution) is then assigned to the track. When the total number of hits assigned to a track is higher than a threshold the collection of points is accepted as a candidate track. This threshold is set at roughly 50% of the number of planes used.
- Step 2 Track recognition in the (X,Y) projection. The same procedure as done in step 1 is repeated, but since this projection is perpendicular to the magnetic field the tracks are curved. Therefore instead of a straight line a parabola is defined and in order to get a good first choice a third point is necessary. This point is chosen by drawing a straight line and then searching for a hit on a middle plane within a large acceptance window. When a hit is found a parabola is defined and with the predictions of this parabola on other planes matching hits are selected and a track is built.
- Step 3 Track matching. In the last step the track candidates in both projections are matched. This is done by checking whether the hits which defined the separate track projections correspond. When the number of shared points is larger than a threshold the track is accepted and a three dimensional representation of a track is left with its hits stored in a track bank. The size of the threshold is dependent on the number of planes in the Compact Telescope. For the Pb1998 and Pb1999 runs respectively 9 and 10 planes were used for the track finding. The minimum number of points for acceptance of a track was set to 7 for these runs. For the Pb2000 data the compact telescope comprised of 11 planes and the threshold was set to 8 hits. The hits, which are assigned to a track, are marked not to be used again.

The track finding method described above has the disadvantage that inefficiency in the starting planes (first, middle and last) can lead to the loss of good tracks. In order to recover the lost tracks,

the definition of first, intermediate and last plane is varied. So for example in the reconstruction of the Pb1998 data, besides the standard definition (1-5-9) for first, intermediate and last plane, also other combinations are used for track finding, for example 1-4-9, 2-5-9, 1-4-8 and 2-5-8. After the track finding has been completed, the collection of hits belonging to a track is fitted using a Quintic Spline Fit [55], which is implemented in the TF processor. The resultant fit parameters are also stored in the track bank.

4.1.2 The track improvement: the XC-processor

After the tracks have been reconstructed in the compact telescope they are extrapolated to the lever arm where points are added to improve the fit. This is done by the XC processor. In the Pb1998 experiment the lever arm consisted out of silicon pixel and micro-strip detectors. Because the micro-strip detectors were only for the first time employed, only the pixel detectors were used in the analysis of the 1998 data. In the following experiments only micro-strips were used in the lever arm. The resolution of the micro-strips is worse than that of the pixel detectors, so that a different extrapolation algorithm had to be used. In the following first the lever arm in the 1998 situation is described, after which the use of the micro-strips in the lever arm is explained.

The lever arm without micro-strips

In the 1998 data-analysis only pixel detectors were used for the lever arm. In order to assign hits of the pixel planes in the lever arm to extrapolated tracks the following method was used:

- 1 The first track is extrapolated from the telescope to the first pixel plane.
- 2 The distances between the extrapolation point and all hits in that plane are calculated.
- 3 All the hits within 3σ of the distribution of distances, calculated in the last step, are selected.
- 4 For each of the hits, selected in the last step, their space point is added to track bank, which contains the points of the preceding detectors. With this new hit, a new track fit is performed. The hit which gives the best fit (the smallest χ^2 value) is finally selected.
- 5 The selected hit is kept in the track bank and this best new fit is extrapolated again to the next detector and the procedure described above is repeated again. Note that when no hit matches the selection criteria, the track is extrapolated to the next detector available.

This hit attachment and new track fit procedure is done for each track. When the resultant track fit satisfies the condition $\chi^2/NDF \leq 2$ the track is stored for later analysis purposes and its characteristics are stored in the output DST-file.

The lever arm with micro-strips

During the data taking periods of 1999 till 2001 the micro-strips were functioning properly and could be used in the lever arm. Due to the lack of good pixel planes the micro-strip planes were the only planes used in the lever arm. Because of the fact that the micro-strips were a new type of detectors in the NA57 setup, the ORHION software had to be adapted. First the decoding of the raw data was added to the XC processor. For the pixel detectors this is done in the ST processor,

but in order to keep the alterations in the software concentrated in the software design, it was decided to implement all the micro-strip software in the XC part.

Furthermore because the micro-strip detectors give different hit information than the pixel detectors (like a poor Z-resolution of space points, calculated by combining strips from both sides), a direct cut on the distance between the extrapolation and hit candidate can give a problem at high hit multiplicities. Therefore a new hit assignment algorithm was developed by Alain Michalon. In the next sections all steps implemented for the use of the micro-strips are described in detail.

4.1.3 Reconstruction of V^0 candidates: the V0 processor

After the track reconstruction has been completed, a sample of tracks for each event is available. In order to find the decay of a neutral particle, a pair of two oppositely-charged particles has to be reconstructed. This task is performed by the V0 processor which uses the tracks stored in the track banks to make a first rough selection of V^0 candidates. The V0 processor sets some conditions which have to be satisfied by a track pair to be selected.

The tracks from this pair should originate from the same position: the *decay vertex*. By extrapolating the fitted tracks back to the target region it can be checked whether their closest approach is not too far away. This constraint should deselect the many random combinations which can be made by background tracks, like the ones originating from primary production vertex. The requirement on this distance is put at 1 mm for the first selection. It is also required that the *decay vertex* lies only between the target and the first plane of the telescope.

The V^0 candidates are stored again in ZEBRA banks [54]: the V^0 banks, which are also copied to the output DST. From the information in the DST-file a refined selection of V^0 candidates is done. This will be explained in the next chapter.

4.2 The micro-strips in the reconstruction software

4.2.1 Hit reconstruction

For the micro-strip detectors the hit information is stored as the strip number of the strip which is traversed by the track and the charge deposited by the track, stored as an ADC value. As there are two active sides per detector, for each track passing the detectors there are two strip numbers and ADC values stored. In the following the extraction of the hits out of this information is described.

First the hardware thresholds of the strips have to be determined. This is done by taking data during a period when there is no beam. In this way only noise will be measured. This noise is sampled 1000 times for each strip and with this sample the average value and the variation are calculated of the strip readout. The average value of the noise of strip j is called the *pedestal* P_j of that strip, and this pedestal has to be subtracted from the measured ADC signals of that strip. The variation of the pedestal is referred to as the *RMS value of the noise* N_j and it gives an indication of the noisiness of strip j . Both P_j and N_j are expressed in ADC units.

The typical value for the noise is dependent on the type of detector and the readout chip. For example for a detector with a VA2 chip the average value of the noise of a strip is 4 ADC units for the P-side and 6 units for the N-side of a double sided detector, as can be seen in figure 4.3. The fact that the noise of the N-side is higher than the P-side is characteristic for a detector with a bulk of N-type silicon. For detectors with the VA1 chip the amplifying capacity is half that of the

VA2 chip and thus all ADC values are decreased by a factor 2: for the P-side and N-side the RMS values are 2 and 3 ADC units respectively.

For some strips in figure 4.3 the values of the noise are clearly lower than the average of the distribution. These strips are not reading out a signal and thus are called *dead strips*. The main reason for this is failed bondings and because of this the charge deposited by a track is not recorded by the traversed strip, but flows to neighboring strips. This means that the ADC information is not lost and can be regained by clustering the hits, as will be explained later.

With these measured thresholds a hardware cut in the readout was made, in order to reduce the number of noise hits in the data sample. This cut required that the measured ADC value of a strip was above a threshold T_j , which was set to be equal to its pedestal plus a certain factor times the RMS value of the noise: $T_j = P_j + C_{RMS} \cdot N_j$. The factor C_{RMS} was dependent on the type of the data taken. For p-Pb collisions the hit multiplicity was low, giving a small dead-time for the strip detector readout. So less data had to be cut away resulting in a value of 2.5 for C_{RMS} . When the hit multiplicity in a collision was higher, like in Pb-Pb reactions this RMS cut was set to 3.5 in order to keep the dead-time at an acceptable level. At a value of 2.5 for C_{RMS} 95 % of the noise-hits are cut away and for each strip a Landau distribution should be seen for the real hits. In reality though, the tracks do not always traverse one single strip, but hit the detector in between two adjacent strips. This results in the signal being shared between these two strips. In order to determine the correct hit position and total signal, the information of adjacent strips has to be combined. This is done by forming a cluster, which is a row of consecutive hits on a plane. The position x of the cluster is then determined by using the center-of-gravity algorithm [49]

$$x_{\text{COG}} = \frac{1}{S} \sum_{i=1}^n S_i x_i, \quad (4.1)$$

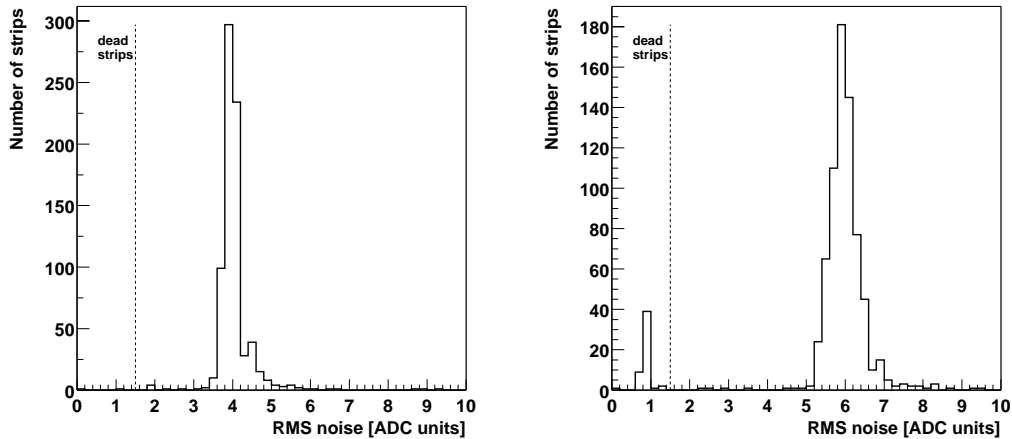


Figure 4.3: RMS value of the noise for strips on the P-side (left) and N-side (right) of a double-sided micro-strip detector. The RMS is expressed in ADC units.

where the sum runs over all strips i that are included in the cluster, with a cluster size equal to n . The term x_i is the position of the i th strip in the cluster and S_i is the signal on that strip, which is equal to the measured ADC signal minus the pedestal of that strip $S_i = ADC_i - P_i$. The total signal of the cluster is given by $S = \sum S_i$.

The presence of a dead strip in the sequence of strips belonging to a hit does not imply the breaking of the cluster: the charge deposited in the dead strip flows to the neighboring strips, which means that the ADC information is preserved. Due to the COG algorithm the x position of the cluster is shifted, which means that some precision is lost. During a calibration performed before the event reconstruction a list of candidate dead-strips is made, which is used in the cluster algorithm: when both strips next to the dead strip match the selection criteria the dead strip is included in the cluster.

Confining the selection criterium for the strip candidates for clustering to just the hardware threshold, one can determine the total signal with the COG method. Its distribution is depicted in the left-hand plot of figure 4.4. It is clear that there is an abundance of clusters with a total signal below 50 ADC units. This is an indication that there are still many noise hits in the sample. In order to reduce the amount of noise further the selection criteria for the strips in clusters are refined:

- At least one strip in the cluster is required to have a *Signal-to-Noise ratio* S_i/N_i which is larger than 5.0 for the P-side or larger than 4.0 for the N-side.
- The total noise and signal of the cluster is determined: the total noise of the hits is calculated by adding quadratically the individual noise values: $N = \sqrt{(\sum(N_i)^2)}$. The total signal of the cluster is given again by $S = \sum S_i$.
- The resultant ratio S/N of the cluster is required to be larger than 10.0 for the P-side and

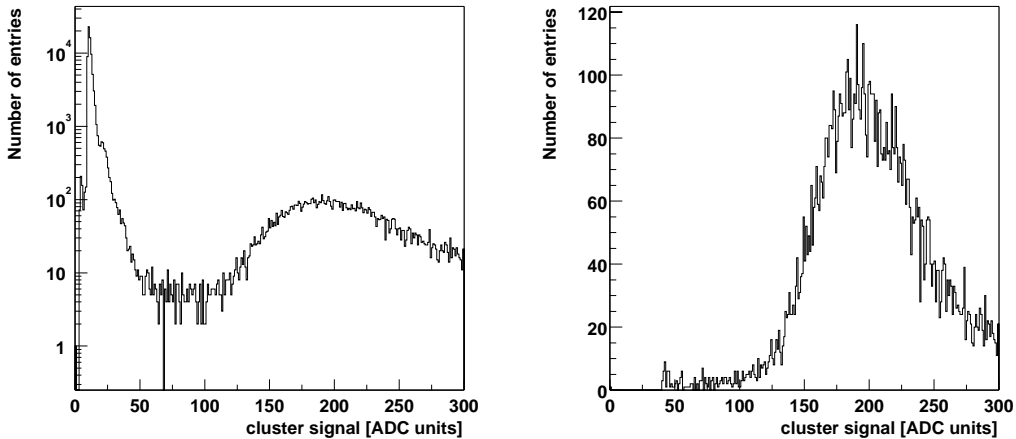


Figure 4.4: Total signal of the clusters in ADC units, before (left) and after (right) noise rejection, for a detector with VA2 chips.

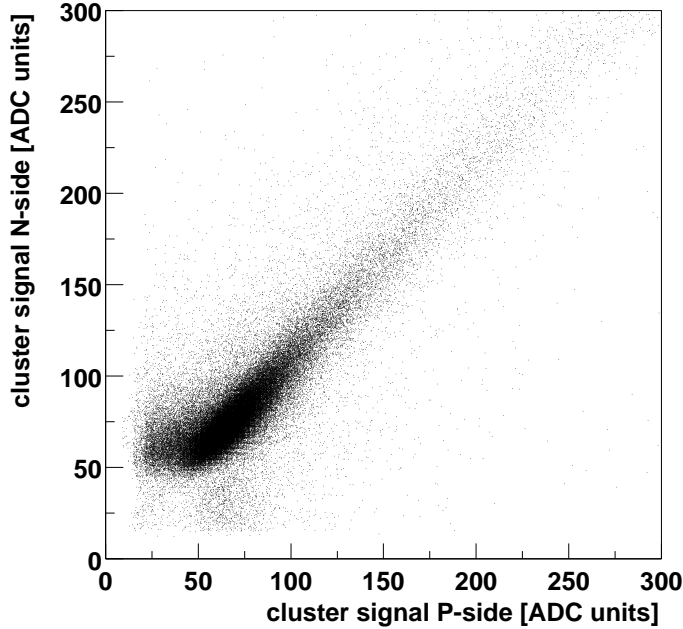


Figure 4.5: Cluster signal on the N-side versus cluster signal on the P-side of reconstructed hits for a strip detector with VA1 chips.

larger than 6.0 for the N-side.

After these requirements the noise hits are largely removed from the total signal distribution (see the right-hand plot of figure 4.4). The distribution that is left resembles a Landau distribution as expected and the peak value is around 200 ADC units. This is for a VA2 chip, while a similar distribution is obtained for a detector with VA1 chips, but then the peak value is at around 100 ADC units. Now it seems that real hits are selected it is interesting to look at the other side of the detector. The front and back of the detector measure the same signal deposited by a particle and thus their signals should be similar. This is the case as can be seen in figure 4.5 where a clear linear correlation is observed (note that this is for VA1 chips).

By combining the information of the two sides of the detector it is possible to reconstruct the position where the charged particle traversed the detector. This position can be calculated by using the measured strip numbers of the front (strip number F) and back (B):

$$y_{\text{hit}} = \frac{w}{2} (B - F) ; \quad z_{\text{hit}} = \frac{w}{2 \tan \alpha} (N + 1 - F - B) , \quad (4.2)$$

where F and B are integers in the range $0 - 767$. The value N is the total number of strips per side (768), $w = 95 \mu\text{m}$ is the pitch of the micro-strip detectors and $\alpha = 35/2$ mrad is the angle of the strips with respect to the vertical direction, also referred to as the stereo-angle. These detector

related values are stored in a HEPDB [57] database and extracted by ORHION when starting the reconstruction. The reconstructed hit positions are in the range $-73/2$ mm and $+73/2$ mm for y_{hit} and 0 to 40 mm for z_{hit} . Because in the formula the input are integer strip numbers the steps in y_{hit} and z_{hit} are discrete, with steps equal to $\Delta y = \frac{1}{2}w \cos \alpha \approx \frac{1}{2}w = 45 \mu\text{m}$ and $\Delta z = \frac{1}{2}w \sin \alpha \approx 2.6$ mm. When the charge is distributed over more strips and clusters are formed, the input values are not discrete anymore and thus the hit positions are smeared. In the following the position on the detector calculated from the strips of the front and the back are referred to as *space points*.

The disadvantage of this method is that when there are two hits, there are $2 \times 2 = 4$ possible hit positions, of which only two are the real hit positions. In order to reduce these ambiguities the overlap between strips of the front- and the back-side has to be restricted. Therefore the angle α is chosen to be small, which causes the resolution in the Z-direction to have less precision than in the Y-direction. In the case of the lever arm this is appropriate, considering that only an improvement of the track momentum in the Y-direction is required. Another way to deal with the ambiguities is to use *charge matching* [50]. As showed earlier in figure 4.5 there is a linear correlation between the front and back signal, so that demanding a signal of same magnitude for both sides will remove some ghost hits.

4.2.2 The hit assignment algorithm

As mentioned before, the compact telescope is the main detector used for the track recognition, performed by the ST processor. For every event all track candidates are stored in a track bank. In order to add points from the lever arm each of the stored tracks is extrapolated to the lever arm, where coincidences with the hits from the detectors have to be found. For the micro-strip detectors the method of global minimization of distances was introduced for this hit assignment. In the following all the steps in using the lever arm are described:

- Take the reconstructed space points of the first plane.
- Extrapolate all tracks to the plane (the first time from the compact telescope, the next times from the previous track refinement).
- Compute the Y/Z distances from each space point to each track extrapolation. By using the width of the distance distribution for the extrapolation of all tracks in one run (140M events) the hits within 3σ are selected.
- Perform a global minimization of these distances (with a larger weight for Y).
- Attach the space points assigned to a track when a new fit of the track gives $\chi^2 < 16$.

If there are some free tracks left and some free strips left:

- Compute the distance of each free strip to each track extrapolation. This distance is taken to be the projection on the strip of the extrapolated point on the detector and is calculated by:

$$\Delta = \frac{ay - z + b}{\sqrt{\left(\frac{1}{\tan \alpha}\right)^2 + 1}}, \quad (4.3)$$

where for the front side for a cluster with strip number F :

$$a = \frac{-1}{\tan \alpha}, \quad b = \frac{-\omega}{\tan \alpha} \left[F - \frac{1}{2}(N - 1) \right] + H, \quad (4.4)$$

and for the back side for a cluster with strip number B :

$$a = \frac{1}{\tan \alpha}, \quad b = \frac{-\omega}{\tan \alpha} \left[B - \frac{1}{2}(N - 1) \right] + H, \quad (4.5)$$

In these is H the height of the detector, which amounts to 4 cm. Again the accepted hits should lie within 3σ of the distance distribution of all tracks in one run.

- Perform a global minimization of these distances.
- Attach strips assigned to a track if a new fit gives $\chi^2 < 16$.
- Refit tracks with a new point added.
- Go to the next plane and repeat the procedure.

This method has been tested by simulating different types of particle samples and collisions. These simulations are performed using the GEANT program [56]. In this simulation package all the experimental conditions are copied to resemble reality as closely as possible. In order to achieve this, all information about the setup is extracted from the database. In these simulations the setup of the p1999 data was taken. In this experiment there were 10 pixel planes in the telescope and 4 double-sided micro strip planes in the lever arm (so a maximum of 8 hits per track for the lever arm). In the simulations particles and their hits can be tagged, which means that it is possible to recognize the original particles after the reconstruction and that their corresponding simulated hits can be matched to the ones found. In this way the reconstruction efficiency of this method can be tested. The results for different types of reactions are listed in tables 4.1 and 4.2. The first table lists the results for the old method, while the second table reports the results for the newly implemented method.

In the tables three possible reconstruction possibilities are given (only reconstruction is considered when the ST processor has identified a track):

Table 4.1: Percentage of hits assigned to simulated tracks for two different track samples, in case the original method is used.

Detection system	π^- (one track)	Pb-Pb (200 GeV/c)
Hits OK [%]	93	59
Missed hits [%]	2	30
Ghost hits [%]	5	11

Table 4.2: Percentage of hits reconstructed from the original simulated tracks for different track samples for the 'global minimization' method.

Detection system	π^- (one track)	Λ (two tracks)	p-Pb (40 GeV/c)	Pb-Pb (400 GeV/c)
Hits OK [%]	98	97	97	90
Missed hits [%]	2	3	2	6
Ghost hits [%]	0	0	1	4

- Hits OK: these are the lever arm hits assigned which correspond to the GEANT track hits
- Hits missed: hits belonging to a track but which have not been recorded.
- Ghost hits: hits that have been attached but which do not match the GEANT track hits (like noise or background).

The most simple track sample is the π^- sample where only one track per event is generated and it is required that this track reaches the first plane from the lever arm. For both methods the reconstruction efficiency seems to be reasonably good. The old method gives a correct reconstruction of 93%, while for the new method 98% of the correct hits were added to the track fit, which is somewhat better.

In the case of the Pb-Pb events at 200 GeV/c the old method gives considerable problems: only 59% of the hits are correctly attached and 11% is wrongly assigned. It is clear that the higher hit multiplicity (on average 16 tracks per event in this case) causes the old hit assignment procedure for lever arm data not to function well. In table 4.2 it can be seen that the global minimization method yields better results. This is shown for gradually increasing the complexity of the system. A more interesting case is that of the Λ sample. Here events with one track in the first micro-strip plane acceptance is required (2 tracks maximum). Furthermore an inefficiency of 1% and noise hits are introduced in the detectors. For this sample 97% of the hits are assigned correctly and this is still the case for the p-Pb collisions where some ghost hits start to be included (only 1%). Finally a large collision system is created with 400 GeV/c Pb-Pb collisions to really put the test to its limits. Even there the correct assignment is still 90%, and it gives an indication that for the experimental situation (beam energies of 40 and 160 AGeV/c and thus lower hit multiplicities) this method is reliable.

4.2.3 Track extrapolation results

In order to find hits in the lever arm belonging to a track, this track has to be extrapolated to each lever arm plane. As mentioned in the last subsection only those tracks are accepted for the global minimization procedure, that are within distance cuts. Hence before applying these cuts the detectors have to be aligned properly with respect to the telescope.

There are two ways to determine the alignment. The first is by using data from the so called alignment data. These data are taken before the run to determine the configuration of the detectors before the starting of the data taking. Furthermore extra data have been taken whenever a clear change in the set up of the experiment occurred, for example after a magnet trip in which the bench moved. These data can give precise information about the alignment because they were taken with the magnetic field off. In this way straight tracks can be reconstructed and with these the relative positions of the detectors in the telescope can be determined. After the tracks have been determined in the pixel telescope the tracks are extrapolated to the lever arm and by centering the distance of the closest hit distribution for each of the single detectors, the lever arm alignment is determined. The results for this alignment determination for the Pb1999 data are described in [51].

There are some disadvantages to this method: the alignment data which are taken can have low statistics (usually only some 100.000 events). In determining the tracks in the pixel telescope very strict cuts have been applied in order to use only the tracks of the best quality. So in this respect only a small sample of good tracks is selected. Because of the fact that these still have to be extrapolated to the lever arm makes that not all of these are within the acceptance of the micro-strips, so that not enough good tracks are left to obtain good alignment values. Furthermore the alignment data were taken only when there was a suspicion that something had changed in the setup. Unfortunately some changes in the setup occurred unnoticed so that no alignment data were available. Therefore a second method was developed where the tracks found by ORHION are used.

Here again the same procedure as in the first method is followed, only with the difference that the tracks are reconstructed in a magnetic field. This could cause the alignment to lose some precision, but comparing the alignment determined by the first method show that the alignment values agree within microns. The alignment values are stored in the database, where the whole run period was split into several alignment periods, because of some bench movements.

After the correction for the misalignment, the tracks are extrapolated again to the lever arm and the distances of all hits to the extrapolation can be considered for different cases. In figure 4.6 the distance of the extrapolated track to the reconstructed space points in the Y-direction is plotted. On the left hand side the distance distribution for the first plane of the lever arm is shown, the right side gives the results for the second plane after the first plane has changed the track. In order to make a comparison between the two cases the same scale is kept for both distributions. When comparing both plots, it becomes clear that the distribution for the first plane has a bigger width than the second. This is due to the fact that the extrapolation error becomes bigger when the extrapolation distance is bigger. In the extrapolation to the first plane the distance is around 30 cm, while to the second plane this is only 2 cm. Furthermore, for the second extrapolation a hit is already attached in the first plane and therefore the track-fit has been improved already. The extrapolation error can be introduced by two reasons: the momentum of the fast tracks from the telescope can have a large uncertainty, due to the fact that their curvature is not well determined in the telescope. It is the task of the lever arm to improve these momenta. A second reason could be the fact that the value of magnetic field near the lever arm is not determined as precisely as in the center of the magnet (near the telescope). The complete ORHION extrapolation consists of parts of smaller extrapolation steps where the local field values are used for every extrapolation step. Near the lever arm the precision of the field could be less well known than the step size requires. The latter effect will be seen when the residuals are determined. Because the extrapolation distribution is much wider for the first plane the selection cuts for attachment of the strip is 2 mm for the first

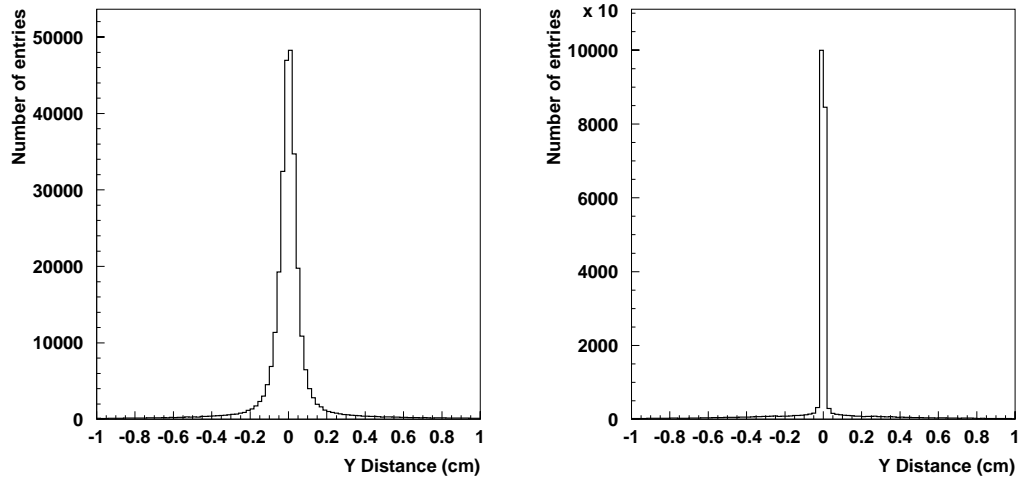


Figure 4.6: Distance between track extrapolation and reconstructed space point for the first lever arm detector (left) and the second (right) in the Y-direction.

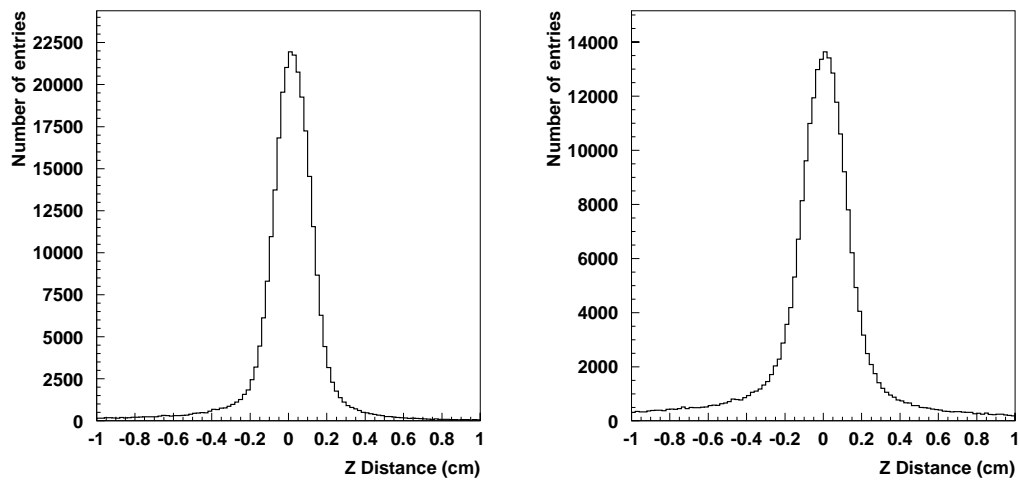


Figure 4.7: Distance between track extrapolation and reconstructed space point for the first lever arm detector (left) and the second (right) in the Z-direction.

plane and $200\ \mu\text{m}$ for subsequent planes.

The results in the Z-direction can be seen in figure 4.7. They do not differ much for the first and second plane, but the width is greater than for the Y-direction due to the poorer Z-resolution. For both planes the acceptance cut was put at 3 mm.

When no space points could be attached coincidences with the clusters on the single sides of a detector are used. The extrapolation distances are shown in the plots in figure 4.8. The plot on the left hand side gives the distribution of the front side of the first detector. Two side peaks can be seen next to the central peak. These peaks can be explained by the fact that the cut for the space point acceptance was at 2 mm for the Y-direction and all strips of the hits which were not accepted are again matched for the incoming tracks not adapted. Since the inclination of the strips is almost vertical, the Y-distance of the projection of the point on the strip must be almost equal to the Y-distance of the space points. Therefore these must be cut out again and therefore the cut for acceptance is set at the same value as for the space point attachment. It is also clear that the width of this peak is larger than for the space points. Because there is no Z-information it is possible to accept a background or noise hit which is at the same Y-coordinate but in a different Z-region. Therefore the background in the distribution is higher and this method is less reliable. For the next plane in the lever arm the distribution is nicely peaked so for this case the acceptance cut is put also at $200\ \mu\text{m}$. The background seems also higher here than for the case of the space points so also here the Z-uncertainty has some effect. Still the 'global minimization' method is able to reject many background hits. During the lead runs many delta rays were detected by the micro-strip detectors. These rays consist of electrons knocked out of the air molecules by the heavy ions of the beam. The negative charge of the electrons makes that they all are bent to one side of the detector by the electric field. Their presence in the overview of the total number of hits

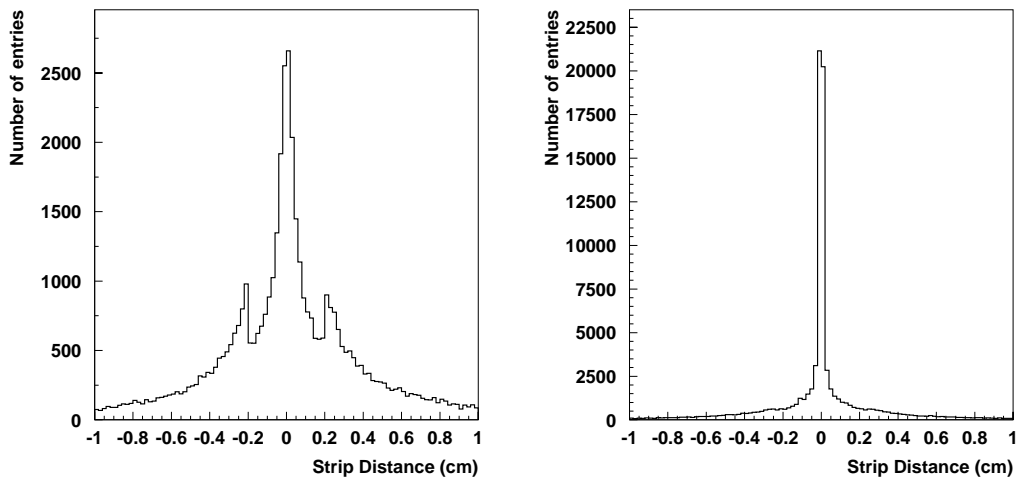


Figure 4.8: Distance between track extrapolation and the strip hits on the front side for the first lever arm detector (left) and the second (right).

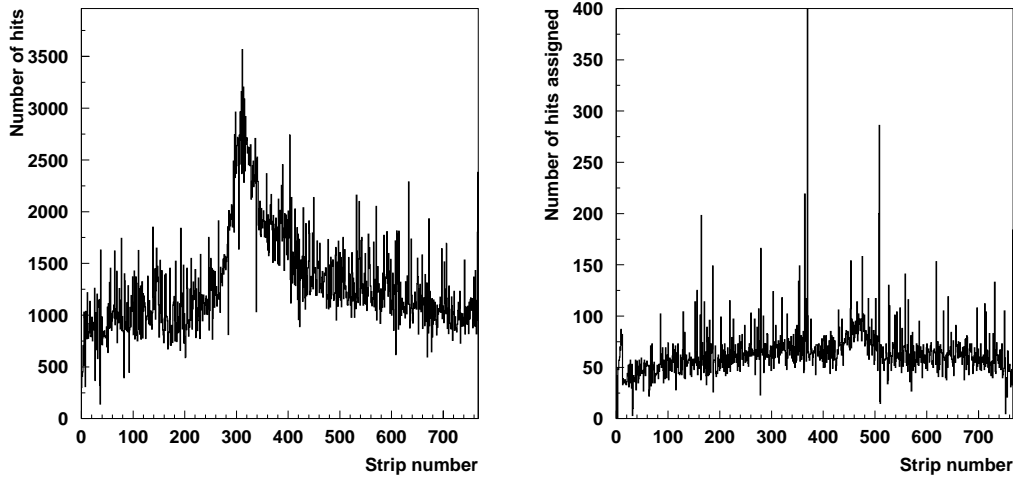


Figure 4.9: Number of hits for each strip of one plane for all hits (left) and the number of hits for each strip for only those hits assigned to tracks (right).

per strip can be seen in the left plot of figure 4.9. In the right plot the number of hits per strip is given again, but now only for the hits which are attached to the tracks. As expected an almost flat distribution can be seen.

After the hit assignment procedure has been done for all planes in the lever arm and all new added hits are stored in the track bank, a final track fit is made. If this track fit has a good χ^2 (i.e. $\chi^2 \leq 16$), it is selected and written to the output DST. With the new fit-information the trajectory of the track can again be followed through all detectors and the distance of the final track to the points added in the track bank can be calculated again. In this way a check can be made to which amount the attached hits match the tracks. These distances are called 'residuals'. When the Y-residuals are plotted though, there seems to be a problem: there are two peaks shifted away from each other with respect to the center of the plot. When the residual for a track is plotted versus the track momentum it becomes clear that the residuals are split up in a residual distribution for the negative tracks and one for the positive tracks, which are shifted with respect to each other. This can be seen in figure 4.10. This effect is called *over-steering* and could be due to the problem mentioned earlier that the field is known with less precision in the off-center region. Another reason could be that the uncertainty in the position of the detectors is such that misalignments occur in the reconstruction. In order to correct for this effect we have to shift the detector positions artificially in the beam direction by applying a shift, a so called X-alignment. The detectors have to be shifted such that the positive and negative tracks intersect at the same position. For the Pb1999 data the first detector had to be moved 7 mm towards the target, while the shift done for the second and third detector was about 5 mm.

After the X-alignment correction for all detectors the residuals give a nicely peaked distribution (see fig. 4.11). By applying a Gaussian fit to these residual distributions their width could

be determined. The results of the fits are listed in table 4.3 for all the assignment options. For the Pb1999 data the space point resolutions are as expected. For a digital readout of the strips the resolution should be $d/\sqrt{12} = 27.4 \mu\text{m}$, where d is the pitch of the strips. For the analogue readout the precision should be better, but due to noise, precision loss due to dead strips and some small uncorrected over-steering effects, this resolution can become worse. In the light of this, the measured values of 28 and 20 μm , for the first and the second plane respectively, for the Y-resolution of the space point residuals is as expected. For the single side residuals the resolution is worse: the precision is deteriorated because not the Y-distance is taken but the projected distance on the strip. Furthermore more noise and background hits are selected due to the larger extrapolation uncertainty, which also blurs the distribution. This can be seen the left hand side of figure 4.12, where clearly more background is accepted. For the second plane the background is still higher than for the space point residuals but is already much better because the track extrapolation uncertainty has decreased considerably. For the backside of the second detector the resolution is larger than for the front. This is due to the fact that the this side has a blind spot, caused by a too low bias voltage applied to the detector. By keeping the bias voltage too low, no complete depletion could be established in the detector and therefore a part in the middle of the p-side gave no signals.

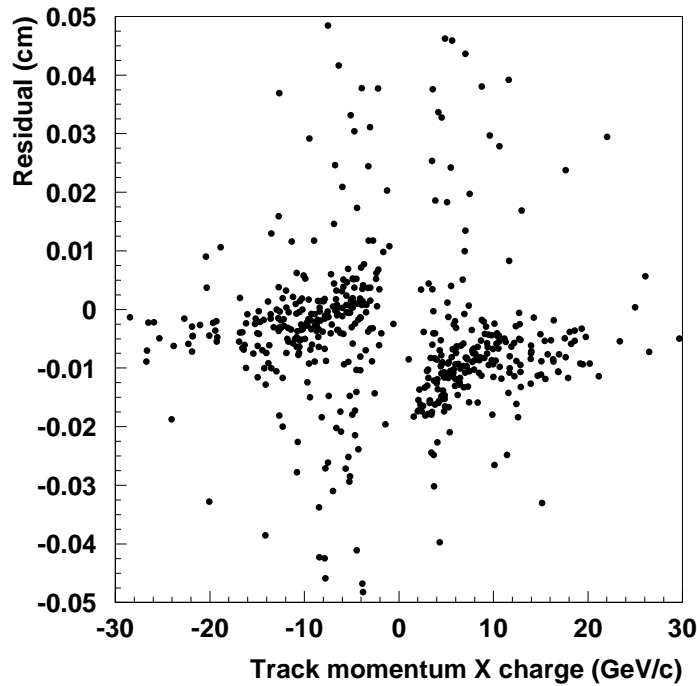


Figure 4.10: *The hit residual for a track versus its momentum times its charge. For low energy particles the residuals tend to diverge.*

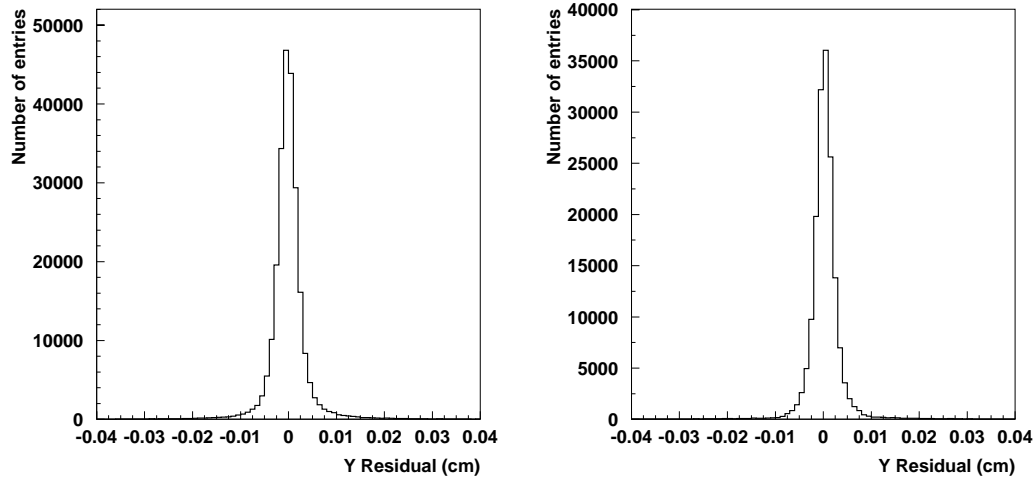


Figure 4.11: Track residuals of reconstructed space points for the first lever arm detector (left) and the second (right) in the Y-direction.

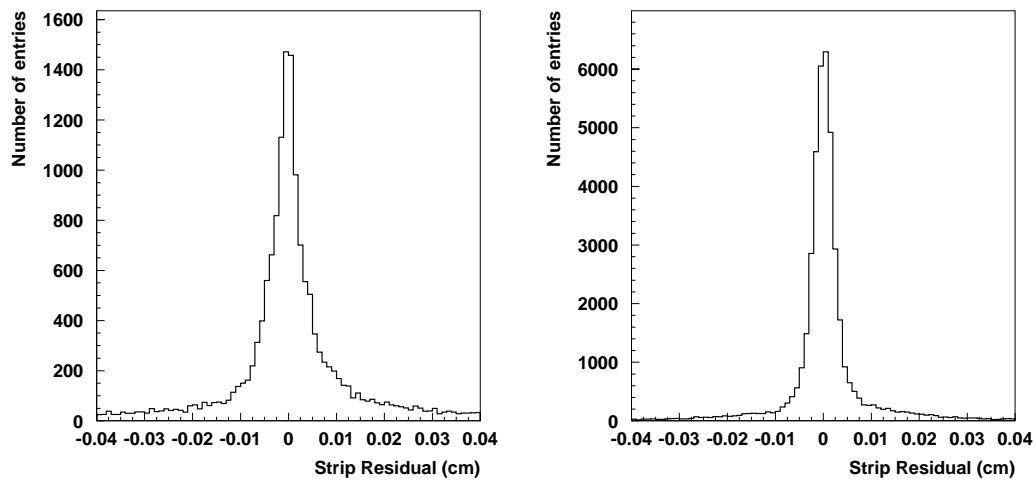


Figure 4.12: Track residuals of strip hits at the front side for the first lever arm detector (left) and the second (right).

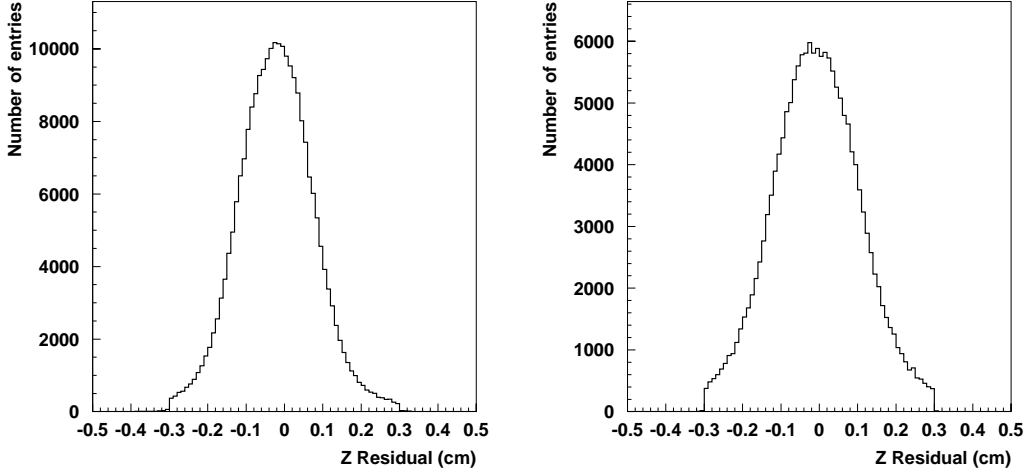


Figure 4.13: Track residuals of reconstructed space points for the first lever arm detector (left) and the second (right) in the Z-direction.

For the Z-residuals results are shown in figure 4.13. There is not much difference between these residual distributions, mainly because the Z-information is used for hit selection purposes, but does not contribute to the improvement of the fit.

In table 4.3 the results for the Pb2000 data are also given. Here three double-sided micro-strip detectors are used for the lever arm analysis. Before discussing the results listed in the table it must be mentioned that the distance from the telescope to the lever arm is almost the same in the

Table 4.3: Values of the width obtained by a Gaussian fit of the residuals for space points (σ_y and σ_z) and for single strips (σ_{front} and σ_{back}). Both the results for the Pb1999 and Pb2000 runs have been given.

Lever arm detector (Run)	σ_y [μm]	σ_z [μm]	σ_{front} [μm]	σ_{back} [μm]
1 (Pb 1999)	22	984	41	44
2 (Pb 1999)	20	1013	24	43
1 (Pb 2000)	25	902	62	69
2 (Pb 2000)	23	826	59	65
3 (Pb 2000)	27	896	45	54

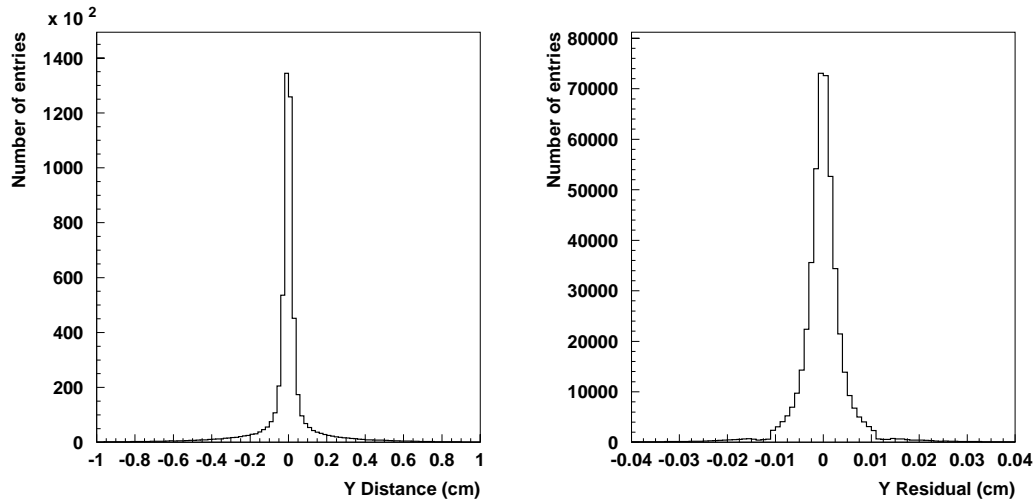


Figure 4.14: The distance between the track extrapolation and the strip hit at the front side of the first detector in the lever arm (left) and the resultant residual (right). These are distributions determined for the Pb2000 reference run.

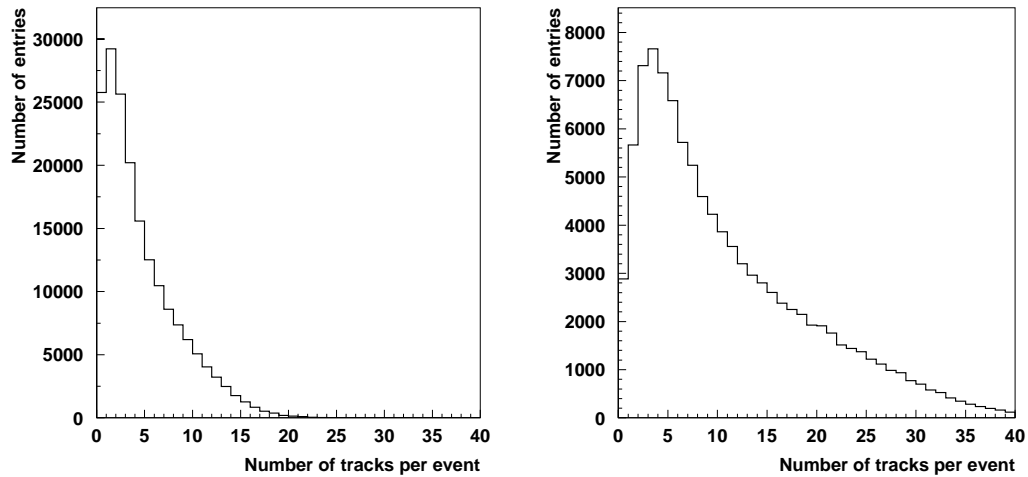


Figure 4.15: Number of measured tracks in the telescope per event for the reference run of the Pb1999 data (left) and Pb2000 data (right).

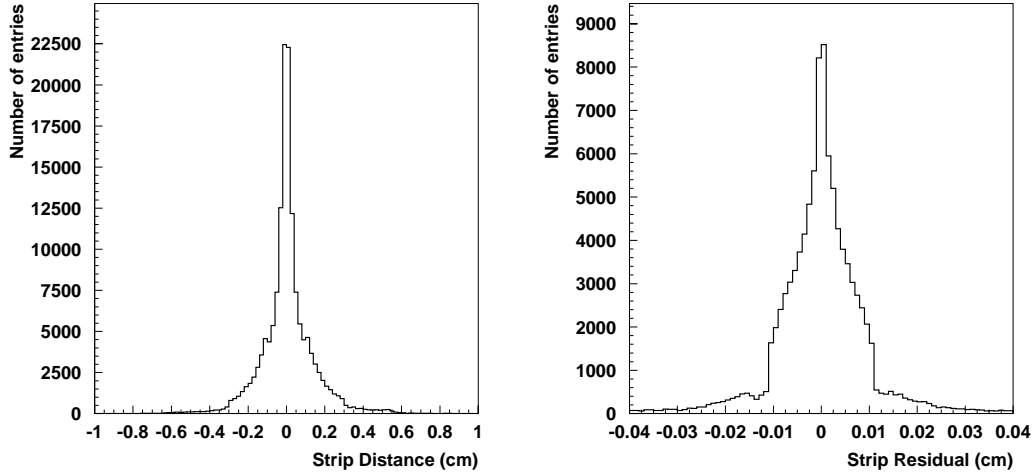


Figure 4.16: *The distance between the track extrapolation and the strip hit at the front side of the first detector in the lever arm (left) and the resultant residual (right). These are distributions determined from the data of the Pb2000 reference run.*

Pb1999 and Pb2000 (ca. 30 cm) setup. Surprisingly the width of the distribution of the distance extrapolation to the first plane is smaller than for the Pb1999 case. A reason could be that the performance of the telescope for the Pb2000 run is better than for the Pb1999 data, due to the fact that for the former 11 pixel planes were used, while for the latter only 10 were placed in the compact telescope (see appendix A). Therefore the momentum resolution was determined more accurately, due to the addition of an extra Y-plane. The width of the distribution for the Pb2000 data is almost twice as small as for 1999 (see figure 4.14). Therefore the cut on the first plane is put at only 1 mm (which is about 3σ). The distance between the detectors themselves is somewhat different: 4 cm for the Pb1999 setup, 2 cm for Pb2000, but it is too small to give very different extrapolation results. What can also affect the hit assignment is a different number of tracks reaching the NA57 detectors, due to different beam energies. This can be seen in figure 4.15. On the left hand side the number of tracks measured in the telescope per event for the Pb1999 run is displayed giving an average of 4.1, at the right side for the Pb2000 run which has an average of 10.4 tracks per event.

As was seen in the discussion on the simulation tests of the 'global minimization' method, the number of correct hits attached decreases with the increase of the collision system and energy. So it is expected that the increase of number of incoming tracks decreases the hit assignment efficiency. This results in a large number of background hits to be added and this should be seen in the residuals. For the space point residuals this is not observed: the residuals have the same width as for the Pb1999 case. For the strip residuals though the widths are larger by 50%. Because no Z-information is available, these distributions are sensitive to the background and thus are influenced more for the 2000 data. This is shown in figure 4.16, where the plot of the

distance between extrapolation position and strip hit is shown (left) next to the plot of the resultant residual distribution (right). These effects therefore also should influence the track improvement efficiencies. The results for the efficiencies of the detectors for the two lead runs are described in the next paragraph.

4.2.4 Reconstruction efficiencies

The list of the hit attachment results are given in table 4.4. The percentages shown are calculated for the reference run. In the first column the percentage of hits, which are assigned to a track for the space points is given. The tracks which are selected for the hit assignment are not only the ones which fall within the first plane acceptance, but there is an extra tolerance of 0.3 mm in the Z-direction because of the poor resolution, and a tolerance of 95 μm in the Y-direction because of the extrapolation uncertainty. So it is possible that some tracks are assigned by this which give no hits.

In the first plane the percentage of space point hits attached is 83%, while in the second this is only 65%. The reason for the lower hit attachment of the second plane is because the bias voltage was not high enough. This caused a part of the silicon not to be depleted, resulting in a dead region at the front side of the silicon. No space points could be formed there. The absence of space points in that region can be compensated by looking at the strip hits. In the second column it can be seen that the front side assigns more hits to incoming tracks than the back, therefore compensating the loss of space points. When the reconstruction efficiencies are added for all possibilities the total percentage of hits which have been assigned is 97% for the first plane and 88% for the second. It is important to realize that it is possible for a track to have two hits assigned at the single sides, while there is no space point reconstructed there. For example a space point which was within the Y-direction cut, but which did not lie within the tolerated Z-cut, gives for the strip assignment method two possible candidates. Therefore the addition of the efficiencies of all assignment possibilities can give an overestimation of correctly attached hits. Whenever the new fit of the track has a χ^2

Table 4.4: Percentage of hits assigned to incoming tracks reconstructed in the compact telescope for the space points and the strips for each side (F/B). Also listed is the total percentage of tracks, in the acceptance of the lever arm detectors, adapted by the lever arm.

Lever arm detector (Run)	Space point efficiency [%]	Strip hit efficiency [%]	Total tracks adapted [%]
1 (Pb 1999)	83	7/7	94
2 (Pb 1999)	65	17/6	
1 (Pb 2000)	83	-	92
2 (Pb 2000)	75	-	
3 (Pb 2000)	63	-	

which is too high the track will not be changed. Taking into account the arguments mentioned above the total percentage of adapted tracks of 94% seems reasonable.

For the Pb2000 data, the attachment of strips to tracks gives problems, as was shown already in discussing the track extrapolation results. Therefore only the constructed space-points were matched to the incoming tracks. The attachment efficiencies for the Pb2000 data are also listed in table 4.4. The first two detectors listed correspond to the detectors used for Pb1999. The attachment efficiency of the first detector is the same for both run periods: 83%. The second detector shows a larger efficiency of 75%. This is due to the fact that the bias voltage was increased, which caused the dead-region to disappear. The last detector has attached hits to only 63% of the incoming tracks. This is due to the absence of a readout chip in the back-side of the last detector, which decreases the number of space points by $\frac{1}{6}$, corresponding to 13%. The total percentage of adapted tracks here corresponds to 92%, which is about the same as for Pb1999. Since for the Pb2000 run only the space points were used, the argument of hits assigned wrongly by single strips is not valid anymore. The tracks not adapted then only could be ghost tracks, which do not have hits in the lever arm and hence can not be found back in the detectors. In order to check what the intrinsic efficiency of the detectors is another method has been applied. This method is used by the PLANEFF program which is designed to measure the chip efficiencies of the pixel and strip planes.

Plane efficiencies from the PLANEFF program

In the PLANEFF program the efficiencies are determined in the following way: in order to find the efficiencies of a detector the track reconstruction in ORHION is repeated but now with the plane, which is under investigation, left out. After the tracks have been reconstructed they are extrapolated to the plane left out and with this prediction the closest hit within the same cuts as for the reconstruction is looked for. In case the plane looked for was a micro-strip detector an extra demand was made: only those tracks were considered which had at least one hit in one of the other detectors of the lever arm. In this way the ghost tracks could be discarded. The efficiencies of the separate chips of the detectors determined by the PLANEFF program for the Pb2000 data are listed in Appendix A. The global efficiency of the planes ranges from 94-96%. These results are in agreement with the performance of the micro-strip detectors for the Pb1999 data [51], where alignment data were used for determining the detection efficiencies of the micro-strip detectors. With these alignment data, a selection of qualitatively good tracks was used and efficiencies of 96-98% were found for the single sides of the detectors. It must be stressed that because of the demand of qualitatively very good tracks only parts of the silicon telescope were used and hence only a part of the micro-strip detectors was probed. These values for the efficiencies are an indication that the micro-strips detectors have worked well during the data taking and that they manage to correct almost all incoming tracks. In the next section the effect of the improvement of the track momentum will be investigated by looking at the invariant mass distributions of the reconstructed particles.

5

Reconstruction of Λ , $\bar{\Lambda}$ and K_S^0 particles

5.1 V^0 selection procedure

The particle selection in the analysis is performed by taking a second look at all the V^0 candidates stored in the V^0 banks of the ORHION output. This sample still consists of many random combinations of oppositely charged tracks and in order to get rid of this background all V^0 candidates have to satisfy tighter decay variable cuts. These decay variables will be introduced in section 5.1.1. In section 5.1.2 it will be shown that different particle types can be selected by applying kinematical cuts. Finally in section 5.2 for the three lead data taking periods the final particle samples will be presented and for the Pb1999 and Pb2000 data samples the results of the addition of the micro-strip lever arm will be shown.

5.1.1 Variables of a V^0 decay

In figure 5.1 a schematic view of a V^0 decay is shown. Keep in mind that in the NA57 definition, the beam direction is taken as the X-axis, while the Z-direction is taken in the direction of the magnetic field. The Y-axis is then chosen to give an right-handed coordinate system.

Combining the momenta of track 1 and track 2 the original V^0 momentum can be reconstructed. This momentum is indicated by the large dark arrow: $\vec{p}(V^0) = (p_x, p_y, p_z)$. The position of the closest approach between the two tracks is taken as the decay position and is called the secondary decay vertex $x(V^0) = (v_x, v_y, v_z)$. The distance of the closest approach between the tracks is referred to by Δ . The back extrapolation of the V^0 momentum to the target plane gives the impact parameters b_y and b_z (indicated by the dashed line), which are the distances between the impact position of the V^0 and the beam impact position. The beam impact position, which is referred to as the primary vertex position, can be determined in different ways:

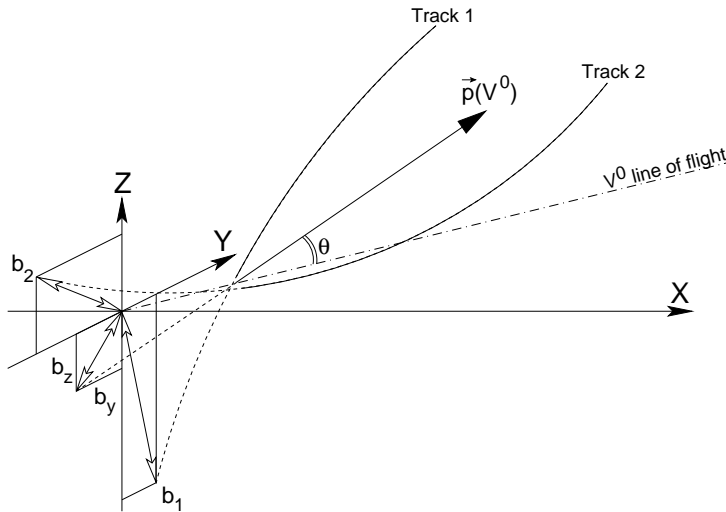


Figure 5.1: Schematic drawing of a V^0 decay, indicating the impact parameters and the line-of-flight.

- *Survey vertex position:* This is a general position which is the same for the whole set of data of one period. It is measured mechanically for the X-position and the Y- and Z-positions are taken as the nominal position.
- V^0 *vertex position:* This is the beam position determined by extrapolating all V^0 candidates of one run back to the target plane and taking the average position.
- *Event-by-event vertex position:* This position is determined by taking all tracks from one event and removing all tracks belonging to a V^0 candidate. All remaining tracks are then extrapolated back to the target plane and after rejecting the tracks which fall too far away from the central cluster, a final distribution of the impacts on the target plane is made. This distribution has in approximation a Gaussian shape and by performing a fit the mean and a variance can be determined. This method is the most accurate, but has the disadvantage that the method does not work for events with low multiplicity.
- *Run-by-run or Off-line vertex position:* This method follows the same procedure as for the event-by-event vertex, but in order to get rid of the low multiplicity events all tracks from all events of one run are considered. The resulting Gaussian fit gives the mean beam impact position and its variance.

Other variables which are useful to look at are the internal decay angles (see figure 5.2). In order to calculate these variables, the proton and pion momentum have to be transformed back to the center of mass frame of the Λ . In this system then the X' -axis is defined as the original direction of the Λ and the Y' -axis is chosen such that the (X', Y') -plane is parallel to the original (X, Y) -plane. The Z' -axis then is chosen to give a right-handed coordinate system. The angle of the proton in the (Y', Z') -projection is called ϕ and its projection on the X' -axis is defined as $\cos \theta_\Lambda^*$.

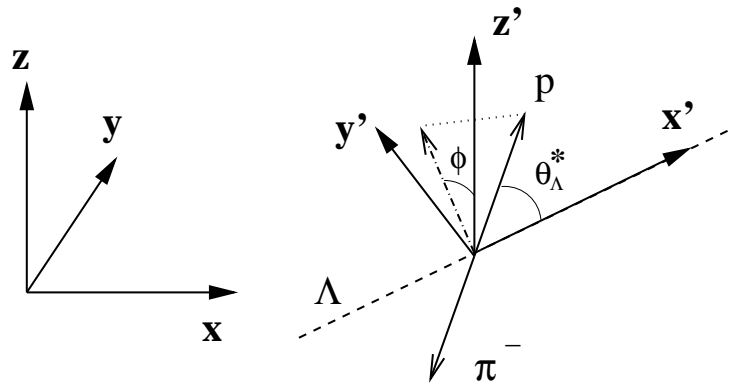


Figure 5.2: Definition of the internal decay angle ϕ in case of the decay of a Λ . In the left the NA57 laboratory system is drawn, to the right the center of mass system of the Λ with X' in the direction of its original direction of flight and the Y' -axis chosen such that the (X', Y') -plane is parallel to the original (X, Y) -plane.

5.1.2 Particle identification

NA57 has no means to determine the particle type directly and therefore another method has to be used to perform the particle identification. This method makes use of the Podalanski-Armenteros variable α . In fig 5.3 the decay of the V^0 candidate is depicted again. This time only the longitudinal and transverse components q_L and q_T of the decay momenta with respect to the direction of the V^0 momentum are indicated. With the longitudinal components of both the decay particles the variable α is defined:

$$\alpha = \frac{q_L^+ - q_L^-}{q_L^+ + q_L^-}, \quad (5.1)$$

where q_L^+ and q_L^- are the longitudinal momentum components of \vec{p}^+ and \vec{p}^- . In a two body decay this variable α and the transverse momentum q_T^+ can be used to distinguish between different hadrons [58]. When plotted versus each other ellipses can be seen in different regions, each typical for a hadronic type (see figure 5.4). In order to get an indication of where different particles can be found in the Podalanski-Armenteros plot, the 3 types of V^0 decays, looked for by NA57, have been simulated. The sample of $\bar{\Lambda}$ s gives an ellipse at negative values of α , while the Λ sample is depicted, mirrored with respect to zero. Due to the Lorentz boost, the momentum of the decay proton of the Λ , will always be larger than the decay π momentum. This will cause α to be positive for the Λ , while the $\bar{\Lambda}$ represents the opposite case, yielding a negative value of α . For the K_S^0 the case is different: it decays in two pions and on the average there is no preference for one of the pions to have a higher momentum. Therefore the average value of α will be zero and the particle ellipse will be formed around zero. For a large value of α , one of the decay particles needs to have a large longitudinal momentum, resulting in a small value of q_T . The maximum q_T can be reached if all the energy of the decay goes to the transverse momenta of the decay particles: e.g. the maximum for the K_S^0 is given by $q_T^{\max} = [\frac{1}{4}m_K^2 - m_\pi^2]^{1/2} = 206 \text{ MeV}/c^2$, as can be seen in

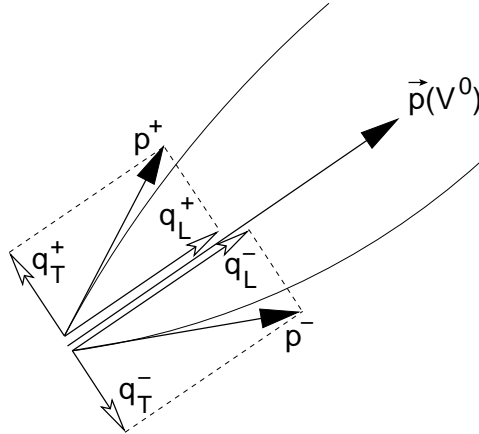


Figure 5.3: Transverse (q_T) and longitudinal (q_L) momentum components of the positively and negatively-charged track, with respect to the direction of the reconstructed V^0 momentum $\vec{p}(V^0)$.

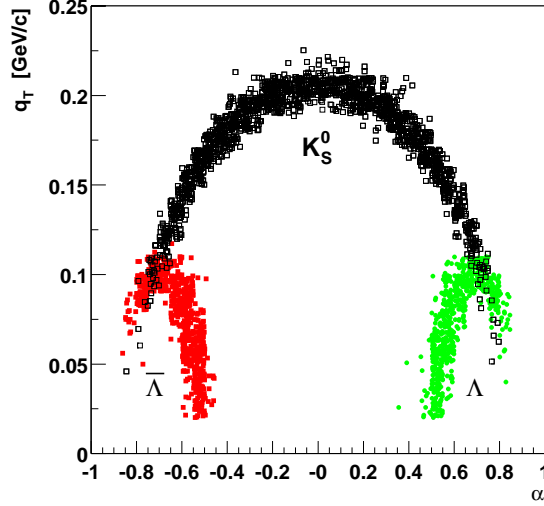


Figure 5.4: Simulated Podolanski-Armenteros plot with ellipses from $\bar{\Lambda}$, K_S^0 and Λ particles.

the Podalanski-Armenteros plot.

Unfortunately the Podalanski-Armenteros plot is not decisive of a particle type in some regions, because an overlap of particle ellipses occurs. In order to select only one particle type, for example the Λ , the overlap region with the K_S^0 has to be excluded for selection. This can be done by calculating two invariant masses for each V^0 candidate: $M(\pi^+, \pi^-)$ and $M(p, \pi^-)$ in case of a K_S^0 and a Λ respectively. This can be calculated by assuming the masses of the decay products to be that of the particle looked for:

$$M(V^0) = \left[(E_1 + E_2)^2 - (\vec{p}_1 + \vec{p}_2)^2 \right]^{1/2}, \quad (5.2)$$

where E_i and \vec{p}_i are the energy and momentum of the two decay products, $i = 1, 2$.

Then by imposing a cut on the value of the K_S^0 invariant mass it is possible to remove the K_S^0 ellipse. This can be seen in the left-hand plot of figure 5.5 which shows the Podolanski-Armenteros plot of the V^0 candidates. In the right hand plot the K_S^0 ellipse has been removed. Although this decreases the statistics of the Λ sample, the purity is enhanced greatly. This demand for high purity is required by the further analysis in NA57. The experimental setup has a distorted acceptance, which has to be corrected for by weighting particles or deconvolution (see chapter 6). Therefore since there is corrected for the limited acceptance and efficiency by these methods it is more important to achieve a high purity. In this way you will not correct the background.

In the next section the cuts, applied for the selection of different particle types are given for the different data taking periods. Since in this thesis only the lead runs are considered only these will be considered. The resultant invariant mass distributions will be shown and for the Pb1999

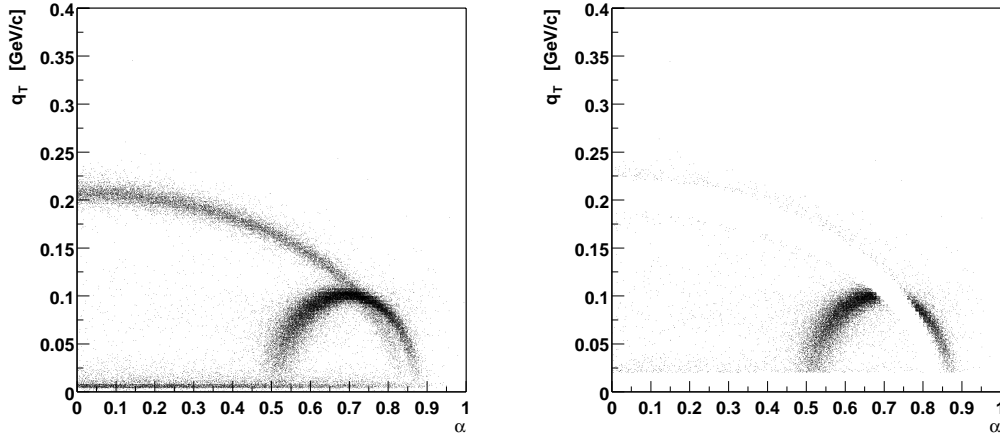


Figure 5.5: Podolanski-Armenteros plot: q_T versus α , before (left) and after (right) the cut on $M(\pi^+, \pi^-)$ and the cut on q_T (in order to remove γ conversion background) have been applied.

and Pb2000 periods the influence of the addition of the micro-strip lever arm on the results will be given.

5.2 Final selection results

5.2.1 The Pb-Pb data at 158 A GeV/ c taken in 1998.

The Pb1998 data are used for the analysis of the inverse slopes and yields (chapter 7) and the transverse polarization (chapter 8). For the analysis three types of V^0 decays were studied: the decays form the Λ , $\bar{\Lambda}$ and K_S^0 particles. The final particle samples used were found by applying strict selection criteria on the kinematical characteristics of a V^0 which have been described in the previous section. These cuts aim to have a pure sample and not to have a high efficiency and were taken to be the same as the cuts used for the determination of the inverse slopes and yields used for the weighting analysis [60]. In table 5.1 an overview of the selection criteria is given for the Λ and $\bar{\Lambda}$.

The variable x is the position of the decay vertex in the direction parallel to the beam. This position is given with respect to the center of the magnet, where the first detector of the telescope is positioned. The target has the position coordinates: $x = -61.2$ cm; $y = 0.0$ cm; $z = -17.5$ cm. The cut set on the position of the decay vertex requires that the accepted V^0 candidates have to decay at least 31 cm downstream from the target but before the telescope. In the left Podalanski-Armenteros plot of figure 5.5 background at low q_T can be seen. This is due to the γ conversion process ($\gamma \rightarrow e^+e^-$) [59] and in order to remove this contamination a cut of $q_T > 0.02$ GeV/ c has been set.

For the V^0 selection of the 1998 data, the *run-by-run vertex position* has been used to calculate

Table 5.1: Selection criteria for the Λ , $\bar{\Lambda}$ for the Pb1998 data.

Cut	$\Lambda/\bar{\Lambda}$
Secondary vertex	$-30. \text{ cm} < x < 0.5 \text{ cm}$
q_T	$0.02 \text{ GeV}/c < q_T < 0.4 \text{ GeV}/c$
Closest approach	$\Delta < 0.03 \text{ cm}$
Beam position	$\left(\frac{b_y}{2.5\sigma_y}\right)^2 + \left(\frac{b_z}{3.0\sigma_z}\right)^2 < 1$
Podalanski-Armenteros	$0.45 < \alpha (\Lambda) \text{ OR } 0.45 > \alpha (\bar{\Lambda})$
K_S^0 mass cut	$34 \text{ MeV}/c^2 < M(\pi^+, \pi^-) - m_{K_S^0} \text{ OR}$ $26 \text{ MeV}/c^2 < m_{K_S^0} - M(\pi^+, \pi^-)$
Transverse internal decay angle	$ \phi > 0.157 \text{ rad}$
Λ mass cut	$ M(p, \pi^-) - m_\Lambda < 10. \text{ MeV}/c^2 (\Lambda)$

Table 5.2: Selection criteria for K_S^0 for the Pb1998 data.

Cut	K_S^0
Secondary vertex	$-42. \text{ cm} < x < 0.5 \text{ cm}$
q_T	$0.125 \text{ GeV}/c < q_T < 0.6 \text{ GeV}/c$
Closest approach (cm)	$\Delta < 0.035$
Beam position	$\left(\frac{b_y}{2.5\sigma_y}\right)^2 + \left(\frac{b_z}{2.5\sigma_z}\right)^2 < 1$
Podalanski-Armenteros	-
K_S^0 mass cut	$20.6 \text{ MeV}/c^2 > M(\pi^+, \pi^-) - m_{K_S^0} \text{ AND}$ $16.6 \text{ MeV}/c^2 > m_{K_S^0} - M(\pi^+, \pi^-)$
Transverse internal decay angle	$ \phi > 0.157 \text{ rad}$

b_y and b_z . The spread of the beam impact, σ_y and σ_z , determined as described in section 5.1.1, is then used to define an elliptical cut. Because of the fact that the K_S^0 invariant mass distribution is not symmetrical, an assymetrical cut has been defined: the upper limit is put at $34 \text{ MeV}/c^2$ and the lower at $26 \text{ MeV}/c^2$ with respect to the PDG mass. The mass cut set for the selection of the Λ and $\bar{\Lambda}$ are set to about 2.5σ of their invariant mass distribution. The cut set on the internal decay angle ϕ is motivated by the fact that the combinatorial background formed from random combinations with primary tracks from the target can be found mostly at very small angle of ϕ .

This is due to the following reason: the geometrical acceptance for V^0 decays is largest in the plane around $\phi = 0$ (for a plot of the ϕ -distribution see figure 6.4). This is because the magnetic field is perpendicular to the (X', Y') plane (for a definition of the coordinates see figure 5.2) and due to the fact that the tracks are pointed towards each other. In the (X', Z') plane this effect is less pronounced and tracks have a larger probability to escape the telescope. In addition also primary tracks from the target also have a large probability to be contained in the (X', Y') direction. This increases the probability to make random combinations and to have a value of a closest approach which is within the selection cut. By applying a cut for a minimal value of ϕ almost all background can be removed [60].

The selection cuts for the K_S^0 are also taken from [60] (see table 5.2), except for the selection cut on the invariant mass and the cut on q_T . In order to remove the background of Λ and $\bar{\Lambda}$ particles a cut on the value of q_T was set: $0.125 < q_T$. This cut will influence the K_S^0 invariant mass distribution in the tails, but since the invariant mass distribution is not the subject of the investigations presented here this bias is tolerable. Instead of the cut of 2σ on the value of the invariant mass applied in [60], which seemed to be too small, it was chosen to have the cut at 2.5σ . Finally because the K_S^0 has a shorter decay length than the Λ the secondary decay vertex

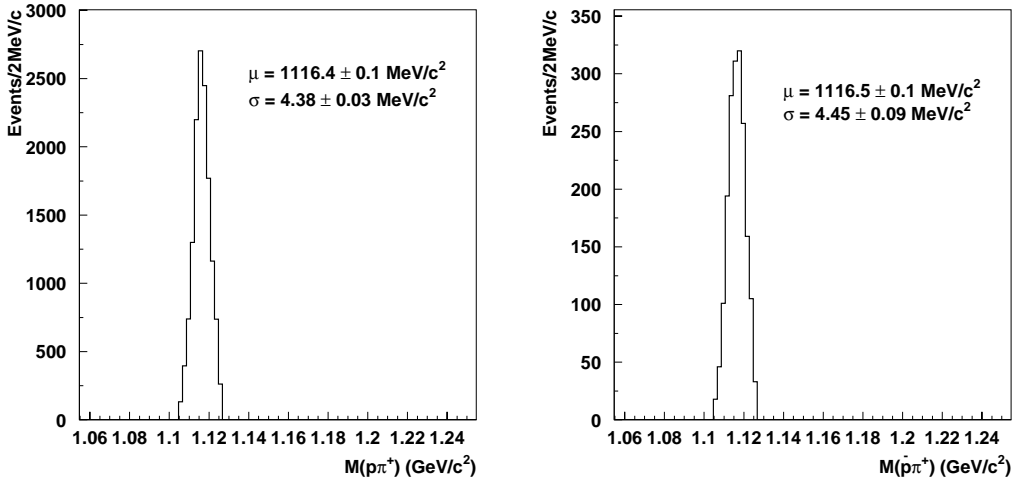


Figure 5.6: The invariant mass distributions for the final selection of particle samples for the Λ (left) and the $\bar{\Lambda}$ (right).

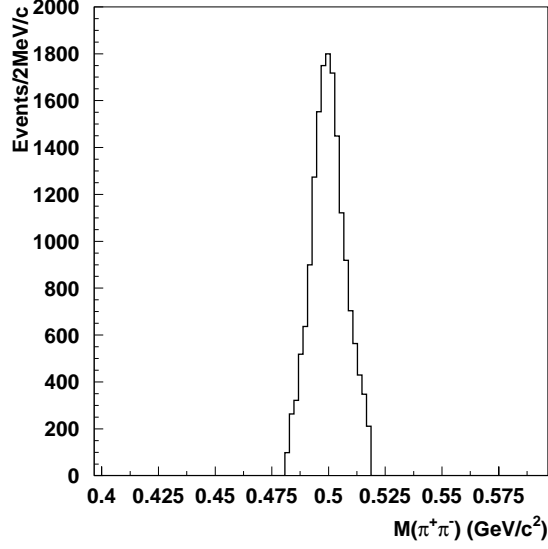


Figure 5.7: The invariant mass distribution for the final selection of the particle sample of the K_S^0 .

is allowed to be closer to the target. The other cuts resemble the cuts for the Λ and $\bar{\Lambda}$. The final selected particle samples are shown in figures 5.6 and 5.7. The results of the Gaussian fit of the invariant mass distributions are listed in table 5.3. It can be seen that the mean values of the invariant mass distributions are shifted with respect to the PDG values. This shift is the most pronounced for the K_S^0 mesons. The acceptance of these particles in y and p_T is depicted in figure 5.8, where only the Λ and K_S^0 acceptance window is shown. Due to the small acceptance the NA57 experiment measures in a banana-shape acceptance window.

Table 5.3: Results of the Gaussian fit of the invariant mass distributions for the Pb1998 data. Also the PDG values for the mass are given.

Particle	μ (MeV/c ²)	PDG value (MeV/c ²)	σ (MeV/c ²)
Λ	1116.4 ± 0.1	1115.7	4.33 ± 0.03
$\bar{\Lambda}$	1116.5 ± 0.1	1115.7	4.45 ± 0.09
K_S^0	500.0 ± 0.1	497.6	8.01 ± 0.07

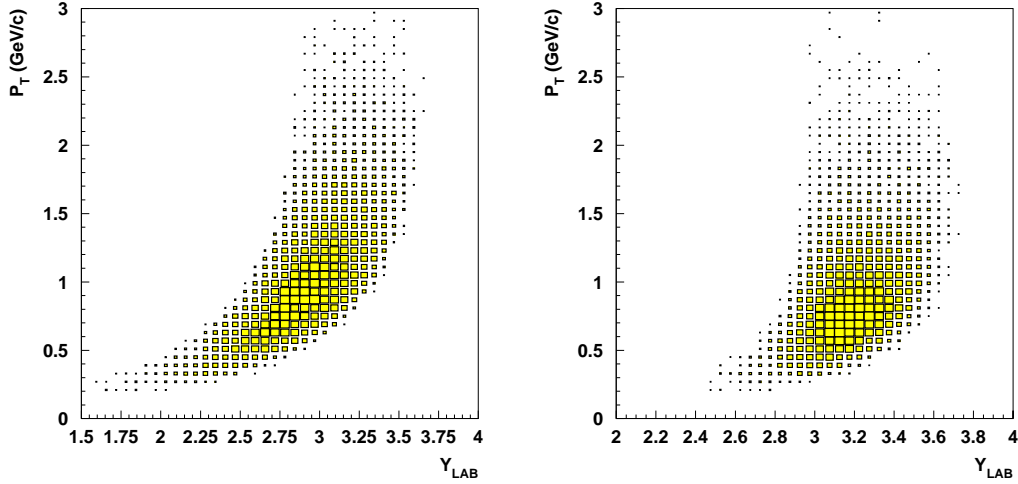


Figure 5.8: The acceptance window in y and p_T for the Λ s and K_S^0 .

5.2.2 The Pb-Pb data at 40 A GeV/ c taken in 1999.

In this section the results are given of the lambda reconstruction for the Pb1999 period with the micro-strips included in the lever arm compared to that without the use of the lever arm. First the selection criteria are defined after which the effect of the implementation of the micro-strip lever arm is investigated.

Selection cuts

The cuts applied for the 1999 (see table 5.4) differ from the 1998 case because the experimental setup was not the same. Also the analysis has not yet advanced enough to put tight cuts on the beam impact position and the particle masses. Note that the cut on the beam impact position is taken to be the V^0 vertex position and the impact cut is just rectangular. With these cuts the particle samples have been determined. In the next sections the resultant invariant mass distributions will be given for both the inclusion of the micro-strip lever arm and the case no lever arm is used in the analysis. First the results of simulations will be shown, after which the comparison with the data will be made.

Simulations study

In order to investigate the effect on the resolution of the invariant mass spectra GEANT simulations were run. The simulated particles are all in the acceptance of the lever arm, i.e. at least one track of the decay products is detected in the lever arm. Furthermore the background, the efficiency

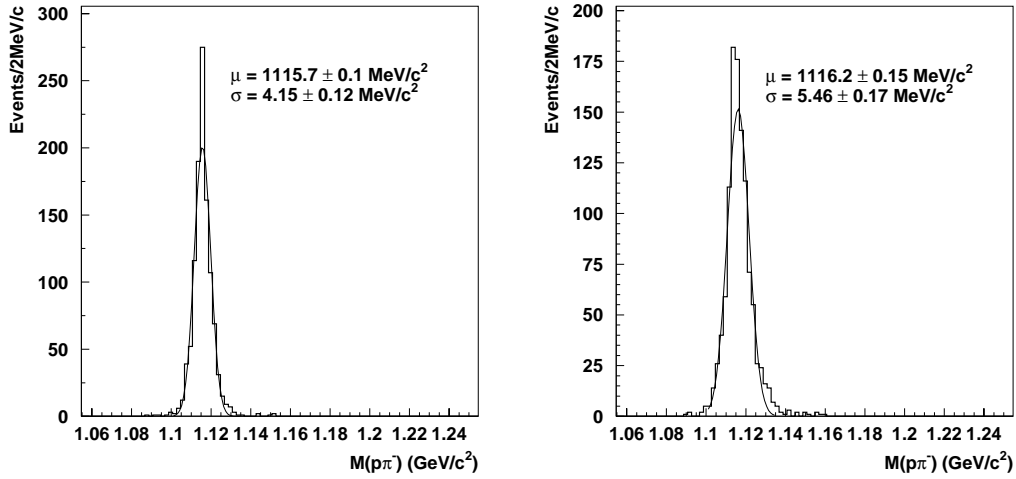


Figure 5.9: Gaussian fit of the invariant mass distribution of the Λ for simulations in the Pb-Pb 40 AGeV/c setup with the use of the micro-strips lever arm (left) and without (right).

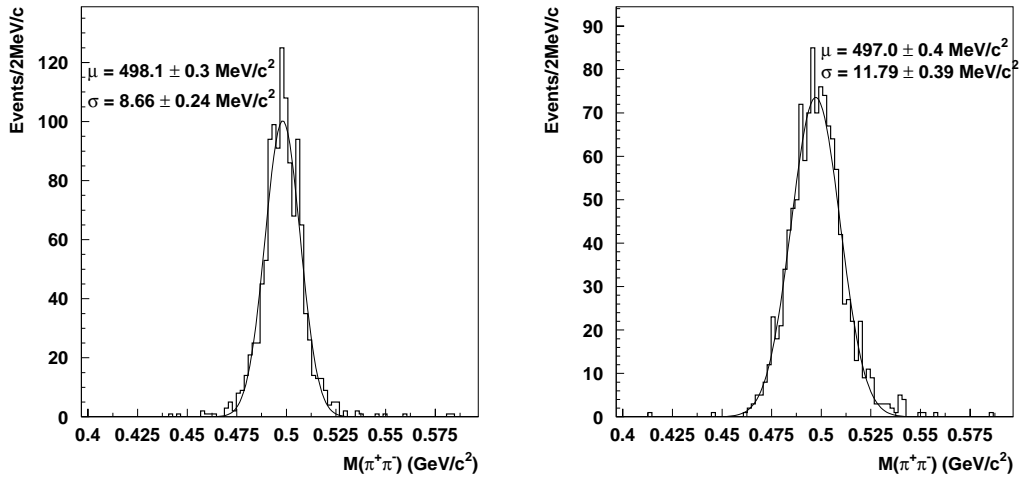


Figure 5.10: Gaussian fit of the invariant mass distribution of the K_S^0 for simulations in the Pb-Pb 40 AGeV/c setup with the use of the micro-strips lever arm (left) and without (right).

Table 5.4: Selection criteria for the Λ , $\bar{\Lambda}$ and K_S^0 for the Pb1999 data.

Cut	$\Lambda/\bar{\Lambda}$	K_S^0
Secondary vertex	$-35. \text{ cm} < x < -20. \text{ cm}$	$-45. \text{ cm} < x < -20. \text{ cm}$
q_T	$0.02 \text{ GeV}/c < q_T < 0.4 \text{ GeV}/c$	$0.06 \text{ GeV}/c < q_T < 0.4 \text{ GeV}/c$
Closest approach	$\Delta < 0.03 \text{ cm}$	$\Delta < 0.03 \text{ cm}$
Y beam position	$ b_y < 0.12 \text{ cm}$	$ b_y < 0.12 \text{ cm}$
Z beam position	$ b_z < 0.12 \text{ cm}$	$ b_z < 0.3 \text{ cm}$
Pod.-Arm.	$0.45 < \alpha (\Lambda) \text{ OR } -0.45 > \alpha (\bar{\Lambda})$	$-0.45 < \alpha < 0.45$
K_S^0 mass cut	$ M(\pi^+, \pi^-) - m_{K^0} > 30. \text{ MeV}/c^2$	$ M(\pi^+, \pi^-) - m_{K^0} < 30. \text{ MeV}/c^2$
Transverse internal decay angle	$ \phi > 0.1 \text{ rad}$	$ \phi > 0.1 \text{ rad}$
Λ mass cut	$ M(p, \pi^-) - m_\Lambda < 17. \text{ MeV}/c^2$	$ M(p, \pi^-) - m_\Lambda > 17. \text{ MeV}/c^2$
Longitudinal internal decay angle	$ \cos \theta_\Lambda^* < 0.9$	$ \cos \theta_{K^0}^* < 0.75$

of the detectors and noise are simulated in accordance with the experimental conditions. This information and the setup definition was taken from the HEPDB database. For Pb1999 5000 Λ 's and K_S^0 were simulated. After the reconstruction in ORHION and the selection in ANALYZE the resulting distributions were fitted. The invariant mass distributions of the particles analysed with the micro-strips and without are plotted in figures 5.9 and 5.10. They were fitted with a

Table 5.5: Results of the Gaussian fit of the invariant mass distributions with the use of the micro-strip lever arm and without for Pb1999 simulations.

Particle	Lever Arm	$\mu(\text{MeV}/c^2)$	$\sigma(\text{MeV}/c^2)$
Λ	On	1115.7 ± 0.1	4.15 ± 0.12
Λ	Off	1116.2 ± 0.1	5.46 ± 0.17
K_S^0	On	498.1 ± 0.3	8.66 ± 0.24
K_S^0	Off	497.0 ± 0.4	11.79 ± 0.39

Gaussian, the results of which are listed in table 5.5. An improvement from 5.5 to 4.1 MeV/c² for the resolution of the Λ distribution can be found and an improvement of 11.8 to 8.7 MeV/c² for the K_S^0 . This amounts to an improvement of 25% of the resolution.

Data study

In the reconstruction software for the analysis of the pb1999 data, the micro-strips have been added. However, since the reconstruction of all data was started before the part adapted for the micro-strips was finished, only a small sample of data was analyzed with the new software. This same sample was analyzed without the use of the lever arm. In this way the track momentum improvement with the inclusion of the micro-strip lever arm could be looked at.

A sample of 11 runs around the reference run 11000 was chosen, an equivalent to 2.5 million events. The first selection of V^0 candidates of the ORHION output DST was analyzed with the selection cuts listed in table 5.4 for both the lever arm included and excluded. The invariant mass plots of the Λ and K_S^0 are plotted in figures 5.11- 5.12. For the Λ insufficient statistics was available to do the same analysis.

In the plots on the left of these figures first the invariant mass distribution of the selected V^0 candidates are shown for the reconstruction with only the compact telescope (hatched histogram) and with the use of the micro-strip lever arm (white histogram). The same distributions are given in the right hand plots, but now the addition of a lever arm hit to at least one track of the V^0 has been required.

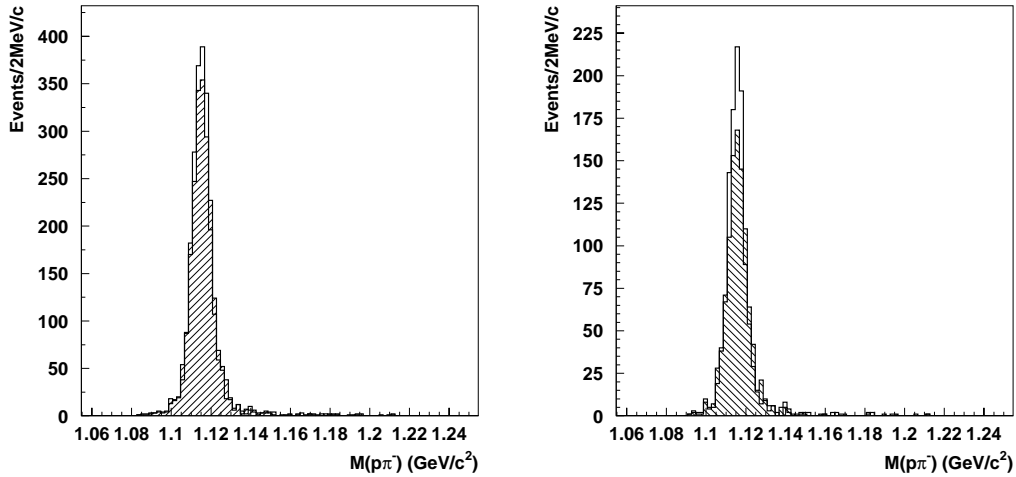


Figure 5.11: Invariant mass distribution of the Λ for the Pb-Pb 40 AGeV/c data with the use of the micro-strips lever arm (white) and without (shaded) on the left. The same distribution is plotted to the right, but now at least one of the decay tracks of the Λ is required to have a hit attached in one of the lever arm detectors.

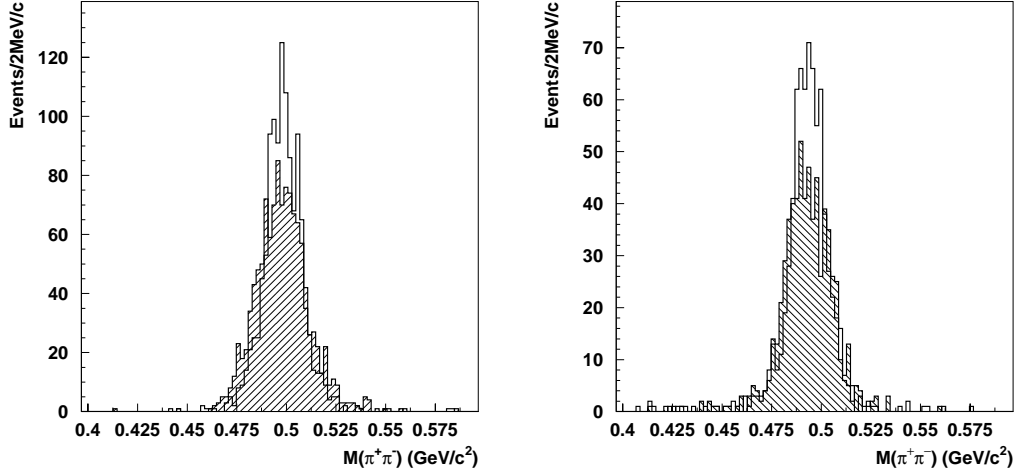


Figure 5.12: Invariant mass distribution of the K_S^0 for the Pb-Pb 40 AGeV/c data with the use of the micro-strips lever arm (white) and without (hatched) on the left. The same distribution is plotted to the right, but now at least one of the decay tracks of the K_S^0 is required to have a hit attached in the one of the lever arm detectors.

The improvement of the width of the distribution can already be seen in the comparison for all selected V^0 candidates, but the requirement of one lever arm track gives a good indication of the lever arm effect. Considering the fact that the simulated data also have one track in the lever arm, these invariant mass distributions can be compared. In table 5.6 the resolution of the three particle types is given when at least one hit has been added in the lever arm. For the $\bar{\Lambda}$ signal not enough statistics were available to get a good estimation, but for the Λ and K_S^0 the improvement of the signal is about 15%. This is less than for the simulations. This is due to a worse resolution in the simulations for the signal analysed with the lever arm off. The signal retrieved with the micro-strip lever arm included has the same absolute value. The percentage of particles which have at least one hit in the lever arm is 49% for the Λ and 68% for the K_S^0 so the improvement for the total sample is less pronounced. The total sample resolutions are listed in table 5.7.

5.2.3 The Pb-Pb data at 158 AGeV/c taken in 2000.

For the Pb2000 data the same analysis was done as for the Pb1999 sample, explained in the previous section. Since the beam energy is higher, the number of particles reaching the lever arm should be greater. It is expected that the lever arm improvement of the invariant mass resolution should be more pronounced in the total sample.

Table 5.6: Results of the Gaussian fit of the invariant mass distributions with the use of the micro-strip lever arm and without for Pb1999 data. The particles selected have at least one track inside the lever arm.

Particle	Lever Arm	μ (MeV/c ²)	σ (MeV/c ²)
Λ	On	1115.3 ± 0.1	4.23 ± 0.12
Λ	Off	1115.7 ± 0.1	5.00 ± 0.14
K_S^0	On	493.9 ± 0.3	8.41 ± 0.31
K_S^0	Off	493.1 ± 0.4	10.22 ± 0.35

Table 5.7: Results of the Gaussian fit of the invariant mass distributions with the use of the micro-strip lever arm and without for Pb1999 data. The whole selected sample is considered. The percentage of particles which have at least one hit in the lever arm is given for each particle type.

Particle	Lever Arm	μ (MeV/c ²)	σ (MeV/c ²)	Percentage (%)
Λ	On	1115.2 ± 0.1	4.59 ± 0.09	49
Λ	Off	1115.4 ± 0.1	5.08 ± 0.10	
K_S^0	On	493.9 ± 0.3	8.84 ± 0.25	68
K_S^0	Off	492.9 ± 0.2	10.10 ± 0.28	

Table 5.8: Selection criteria for the Λ , $\bar{\Lambda}$ and K_S^0 for the Pb2000 data.

Cut	$\Lambda/\bar{\Lambda}$	K_S^0
Secondary vertex	$-32. \text{ cm} < x < 2. \text{ cm}$	$-35. \text{ cm} < x < -20. \text{ cm}$
q_T	$0.02 \text{ GeV}/c < q_T < 0.4 \text{ GeV}/c$	$0.06 \text{ GeV}/c < q_T < 0.4 \text{ GeV}/c$
Closest approach	$\Delta < 0.025 \text{ cm}$	$\Delta < 0.02 \text{ cm}$
Y beam position	$ b_y < 0.12 \text{ cm}$	$ b_y < 0.12 \text{ cm}$
Z beam position	$ b_z < 0.1 \text{ cm}$	$ b_z < 0.1 \text{ cm}$
Pod.-Arm.	$0.45 < \alpha (\Lambda) \text{ OR } -0.45 > \alpha (\bar{\Lambda})$	$-0.45 < \alpha < 0.45$
K_S^0 mass cut	$ M(\pi^+, \pi^-) - m_{K^0} > 30. \text{ MeV}/c^2$	$ M(\pi^+, \pi^-) - m_{K^0} < 30. \text{ MeV}/c^2$
Transverse internal decay angle	$ \phi > 0.1 \text{ rad}$	$ \phi > 0.1 \text{ rad}$
Λ mass cut	$ M(p, \pi^-) - m_\Lambda < 17. \text{ MeV}/c^2$	$ M(p, \pi^-) - m_\Lambda > 17. \text{ MeV}/c^2$
Longitudinal internal decay angle	$ \cos \theta_\Lambda^* < 0.9$	$ \cos \theta_{K^0}^* < 0.75$

Table 5.9: Results of the Gaussian fit of the invariant mass distributions with the use of the micro-strip lever arm and without for Pb2000 simulations.

Particle	Lever Arm	μ (MeV/ c^2)	σ (MeV/ c^2)
Λ	On	1116.0 ± 0.1	3.91 ± 0.12
Λ	Off	1116.3 ± 0.1	5.19 ± 0.14

Selection cuts

Although the position of the telescope was the same for the Pb1998 as for the Pb2000 run, the silicon telescope consisted of 2 more pixel planes. Furthermore the lever arm consisted of 5 planes, 3 double-sided and two single-sided. For the final analysis only the 3 double-side planes were used, as motivated in section 4.2.4. Also for this sample the analysis was not sufficiently advanced to have a precise primary vertex position. Therefore for this sample the V^0 vertex position was used and a rectangular cut was applied. The list of selection cuts for the Pb2000 data is given in table 5.8.

Simulations

For the Pb2000 data only 5000 Λ particles were simulated and reconstructed. The results of the reconstruction are given in table 5.9. In this case the invariant mass resolution improves from 5.19 to 3.9 MeV/ c^2 .

Data

The data sample with at least one hit in the lever arm consists of one run: the reference run 13250. The unbiased sample consists of 10 runs which were taken around the reference run. The result of the simulations can again be compared with the Λ s from the data with at least one hit in the

Table 5.10: Results of the Gaussian fit of the invariant mass distributions with the use of the micro-strip lever arm and without for Pb2000 data. The particles selected have at least one track inside the lever arm.

Particle	Lever Arm	μ (MeV/ c^2)	σ (MeV/ c^2)
Λ	On	1116.1 ± 0.2	4.22 ± 0.23
Λ	Off	1116.3 ± 0.3	5.05 ± 0.27
K_S^0	On	494.3 ± 0.5	8.09 ± 0.51
K_S^0	Off	494.2 ± 0.6	9.19 ± 0.55

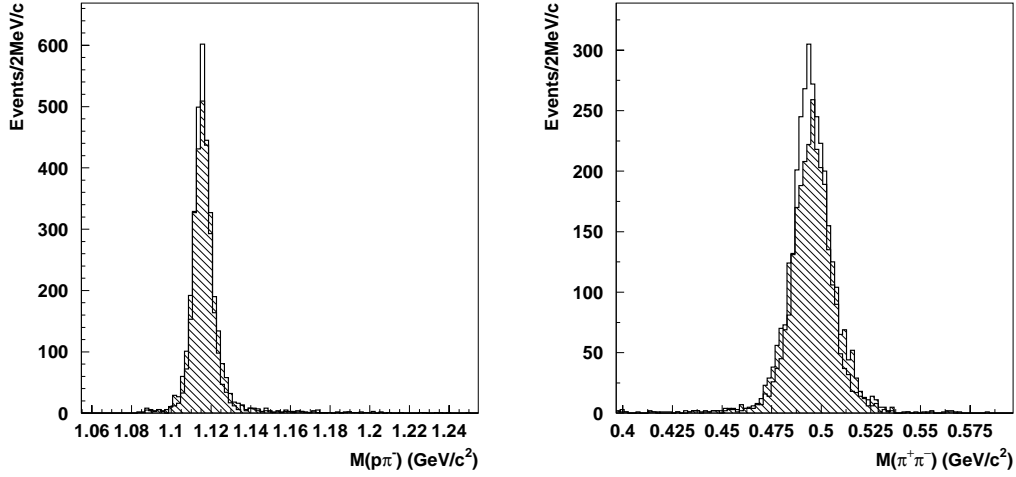


Figure 5.13: Invariant mass distribution of the unbiased Λ (left) and K_S^0 (right) sample for the Pb-Pb 158 A GeV/c data taken in 2000. The distribution of the data taken with the the micro-strips lever is rendered by a white histogram, the distribution of the data taken without the lever arm by the hatched histogram.

Table 5.11: Results of the Gaussian fit of the invariant mass distributions with the use of the micro-strip lever arm and without for Pb2000 data. The whole selected sample is considered. The percentage of particles which have at least one hit in the lever arm is given for each particle type.

Particle	Lever Arm	μ (MeV/ c^2)	σ (MeV/ c^2)	Percentage (%)
Λ	On	1115.8 ± 0.1	4.24 ± 0.08	88.5
Λ	Off	1116.0 ± 0.1	5.21 ± 0.11	
K_S^0	On	495.0 ± 0.1	8.40 ± 0.14	93.9
K_S^0	Off	495.1 ± 0.1	9.81 ± 0.14	

lever arm. The results of the fit of the invariant mass distributions are listed in table 5.10. The improvement of the Λ signal is from 5.05 to 4.22 which is compatible with the result from the simulations. The same 15% improvement can be seen for the K_S^0 while for the $\bar{\Lambda}$ the statistics was too low.

The beam energy of the Pb2000 run was higher than the energy of the Pb1999 run, which implies that a larger percentage of particles reach the lever arm. For the Λ s this percentage amounts to 89% where for the K_S^0 it even reaches 94%. The improvement of the resolution of the unbiased sample is expected to be dominated by the lever arm sample. This is shown in table 5.11 where the improvement of the unbiased sample due to the lever arm influence is given. The improvement of the invariant mass resolution of the Λ amounts to 20% and for the K_S^0 to about 15%. The influence on the invariant mass spectra due to the inclusion of the micro-strip lever arm for the Λ and K_S^0 can be seen in figure 5.13.

These results imply that the micro-strip lever arm has functioned well during the Pb2000 period and that it has been able to improve the invariant mass distributions. This allows tighter mass cuts to be set and reduces the amount of background. Furthermore the analysis performed in the chapter on the track reconstruction shows that the micro-strip detectors employed in the lever arm have reached high reconstruction efficiencies (94-96%). In addition a good position resolution in the bending direction was achieved, which ranged from 20 to 28 μm . Since these detectors are prototypes for the ones which will be used in the ALICE inner tracker, the results presented here are an indication that the ALICE detectors will function well and they give confidence for the future.

6

Data Analysis

In the previous chapter the reconstruction of the measured particles has been discussed. Unfortunately the distribution of the measured particles is not a description of the real distribution of the particles coming out of the collision. The measured distributions of physical variables, like m_T -spectra or decay particle momenta spectra, are distorted due to the imperfection of the detectors and analysis cuts. There are different effects to take into account:

- Limited acceptance: this implies that the probability to observe a given event is less than 1. In NA57 this limited acceptance is mainly due to the small size of the detector. Furthermore inefficient regions in the silicon planes contribute to the loss of events.
- Limited resolution: this is due to the fact that a quantity x in a given event cannot be determined exactly, but only can be measured with a certain measurement error. In NA57 for example the resolution is influenced by the resolution of the silicon detectors and the precision of the magnetic field determination.

There are different methods to correct for these effects. In the NA57 experiment usually the method of *particle-weighting* is used to reconstruct the m_T -spectra and to determine the raw yields. A short description of this method is given in section 6.1. This procedure is relatively simple and straightforward, but has the limitation that it is very CPU-time consuming. Therefore only a small sample of statistics can be used. Another, more complicated, method, which enables the use of a large sample of statistics is the *deconvolution* method, which has been proposed by Blobel [14]. This method performs an unfolding of the data by making use of the information on the transformation of MC events due to the experimental setup. Besides the possibility of handling larger data samples it also takes into account the smearing between bins of a distribution while the weighting method only corrects for the loss of events in one bin. In section 6.2 the principle of this method will be explained and practical guidelines are provided for the use on the NA57 data. In section 6.3 the determination of the centrality of the collision will be discussed.

Finally in section 6.4, the generation of the Monte Carlo information used as input for the deconvolution method will be described.

6.1 Weighting procedure

The weighting procedure intends to determine for each measured particle a detection probability. The inverse of this probability is called a *weight*. By summing the weights of all measured particles the original distribution can be recovered.

The weights are obtained by performing a sequence of steps. For each measured particle a number of particles with the same p_T and rapidity are generated in GEANT simulations, which comprise of a complete and precise description of the experimental setup. This simulation includes the geometrical description of the detectors and their response to particles. By incorporating the detector efficiencies, determined for the relevant run period, a realistic simulation of the efficiencies is obtained. The particles which fulfill the constraints set in the data reconstruction (e.g. 7 hits out of 9 planes for the 1998 data) are selected for further processing and in case of the Λ and $\bar{\Lambda}$ for each original particle a total of 2500 simulated and accepted particles are used. The total number of generated particles N_{gen} (so also the ones who gave not a good enough signal in the detector) is saved.

The selected particles are then embedded in the data, providing events with the expected background in the raw data format. These events are subsequently processed in the same way as the data which means that ORHION and ANALYZE are run on them. The number of particles recovered after this procedure is used to determine the weight of the particle:

$$W(y, p_T) = \frac{2\pi}{\Delta\phi} \times \frac{1}{P} = \frac{2\pi}{\Delta\phi} \times \frac{N_{\text{gen}}}{N_{\text{ana}}}, \quad (6.1)$$

where the multiplicative factor $\frac{2\pi}{\Delta\phi}$ indicates that particles were only generated in a region where there was some chance of detection. N_{ana} is the number of generated particles retrieved by ANALYZE. The weights found in this way for the Λ are in the range from 455 to 1×10^6 , with an average of 1891 (see [39]). The largest weights are found for the events near the edge of the acceptance region.

6.2 Deconvolution

When considering a set x of measured physical variables, they can be regarded as a random sample drawn from a distribution $f(x)$. Data analysis intends to reconstruct this original distribution from the measured set x . Due to the limited detector acceptance and resolution mentioned before, this quantity x and the distribution $f(x)$ cannot be measured directly. Instead a variable y and its distribution $g(y)$ are measured. The distributions $f(x)$ and $g(y)$ are related by the convolution integral [14]:

$$g(y) = \int A(y, x) f(x) dx, \quad (6.2)$$

which is a so called Fredholm integral equation of the first kind. The kernel $A(y, x)$ describes the response of the detector and also encompasses the transformation of x to y . The measured distribution $g(y)$ usually is represented in a histogram g with m bins. Correspondingly the true distribution f can be represented by a histogram with n bins. The discrete approximation of 6.2 can then be expressed in the matrix equation:

$$g = Af, \quad (6.3)$$

where $A(y, x)$ is represented by the m -by- n matrix A . The matrix element A_{ij} then yields the probability to measure an event from true bin f_j in bin g_i .

In order to solve this equation the response matrix A has to be well known. Precise Monte Carlo events can provide information on the detector response: events, generated according to the distribution f_{MC} , will yield the measurement g_{MC} . Out of f_{MC} and g_{MC} the response matrix can be calculated. A detailed description of the simulations and the input for the deconvolution calculation will be given in the next chapter.

In case the limited acceptance is the dominant effect, the solution of equation 6.3 is easy. In this case all elements A_{ij} are zero for $i \neq j$ (taken that $n = m$) and only the elements A_{ii} are relevant. The correction for the limited acceptance can then be calculated by multiplying the measured bin contents g_i by a correction factor defined by the Monte Carlo acceptance probability:

$$f_i = g_i \left(\frac{f_{iMC}}{g_{iMC}} \right). \quad (6.4)$$

This method is called the *factor method* and gives no difficulties, except for a rapid change in the acceptance probability in a few bins. This method corresponds to the weighting method described above in case one takes each weighted particle to correspond to one diagonal element A_{ii} .

In the case a correction is needed for the limited resolution, the matrix elements A_{ij} are not equal to zero and must be taken into account. When the matrix A is square, equation 6.3 has the straightforward solution:

$$f = A^{-1}g, \quad (6.5)$$

and the variance matrix of the solution can be calculated by error propagation:

$$V(f) = (A^{-1})V(g)(A^{-1})^T, \quad (6.6)$$

where $V(g)$ is the variance matrix of the data (for n data points):

$$V(g) = \begin{pmatrix} g_1 & 0 & 0 & \dots & 0 \\ 0 & g_2 & 0 & \dots & 0 \\ 0 & 0 & g_3 & \dots & 0 \\ \vdots & \vdots & \vdots & \ddots & \vdots \\ 0 & 0 & \dots & 0 & g_n \end{pmatrix}.$$

This method is called the *inversion method* and seems to be easy to handle. Unfortunately the result can be very disappointing, because it tends to show an oscillating behavior. This is due to the fact that the covariance matrix of the solution is not diagonal and shows large negative correlations. These correlations make that the statistical fluctuations in g generate oscillations in f . In the next sections this will be explained in more detail and a tool will be described which can prevent the oscillations in the final solution: regularization.

When looking at the case when $m \neq n$, A is not invertible and another method has to be chosen to get the solution. This can be obtained by using the least squares method in the matrix notation:

$$\chi^2 = (g - Af)^T W (g - Af), \quad (6.7)$$

where we define the weight matrix $W = V^{-1}(g)$. In order to transform the distributions $f(x)$ and $g(y)$ into vectors a discretization will be done. This will be shown in the next section.

6.2.1 Discretization

The first step in the understanding of the problems is by a discretization of the function $f(x)$. This discretization can be achieved by first representing the function $f(x)$ with a finite set of coefficients a_1, a_2, \dots, a_m :

$$f(x) = \sum_{j=1}^m a_j p_j(x), \quad (6.8)$$

where the basis functions $p_j(x)$ will be specified later. With this parameterization the integral

in 6.2 can be calculated:

$$\int_a^b A(y, x)f(x)dx = \sum_{j=1}^m a_j \left[\int_a^b A(y, x)p_j(x)dx \right] = \sum_{j=1}^m a_j A_j(y) \quad (6.9)$$

$$\text{with } A_j(y) = \int_a^b A(y, x)p_j(x)dx.$$

So this yields the expected distribution:

$$g(y) = \sum_{j=1}^m a_j A_j(y), \quad (6.10)$$

which is expressed as a superposition of functions $A_j(y)$, each representing one term $p_j(x)$ in the representation 6.8.

The second step is to represent all y -dependent functions in 6.10 by histograms, assuming a certain set of bin-limits y_0, y_1, \dots, y_n :

$$g_i = \int_{y_{i-1}}^{y_i} g(y)dy, \quad A_{ij} = \int_{y_{i-1}}^{y_i} A_j(y)dy, \quad (6.11)$$

which gives the equivalent matrix representation of 6.3

$$g = Aa, \quad (6.12)$$

with g again a n -vector and A a n -by- m matrix of elements A_{ij} . These elements can now be determined from the Monte Carlo events. Each MC event with true value x , is added to histogram $A_j(y)$ with a weight proportional to $p_j(x)$. In order to have a proper normalization and to avoid negative weights the conditions:

$$p_j(x) \geq 0, \quad \sum_{j=1}^m p_j(x) \equiv 1, \quad (6.13)$$

have to be met. Furthermore an overall weight for the MC-events has to be defined such that the resulting distribution $f(x)$ is correctly normalized. In the following the distribution g and coefficients a_j are Monte Carlo variables, while data variables will be denoted by adding a hat.

6.2.2 Unfolding without regularization

Now that the deconvolution equation is expressed in coefficients a , the coefficients for the solution \hat{a} can be found by a χ^2 fit to the the measured distribution \hat{g} (given in the matrix notation):

$$S(\hat{a}) = \chi^2 = (\hat{g} - A\hat{a})^T W (\hat{g} - A\hat{a}) \quad (6.14)$$

$$= \hat{g}\hat{g} - 2\hat{a}^T A^T W \hat{g} + \hat{a}^T A^T W A \hat{a}. \quad (6.15)$$

Minimizing χ^2 by setting the condition $\nabla S = 0$ will then yield the solution:

$$-A^T W \hat{g} + A^T W A \hat{a} = 0. \quad (6.16)$$

This can be written as:

$$\hat{a} = H^{-1}h, \quad (6.17)$$

where the negative gradient h and the Hessian H are defined by the elements:

$$h_j = \frac{\partial S}{\partial a_j}, \quad H_{jk} = \frac{\partial^2 S}{\partial a_j \partial a_k}, \quad (6.18)$$

The full solution can be expressed in the following form

$$\hat{a} = H^{-1}h = (A^T W A)^{-1} A^T W \hat{g}, \quad (6.19)$$

and this yields the covariance matrix as given by error propagation

$$V(\hat{a}) = (A^T W A)^{-1} A^T W W A (A^T W A)^{-1} = (A^T W A)^{-1} = H^{-1}. \quad (6.20)$$

Since matrix H is symmetric it can be transformed to a diagonal matrix D :

$$D = U_1^T H U_1, \quad (6.21)$$

where the matrix U_1 is an orthogonal matrix with the property $U_1^T U_1 = U_1 U_1^T = \mathbf{1}$. The columns u_j are the eigenvectors corresponding to the (real) eigenvalues D_{jj} in its column. These eigenvalues may be arranged in decreasing order $D_{11} \geq D_{22} \geq \dots \geq D_{mm}$. Another vector \hat{a}_1 can now be constructed

$$\hat{a}_1 = D^{1/2} U_1^T \hat{a}, \quad (6.22)$$

which has the corresponding covariance matrix

$$V(a_1) = D^{-1/2} U_1^T V(a) U_1 D^{-1/2} = D^{-1/2} U_1^T H U_1 D^{-1/2} = \mathbf{1}. \quad (6.23)$$

The fact that the covariance matrix is the unity matrix implies that the components of \hat{a}_1 are uncorrelated and hence statistically independent. Their variance of 1 makes it easy to see which of these components are statistical significant. When we use a confidence level of 95% this will make all components i with $(\hat{a}_1)_i^2 \leq 3.85$ compatible with zero (when assuming that the coefficients $(\hat{a}_1)_i^2$ follow a χ^2 distribution). If all values $(\hat{a}_1)_i$ with $i > m_0$ are compatible with zero they are not statistical significant and they will provide no information for the result. Ironically they are the components which spoil the solution \hat{a} . This can be seen when formula 6.22 is rewritten and the solution vector \hat{a} is expressed as a linear combination of the eigenvectors:

$$\hat{a} = \sum_{j=1}^m \left(\frac{1}{D_{jj}} \right)^{\frac{1}{2}} (\hat{a}_1)_j u_j. \quad (6.24)$$

The smallest of the factors $\left(\frac{1}{D_{jj}} \right)^{\frac{1}{2}}$ are the ones which are connected to the insignificant components and because of their unit variance they get a large weight factor in the full solution. This will cause the full solution to have fluctuations. One way to prevent this is to use only the first m_0 amplitudes, but this also can introduce some fluctuations in the solution, known as 'Gibbs phenomenon' in the theory of Fourier analysis. A better way is to accomplish a smooth cut-off. This can be established by the concept of regularization.

6.2.3 Unfolding with regularization

The magnitude of the fluctuations mentioned in the last section can be measured by looking at the total curvature of the solution $f(x)$. This can be rendered quantitatively by:

$$r(a) = \int f''(x)^2 dx. \quad (6.25)$$

For a strongly fluctuating solution this value will have large values and can be an indication of the correction needed to remove the oscillations. To the expression for $S(a)$ then an extra term is added

$$R(\hat{a}) = S(\hat{a}) + \frac{1}{2}\tau r(\hat{a}), \quad (6.26)$$

where the factor $\frac{1}{2}$ is introduced for convenience later. The factor τ is called the regularization parameter.

An example for a good choice of base elements for parameterization of the function $f(x)$ are Quintic Splines. These are smooth and therefore their curvature is well defined. This has the advantage that $r(\hat{a})$ can be represented by the quadratic expression:

$$r(\hat{a}) = \hat{a}^T C \hat{a}, \quad (6.27)$$

where the matrix C is symmetric and semi positive-definite. Apart from some factor which can be absorbed in τ the matrix C is constant and has the form:

$$C = \begin{pmatrix} 2 & -3 & 0 & 1 & 0 & 0 & \dots \\ -3 & 8 & -6 & 0 & 1 & 0 & \\ 0 & -6 & 14 & -9 & 0 & 1 & \\ 1 & 0 & -9 & 16 & -9 & 0 & \\ 0 & 1 & 0 & -9 & 16 & -9 & \\ 0 & 0 & 1 & 0 & -9 & 16 & \\ \vdots & & & & & & \ddots \end{pmatrix}. \quad (6.28)$$

The equation to minimize then becomes:

$$S(a) = \hat{g}\hat{g} - \hat{a}^T h + \frac{1}{2}\hat{a}^T H \hat{a} + \frac{1}{2}\tau \hat{a}^T C \hat{a}, \quad (6.29)$$

which gives:

$$(H + \tau C)\hat{a} = h. \quad (6.30)$$

This can be treated the same way as for the unregularized solution. First the transformation $\hat{a} = U_1 D^{-1/2} \hat{a}_1$ will yield:

$$\hat{a}_1 + \tau D^{-1/2} U_1^T C U_1 D^{-1/2} \hat{a}_1 = D^{-1/2} U_1^T h. \quad (6.31)$$

where now the regularization term can be written as:

$$\tau \cdot \hat{a}_1^T C_1 \hat{a}_1, \quad (6.32)$$

with $C_1 = D^{-1/2}U_1^T C U_1 D^{-1/2}$. The matrix C_1 can again be diagonalized as $S = U_2^T C_1 U_2$, which gives the equation:

$$\hat{a}_1 + \tau U_2 S U_2^T \hat{a}_1 = D^{-1/2} U_1^T h. \quad (6.33)$$

Defining the rotation $\hat{a}' = U_2^T \hat{a}_1$ gives

$$\hat{a}' + \tau S \hat{a}' = U_2^T D^{-1/2} U_1^T h, \quad (6.34)$$

which can be rewritten to give the final solution \hat{a}' :

$$\begin{aligned} \hat{a}' &= \frac{1}{(I + \tau S)} U_2^T D^{-1/2} U_1^T h \\ &= \frac{1}{(I + \tau S)} U_2^T \bar{a} \\ &= \frac{1}{(I + \tau S)} \bar{a}'. \end{aligned} \quad (6.35)$$

The final result implies that the regularized solution is just the unregularized ($\tau = 0$) solution multiplied by a factor, which depends on the eigenvalues S_{jj} introduced by the regularization term. The coefficients \bar{a}' are the coefficients of the unregularized solution \bar{a} rotated by U_2^T . Because this matrix is orthogonal the covariance matrix $V(\bar{a}')$ is still the unit matrix. The original parameterization 6.8 can be expressed in the new coefficients:

$$f(x) = \sum_{j=1}^m \bar{a}'_j p'_j(x), \quad (6.36)$$

where the functions $p'_j(x)$ are linear combinations of the original basis functions $p_j(x)$ (in this case the quintic-spline functions $B_j(x)$). In this parameterization the curvature is given by

$$\int f''(x)^2 dx = \sum_{j=1}^m (\bar{a}'_j)^2 S_{jj}. \quad (6.37)$$

Because the eigenvalues of matrix S can be arranged in increasing order $D_{11} \leq D_{22} \leq \dots \leq S_{jj}$, the contribution to the curvature rises rapidly with increasing index j . If we rewrite 6.35 in the vector components

$$\hat{a}'_j = \frac{1}{(1 + \tau S_{jj})} \bar{a}'_j, \quad (6.38)$$

it becomes clear that the coefficients \bar{a}' are damped for the higher indices j . This means that the statistically insignificant coefficients which cause the oscillations in the final solution are given a very low weight. By this smooth cut-off the 'Gibbs Phenomenon' can be avoided and the number of independent contributions to the solution m_0 should be almost equal to the sum of all factors. When m_0 is specified, the regularization parameter can be calculated from:

$$m_0 = \sum_{j=1}^m \frac{1}{(1 + \tau S_{jj})}. \quad (6.39)$$

A lower limit for m_0 can be determined by looking at the statistical significance of the coefficients of the unregularized solution. Whenever the value of τ is determined the regularized solution can be calculated. Its covariance matrix then will be:

$$V(\hat{a}') = (I + \tau S_{jj})^{-2}. \quad (6.40)$$

The final result will be obtained by transforming the coefficients back to data points, representing average values for the unfolded $f(x)$ in small regions. Blobel proposes to define the limits of the data point regions by using the functions $p'_{m_0+1}(x)$. Since this function has m_0 zeros it seems optimal to define the data points around these zeros. In this way the contribution of the term $\hat{a}'_j p'_j(x)$, which is attenuated by a factor 1/2, is suppressed and the statistical precision and the resolution of x is taken into account. The limits of the data points are then taken to be the extrema of the function $p'_{m_0+1}(x)$.

Now that the concepts of deconvolution have been described, the next step in the analysis of the data is to develop the tools to define the response of the detector: the simulations. Since these have to be the best possible representation of the data it was decided to simulate particles in the same centrality classes, as have been defined in the analysis of the yields (see figure 1.3). Therefore first the definition of the centrality classes will be described.

6.3 Determination of the centrality

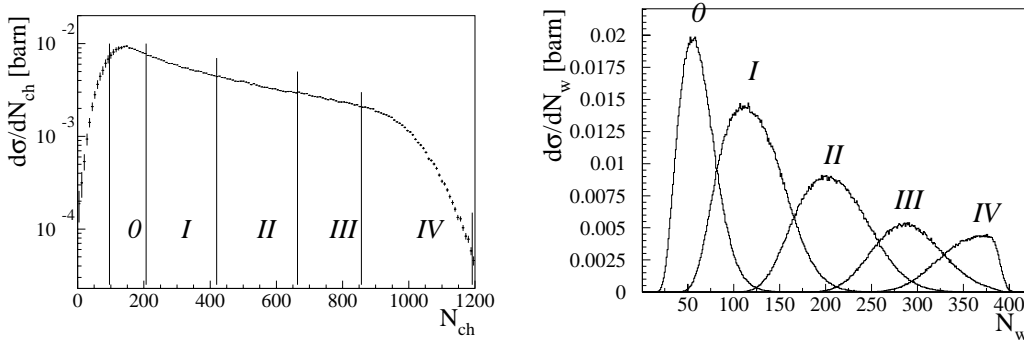


Figure 6.1: Distribution of the charged-particle multiplicity (left) and distribution of the number of wounded nucleons (right) for the five centrality bins of the NA57 experiment. The centrality bins range from peripheral (0) to central (IV).

The centrality of the nucleus-nucleus collisions can be determined by the MSD detectors (see 3.2.3). These measure the number of charged particles produced in the pseudo-rapidity region of $1.88 < \eta < 4.0$. By using Monte Carlo simulations corrections can be made for geometrical acceptance and detector inefficiencies. The corrected distribution of charged particles can be seen in the left plot of figure 6.1 [63]. The distribution shows a drop at lower multiplicities. This is due to the centrality trigger, which suppresses the low multiplicity events. In the figure also the division of the distribution into subsamples, which correspond to different centrality classes, is indicated. The

last four of these so called centrality bins (I to IV) are equivalent to the bins defined in WA97. Bin (0) is only measured by NA57. This bin does not extend to the lower limit of the distribution. This is because at these low multiplicities the background from the empty-target contamination is substantial. This empty-target contamination consists of events caused by an interaction with the beam-pipe or the air. By taking runs with the target removed this background could be estimated and the lower limit of bin (0) was chosen to reduce the empty-target background. The background in bin (0) is nevertheless about 12% and therefore this amount has to be subtracted from the measured cross section.

The cross section can be calculated directly from the total beam luminosity, which is also measured by NA57 [64]. In table 6.1 the cross sections for interactions in the five centrality classes are given next to the definitions of each bin. In this table also the average number of wounded nucleons (N_w) and the impact parameter for each multiplicity class are given. These can be calculated by means of the *Glauber model* [65], which uses the measured cross section. In this model the number of wounded nucleons are the nucleons which have interacted inelastically at least once with another nucleon. In the right-hand plot of figure 6.1 the distributions of the number of wounded nucleons calculated in the Glauber model are plotted for each multiplicity bin. The values of the average number of nucleons correspond to the values found by WA97, which used the *Wounded Nucleon Model* [66]. In this model the average number of charged particles ($\langle N_{ch} \rangle$) is proportional to the average number of wounded nucleons in the collisions. Note that bin 0 is not measured in WA97.

Table 6.1: Range for number of charged particles N_{ch} and experimental cross section σ_{trig}^{exp} after empty-target subtraction for the five centrality classes of the NA57 experiment. For each class the calculated average number of wounded nucleons $\langle N_w \rangle$ and average impact parameter $\langle b \rangle$ are given. For the N_w distribution is indicated the FWHM, with respect to the value of $\langle N_w \rangle$. The centrality classes are peripheral (0) up to central (IV).

Centr. class	N_{ch}	σ_{trig}^{exp} [barn]	$\langle N_w \rangle$	FWHM	$\langle b \rangle$ [fm]
0	$96.0 \leq N_{ch} < 206.6$	0.95 ± 0.03	62 ± 4	$^{+22}_{-26}$	10.43 ± 0.14
I	$206.6 \leq N_{ch} < 419.8$	1.23 ± 0.03	121 ± 4	$^{+37}_{-42}$	8.57 ± 0.12
II	$419.8 \leq N_{ch} < 664.0$	0.88 ± 0.02	209 ± 3	$^{+41}_{-49}$	6.30 ± 0.09
III	$664.0 \leq N_{ch} < 857.1$	0.49 ± 0.01	290 ± 2	$^{+38}_{-43}$	4.22 ± 0.06
IV	$857.1 \leq N_{ch} < 1191.7$	0.33 ± 0.01	349 ± 1	$^{+41}_{-31}$	2.46 ± 0.02

6.4 Monte Carlo input for the unfolding

In section 6.2 the methods for the unfolding of data have been discussed. For these methods MC events were used for the determination of the response matrix A . Therefore the transformation of the true value of a physical variable x to the reconstructed value y had to be known. In this section

it will be shown how a value x of a generated Monte Carlo distribution $f(x)$ is propagated through the reconstruction process to yield a final value y and a resultant distribution $g(y)$.

In order to get a value of y which is as realistic as possible, the simulated events have to be processed in the same way as the data. Therefore a reconstruction chain was set up, which is comparable with the weighting chain, described in section 6.1. This chain will be described in detail by describing the separate steps.

Step 1: Simulation of particles and detector hits

The particles were simulated in the simulation package GEANT. In this package a precise description of the detectors is given and also the performance and the efficiencies of the separate detector components are stored. The performance of the compact telescope was not constant during the run, but tended to change due to growing noise in the pixel detectors and a varying beam size. In order to use the complete statistics of the experiment it was chosen to perform simulations, in which each run was regarded separately. This means that for every run out of the data period simulations were done with the same efficiencies of the telescope detectors in that run. Furthermore the *run-by-run vertex* and its spread (as defined in section 5.1.1), was used in order to get a good estimate of the beam impact. In this way a realistic simulation of the primary vertex could be established. It was decided to tune the simulation statistics to have an output (after the reconstruction chain was finished) which amounts to about three times the events found for the data.

In order to have a realistic distribution of generated particles, they are generated with a flat rapidity-distribution and a p_T distribution, which is given by an exponential:

$$f(m_T) = m_T \cdot e^{-\frac{m_T}{T}}, \quad (6.41)$$

where $m_T = \sqrt{(p_T^2 + m^2)}$ is the transverse mass and T is the inverse slope parameter. These inverse slopes have been measured in the WA97 experiment for the (multi-)strange hadrons. The inverse slope parameter reflects both the temperature of the fireball, created in the collision and the expansion velocity of this fireball. It was shown that the inverse slope parameters are dependent on the centrality of the collision. NA57 uses the same centrality classes as WA97 and therefore the particles were generated in these classes. The particles in the separate classes were generated according to the number of particles found in these classes in the data. NA57 has extended the centrality range and an extra multiplicity bin (0) was added. At the time the simulations were performed, the preliminary weighting results for the Λ s were known [61], and these were taken as the inverse slope input for the Λ and $\bar{\Lambda}$ simulations. The NA57 K_S^0 slopes however were not yet determined and therefore the WA97 slopes [67] were used and the value of the slope for bin (0) was taken the same as the value for the second bin. In table 6.2 the inverse slopes used in the simulations, together with the fraction of generated events per class are shown.

Dividing the generated sample into multiplicity bins, makes it possible to mix the particles with events from the data of the same multiplicity class. The mixing of simulated events with data events is the next step.

Step 2: Mixing

In order to get a realistic background of tracks and noise the simulated particles have been mixed with events from the data. The particles generated in **step 1** yield hits in the detectors according to

Table 6.2: Values for the inverse slope parameters used and fraction of events for each multiplicity class generated in the GEANT simulations.

Particle		0	I	II	III	IV
$\Lambda/\bar{\Lambda}$	Slope (Mev)	258	261	276	313	310
	Fraction (%)	6.9	21.6	29.4	23.1	19.0
K_S^0	Slope (Mev)	224	224	231	232	232
	Fraction (%)	7.0	22.0	29.3	23.0	18.7

the efficiencies determined by the PLANEFF program. These hits are then embedded in the data. For this purpose background files have been created. In these files runs from a specific run period are clustered together and every 200th event from this period is written away to the background file. In this way the simulated event from a certain run can be mixed with an event from the same run period. Another demand on the event to be mixed is that it is from the same centrality class as the simulated event.

Step 3: Particle selection

This step runs the reconstruction program ORHION, as described in section 4.1, and obtains a first selection of V^0 candidates. This sample is then analyzed by the program ANALYZE with exactly the same selection criteria as used for the data (see section 5.2.1). The resultant sample then consists of two types of particles: the data particles and the simulated particles embedded in the events. In the next step the simulated particles will be extracted.

Step 4: V^0 matching

In this step the program WGTCAL checks for each selected V^0 candidate whether it matches with the characteristics (i.e. detector hits) generated by GEANT in the same event.

When a match occurs the information about the characteristics of the generated and the reconstructed particle (like transverse mass, rapidity and internal decay angles) is stored. This output will yield the $g(y)$ distribution of the reconstructed physical variable as well as the transformation from $x \rightarrow y$. The distribution generated in **step 1** will give $f(x)$.

6.4.1 Simulation results

In order to check the accuracy of the simulations for different characteristics of the particles a comparison is made between the data distribution and the simulated distribution. These comparisons are given in figures 6.2- 6.4. Note that the number of simulated events is about three times as large as the data sample. Therefore the distributions regarded are normalized with respect to each other.

In figure 6.2 the comparison is plotted between the charged-particle distribution of the data and the distribution of the data events which have been mixed with the simulated data. The comparison shows that the charged-particle distribution from the mixed events is clearly divided in the multiplicity bins and that in each bin it is peaked towards the lowest multiplicities in the bin. This is because the distribution of the number of charged particles is rapidly increasing towards lower multiplicities (see figure 6.1) and in the mixing all events are used (and not only those with a Λ). Still the events generated in different classes are mixed accordingly with the background events and the relations between the bins are kept.

In figure 6.3 the kinematical characteristics of the Λ s are compared. As can be seen the momentum distributions agree very well. The only discrepancy between the data and the simulations can be seen when the distributions for the V^0 decay parameters are plotted (see figure 6.4). The distribution of the beam impact position in the Y-direction is smaller for the data than for the simulations. This is because in the generation of the particles a Gaussian is assumed. However for the data the shape is not Gaussian and because it is asymmetric for positive values of b_y the distributions disagree. However this discrepancy does not seem to affect other distributions critically.

Since the deconvolution method intends to correct for detector effects like limited acceptance

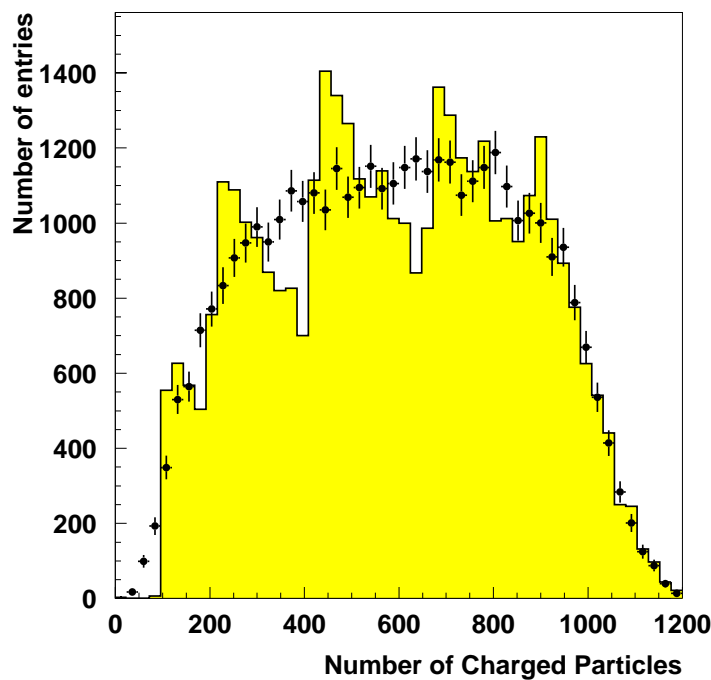


Figure 6.2: Comparison between the data charged-particle distribution (data points) and the relative distribution of the events used for mixing (histogram).

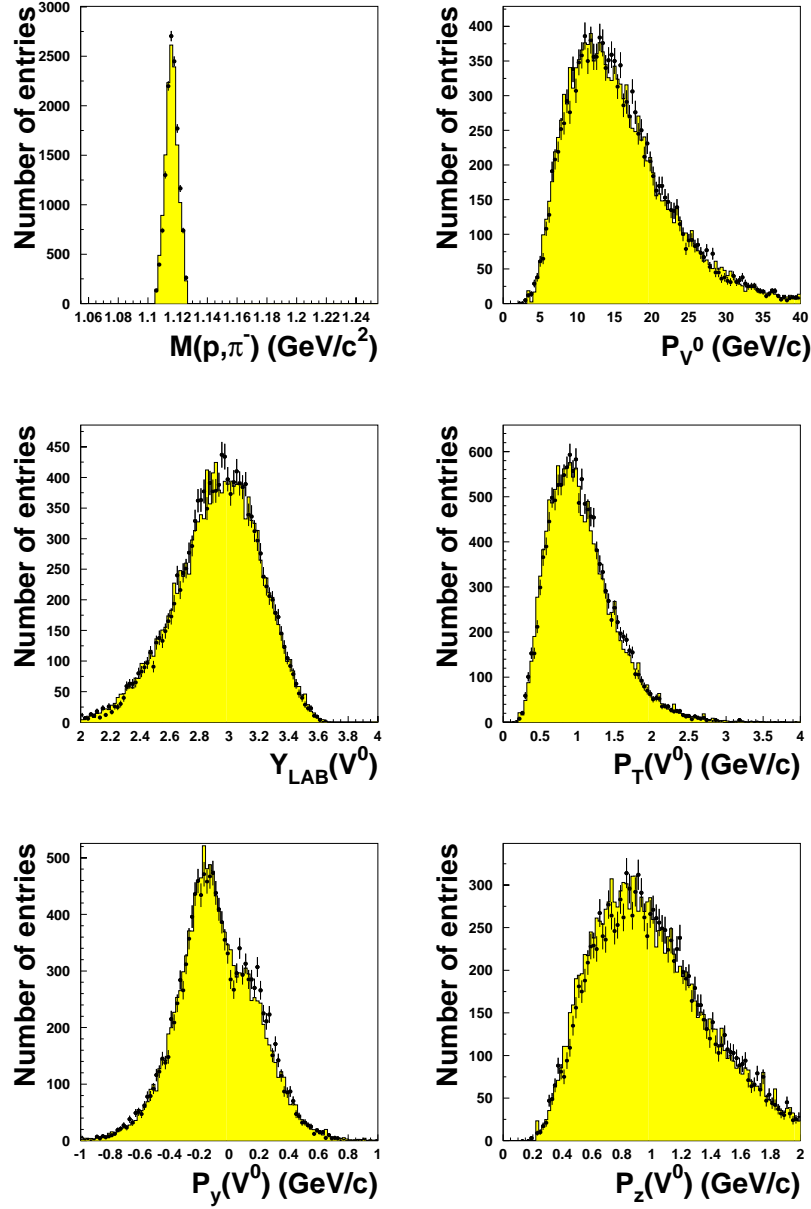


Figure 6.3: Comparison between data kinematical distributions (data points) and the relative simulated distributions (histogram) for the Λ . From top left to right bottom the variables plotted are: invariant mass, total V^0 momentum, rapidity, transverse momentum, momenta in the laboratory Y-direction (p_y) and Z-direction (p_z).

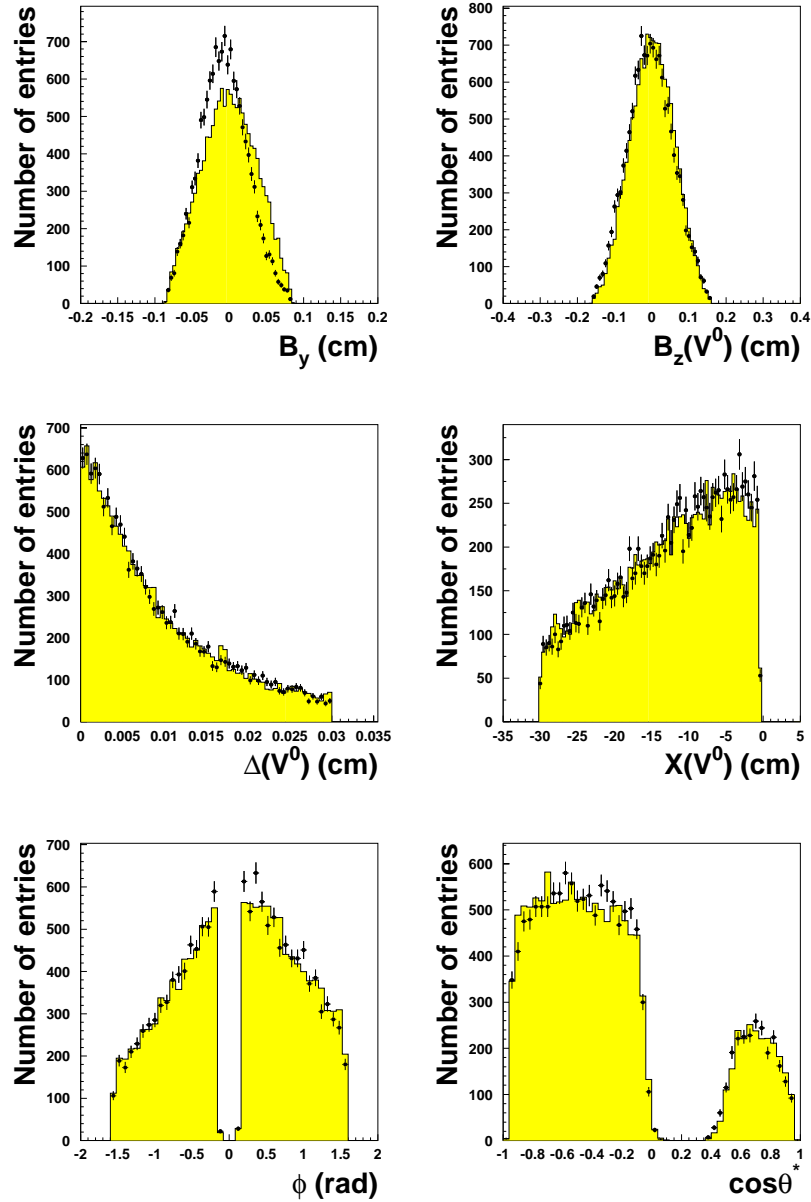


Figure 6.4: Comparison between data decay parameter distributions (data points) and the relative simulated distributions (histogram) for the Λ . From top left to right bottom the variables plotted are: beam impact position in the Y-direction b_y and Z-direction b_z , distance of closest approach, secondary decay vertex X-position, internal decay angle ϕ , longitudinal angular distribution in the CMS of the Λ .

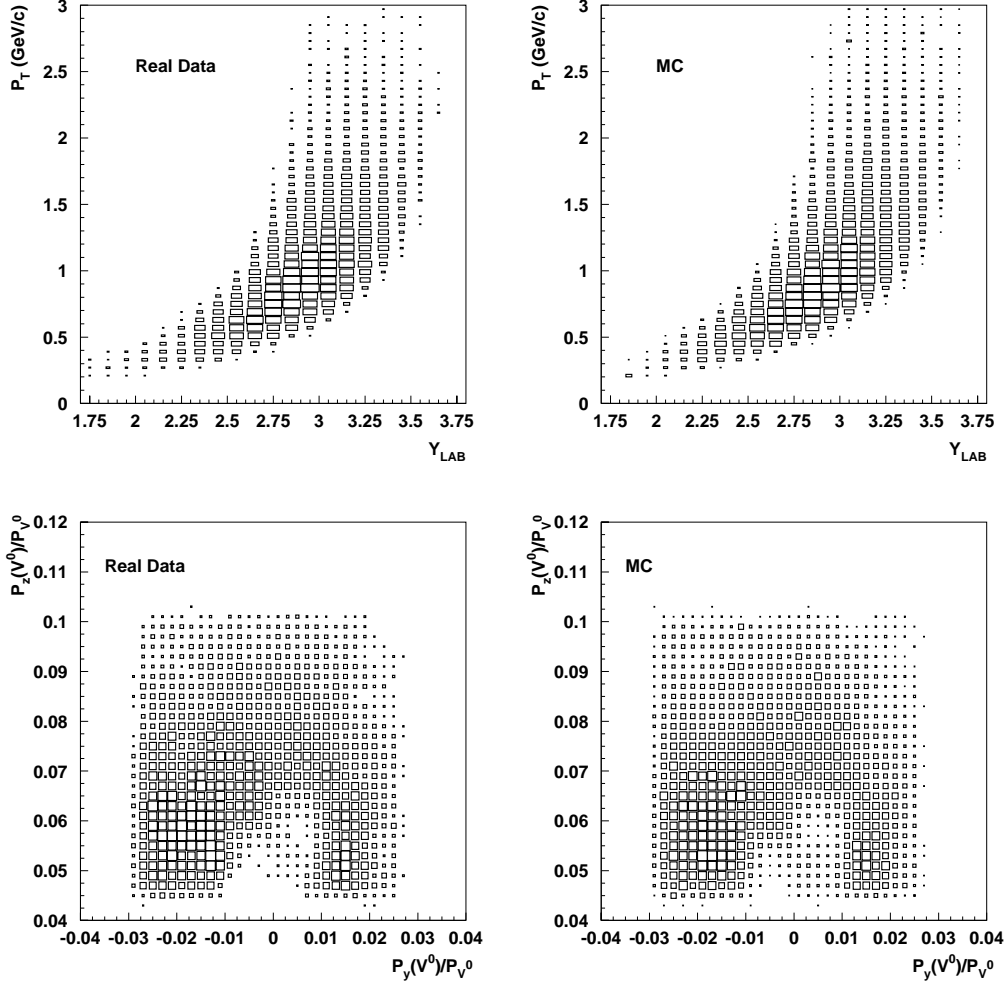


Figure 6.5: Comparison between data acceptance regions (left) and the regions of simulated data (right) for the Λ . The top pictures represent the $p_T - y$ acceptance. The bottom plots show the acceptance of the compact telescope.

and detector efficiency it is interesting to look at the comparison of these. In figure 6.5 on the top the $p_T - y$ acceptance of the NA57 setup is depicted for data and simulations. The simulations manage to reproduce the acceptance shape down to a value of the rapidity of 2. This is because in the simulations only particles have been generated with this value as lower limit. In the bottom plots the scatter-plots are shown for the acceptance of the momenta in the Y- and Z-direction, p_y and p_z , relative to the total momentum $p(v^0)$. In this way an approximation of the detector accep-

tance in the Y-Z plane can be made and hence indirectly the efficiency of the compact telescope can be rendered. During the Pb1995 run of WA97 some of the pixel detectors were damaged near the beam (i.e. the bottom part of the detectors). This radiation damage can be seen at the bottom in the scatter-plot, where a hole is visible. This hole is reproduced in the scatter-plot of the simulation.

In conclusion, the simulations seem to reproduce the data distributions accurately. The simulations for the $\bar{\Lambda}$ are equivalent to the simulations for the Λ and hence are not shown here.

For the K_S^0 the comparison between data and simulations can be seen in figures 6.6- 6.7. Similarly to the Λ the b_y distribution is not reproduced correctly. Furthermore the mean of the K_S^0 invariant mass distribution is shifted to a higher value.

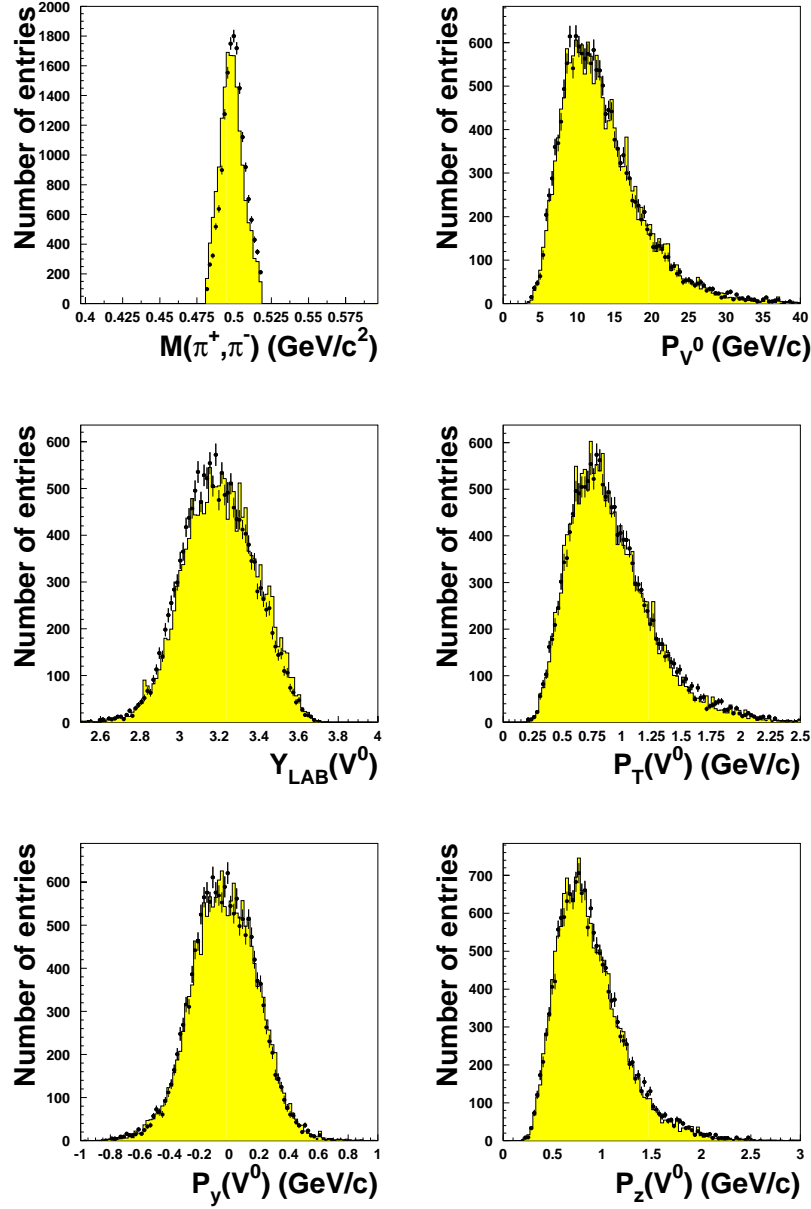


Figure 6.6: Comparison between data kinematical distributions (data points) and the relative simulated distributions (histogram) for the K_S^0 . From top left to right bottom the variables plotted are: invariant mass, total V^0 momentum, rapidity, transverse momentum, momenta in the laboratory Y-direction (p_y) and Z-direction (p_z).

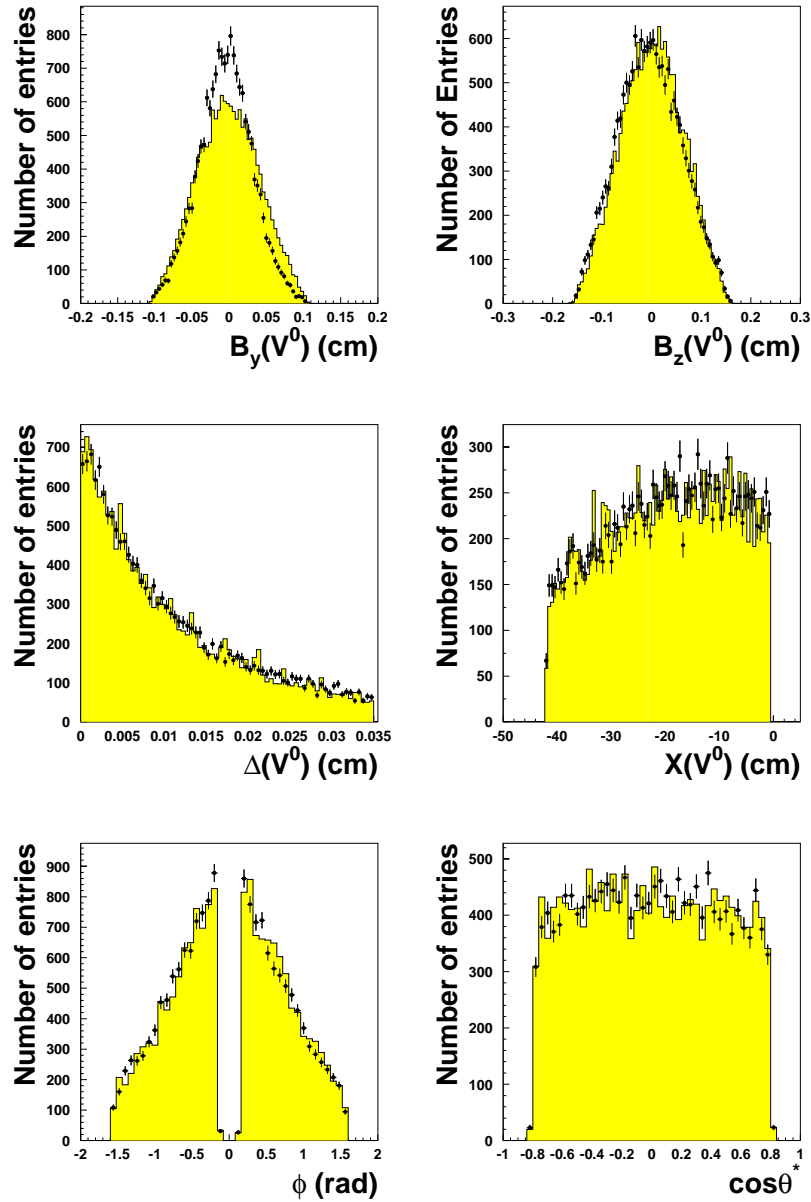


Figure 6.7: Comparison between data kinematical distributions (data points) and the relative simulated distributions (histogram) for the K_S^0 . From top left to right bottom the variables plotted are: beam impact position in the Y-direction b_y and Z-direction b_z , distance of closest approach, secondary decay vertex X-position, internal decay angle ϕ , longitudinal angular distribution in the CMS of the K_S^0 .

7

**Inverse slopes and
yields**

The main goal of the NA57 experiment is to look at the production of (multi-)strange particles at mid-rapidity. The yields of the particles determined in chapter 5 are raw yields and they have to be corrected for detector and reconstruction effects. The method which will be used for this correction, the deconvolution of data, has been introduced in the previous chapter. In this chapter the transverse mass distributions and the yields will be retrieved by using the deconvoluted data for the Λ , $\bar{\Lambda}$ and K_S^0 particles. The yields will be deduced by using the rapidity and transverse mass distributions. Therefore first the deconvolution procedure will be described for the unfolding of the raw rapidity and transverse mass distributions in section 7.1. The results of this deconvolution procedure will then be used to calculate the inverse slope parameters of the produced particles (section 7.2), which then will be used finally to produce the particle yields (section 7.3).

7.1 Deconvolution procedure

The inverse slope parameters can be found by fitting the following double differential to the corrected data:

$$\frac{d^2 N}{dy dm_T} = f(y, m_T) = A f(y) m_T \exp \left\{ -\frac{m_T}{T} \right\}, \quad (7.1)$$

where it is assumed that the rapidity distribution $f(y)$ is flat in the region of acceptance and A is a normalization factor. The true $y - m_T$ distribution used for the fit will be extracted by deconvolution, which implies that a two-dimensional deconvolution procedure has to be used. In the WA97 experiment the deconvolution method has been successful in determining inverse slopes and yields [67]. Therefore the deconvolution method used by WA97 will also be applied to the NA57 data. In the following the procedure developed by WA97 will be explained and its application to the NA57 will be described.

7.1.1 Discretization

In the last chapter it was shown that the original distribution f can be retrieved from the measured distribution g by the equation:

$$f(x) = \int A(x, y) g(y) dy. \quad (7.2)$$

In this equation the distributions $f(x)$ and $g(y)$ are taken as one-dimensional. When a two-dimensional distribution has to be unfolded, this first has to be transformed into a vector. This transformation can be obtained by starting from the matrix equation:

$$g = Af, \quad (7.3)$$

where g and f are vectors and A is a matrix. The discretization of the two-dimensional distribution can now be done by first representing it by a two-dimensional histogram, which is then transformed to a vector. The concept of this transformation is rendered in figure 7.1, where the acceptance region of the NA57 experiment for Λ s is depicted. The boundaries of the acceptance region are indicated by the two lines. The two-dimensional $y - m_T$ space is divided in bins, which is shown as a grid in the plot. It can be seen that some bins lie on the edge of the acceptance

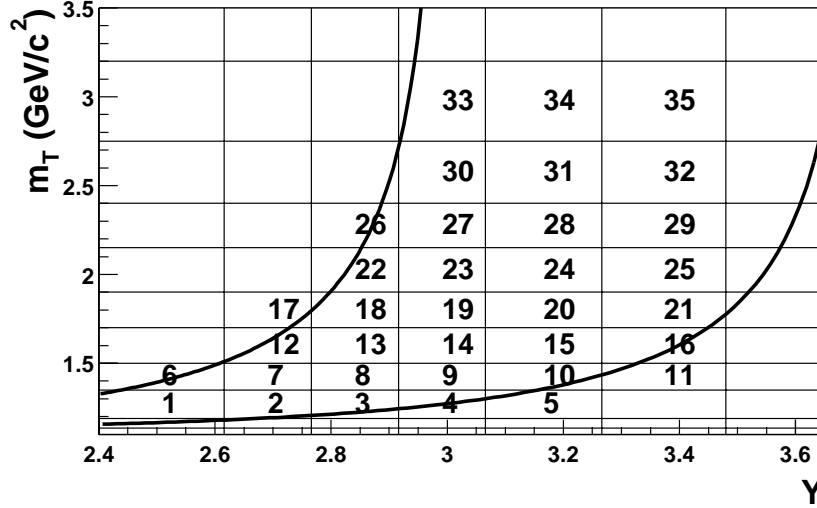


Figure 7.1: Discretization of the two-dimensional $y - m_T$ distribution.

region. This can cause the bin to have low statistics. These bins have a great statistical uncertainty and could introduce oscillations in the deconvolution solution (see section 6.2.2). In order to remove the bins which have very few entries, their average bin content is determined. When a histogram bin has less than a twentieth of this average it is left out. In the plot some of the bins which are on the boundary have less than a twentieth of the average and are not used. After only the statistical significant entries are left, these are reordered: starting left under, the contents of the entry belonging to the first m_T bin and the corresponding y bins are copied to the vector f , this is done for each bin, until the whole $y - m_T$ range has been covered. This sequence of reordering is shown in figure 7.1 by plotting the numbers of the corresponding vector entry into the selected bins. From the possible 64 bins only 35 are significant.

This discretization procedure yields an expansion of the form of equation 6.8 where the eigenvectors are now the step functions (which are not normalized):

$$p_j(x) = \begin{cases} 1 & \text{for } t_{j-1} \leq x < t_j \\ 0 & \text{otherwise} \end{cases}, \quad (7.4)$$

where the nodes $t_0, t_1, t_2 \dots t_m$ are defined by the histogram bin limits and the coefficients a_j are given by the number of entries in the bin. Note that the step functions of equation 7.4 are B-splines of the zeroth order. The discretization of the two-dimensional distribution to a vector with the step function causes the represented histogram f to have discontinuities. In order to prevent a loss of accuracy the number of bins used for the discretization should be as large as possible.

Here problems can occur; in the previous chapter it was shown that the limited resolution of an experiment is a serious parameter in the deconvolution of distributions. The bin sizes have to be chosen such as to prevent large correlations between data points. Furthermore it was shown that this limited resolution will be taken into account by a regularization procedure. This will result in optimization of the bin size of the histogram (see section 6.2.3). However one can also argue the other way around: by choosing the bin limits in such a way that it takes into account the limited resolution of the variables used, regularization is not necessary. This will be explained in the next section.

7.1.2 Bin definition

In order to achieve the best possible binning it is important to look at the resolution of the variables. In figure 7.2 the correlation between the generated and reconstructed rapidity and transverse mass are shown. In figure 7.3 the difference between generated and reconstructed values are plotted. From these plots it can be seen that the resolution in these variables is good and that it is possible to perform a discretization in which not too much information on the shape of the original distribution is lost. For the deconvolution of the data of the WA97 experiment it was shown that it was possible to choose the binning such that the inversion performed was stable and no regularization was necessary [67]. Therefore to obtain a good binning the following procedure was done; first some *a priori* binning was taken, which was assumed to be reasonable. Then the value for the standard deviation was calculated for this bin by using all events generated within this bin:

$$\bar{\sigma} = \sqrt{\frac{\sum_{i=1}^N (x_{gen}^i - x_{rec}^i)^2}{N}}, \quad (7.5)$$

where $\bar{\sigma}$ is the standard deviation for a specific bin, x_{gen}^i is the generated and x_{rec}^i is the reconstructed value of the variable x , and N is the number of events with x_{gen} within bin limits. Now the size of the bin can be expressed in the number of standard deviations:

$$\eta = \frac{t}{\bar{\sigma}}, \quad (7.6)$$

where t is the bin width and η is the number of standard deviations for that bin, which will be referred to as the *bin resolution* coefficient. Considering the fact that the bins are two-dimensional there are two bin resolution coefficients which have to be determined. In figure 7.4 the bin resolution coefficients of the rapidity and transverse mass are plotted for each bin.

The vertical axis is displayed in a logarithmic scale which implies that a value of less than 1 of η has a negative value. In this case the bin width is less than one standard deviation of the resolution defined by the events which it encompasses. In this case data correlations could occur. This will make the inversion of the matrix A unstable and therefore a value bigger than one is preferred for η . For this analysis it was chosen to tune the bin widths such that an average value 2 for η was achieved for both the rapidity and the transverse mass bin size. This means that the probability to find an event in the right bin after the deconvolution is about 85% (see [14]). With this criterium the number of used bins is still large enough to achieve an accurate solution for the deconvoluted result. The figure shows that most bins have a good resolution and only some border bins, where

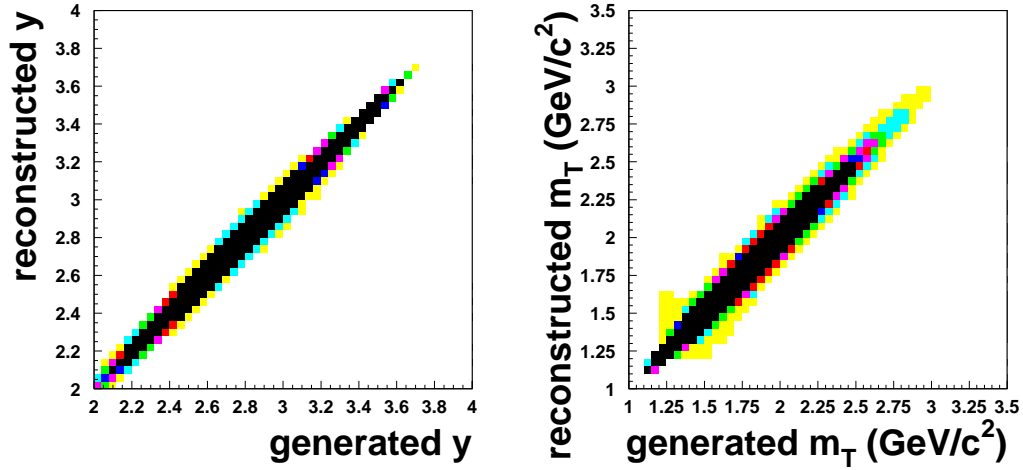


Figure 7.2: Correlation between generated and reconstructed rapidity (left) and transverse mass (right).

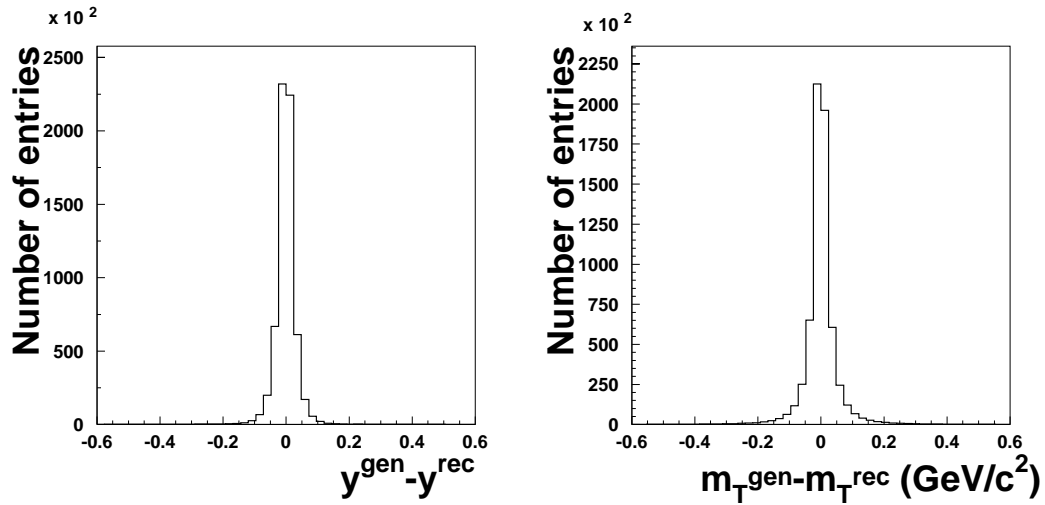


Figure 7.3: Difference between generated and reconstructed kinematic variables: rapidity (left) and transverse mass (right).

statistics is limited, have a value smaller than 1 for η . The effect of these bins on the stability of the inversion seems to be small.

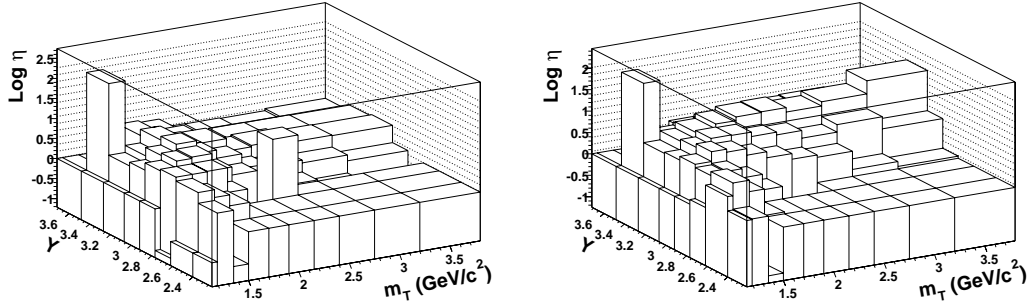


Figure 7.4: Bin resolution coefficients in the rapidity range (left) and in the transverse mass range (right) for each bin. The coefficients are plotted on a log scale.

After the optimization of the bin widths it is now possible to determine from the simulations the matrix A . When on the right side of equation 7.3 the vector $v = [1, 0, \dots, 0]$ is substituted, the first column of A is obtained: $A_v = [A_{11}, A_{21}, \dots, A_{N1}]$. This is equal to g_{MC} , the reconstructed distribution of all generated MC events in the first bin. By repeating this for all bins of the vector f , the matrix A can be constructed from all resultant columns. Once matrix A is determined, its inversion will result in solving equation 6.5.

7.1.3 Stability check

The result of the deconvolution in the $y - m_T$ space is shown in figure 7.5. The plot shows a nice two-dimensional distribution and no oscillations seem to have occurred. In order to check whether the result is stable also the rotated coefficients \hat{a}_1 (which are defined by equation 6.22) of the solution are plotted. Since their corresponding covariance matrix is equal to unity (see section 6.2.2), their values should be bigger than one in order to avoid oscillations. The values of the coefficients \hat{a}_1 are plotted in figure 7.6.

The vertical axis is rendered in logarithmic scale which implies that negative entries could give rise to oscillations. There is no coefficient which is smaller than 1, so it is safe to assume that the unfolding has been successful and that no regularization is necessary. In the next section the deconvolution result will be used to determine the inverse slopes.

7.2 Inverse slopes

The deconvoluted distribution obtained is now fitted using the expression 7.1, where a flat rapidity region is assumed and the inverse slope was left as a free parameter of the fit. This was done by a χ^2 fit. For the weighting procedure usually the maximum likelihood method is used. In order to make a comparison with the results found by the weighting method the same region of acceptance was used for the fit of the deconvolution data. The binning used for the unfolding was chosen such that the border bins of the deconvolution region fall outside of the weighting acceptance region.

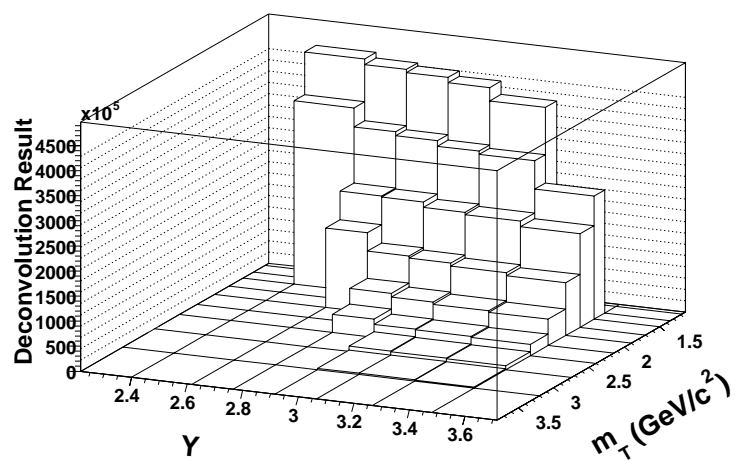


Figure 7.5: Result of the deconvolution of the measured $y-m_T$ distribution for the total Λ sample.

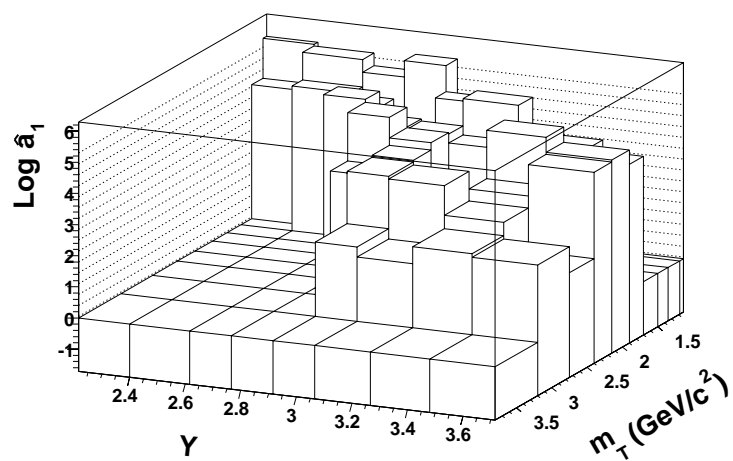


Figure 7.6: The values of the rotated coefficients \hat{a}_1 of the unfolded solution.

When applying the fit, the border bins of the deconvolution result are left out. The values chosen for the region-of-good-acceptance in the weighting for the Λ and $\bar{\Lambda}$ [61] are:

- $0.41 \text{ GeV}/c < p_T < 3.0 \text{ GeV}/c$
- $2.4 < y < 3.48$
- $51 \text{ mrad} < \theta < 92 \text{ mrad}$

and for the K_S^0 [60]:

- $0.55 \text{ GeV}/c < p_T < 2.7 \text{ GeV}/c$
- $2.93 < y < 3.7$
- $49 \text{ mrad} < \theta < 92 \text{ mrad}$,

where θ is the polar angle between the Λ and the beam axis. It must be stressed that for the deconvolution the cut on θ has not been applied, since the choice of binning already makes a selection of the acceptance window equivalent to the θ cut.

7.2.1 Inverse slope parameters as function of centrality

In order to investigate the dependence of the inverse slopes on the centrality, the data sample has been divided into centrality classes (see section 6.3). For each centrality class the data have been

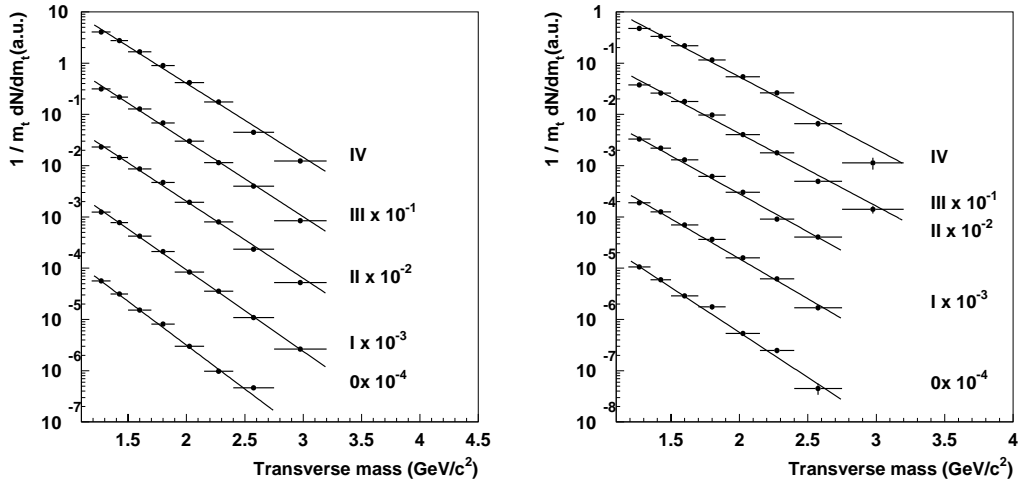


Figure 7.7: Transverse mass distributions for the Λ (left) and the $\bar{\Lambda}$ (right). The results for all centrality classes are plotted in one plot, where the lower centrality bins are scaled for visual convenience

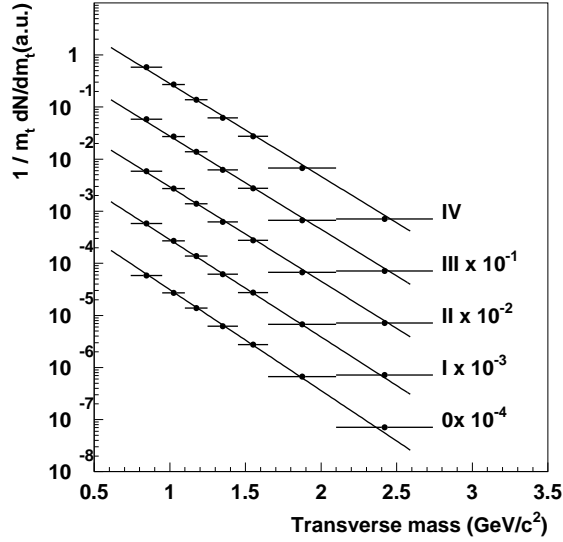


Figure 7.8: Transverse mass distribution of the K_S^0 .

deconvoluted and the resulting spectra have been fitted (figures 7.7- 7.8). For each particle type the m_T spectra of each multiplicity class have been plotted, where for visual convenience the spectra of lower centrality classes have been scaled. Furthermore the data points are put at the average of the bin and its width gives the error. The errors on the slopes are only statistical and consist of two contributions: the statistical error due to the data statistics and the error introduced due to the statistical uncertainty of the response matrix A . In the case this matrix would be determined with an infinite number of events, the response would be defined completely. The statistics used, however, is not infinite and therefore the error in the result due to the statistical uncertainty in the contents of A has to be estimated. This has been done by sampling from a Poisson distribution for each entry of the matrix and then calculating the slope again. This procedure has been repeated 100 times and the spread in the distribution of slopes found is taken as the deconvolution error. This error is about a factor 0.75 of the statistical error from the data. This is reasonable since the simulation sample is roughly 3 times larger than the data sample.

The found inverse slope parameters for the Λ and $\bar{\Lambda}$ are also plotted as a function of the number of wounded nucleons (fig. 7.9- 7.10). In the same plots also the slopes calculated with the weighting method are depicted [61]. The results for the deconvolution method and the weighting method agree within errors. As can be seen from the comparison, the slopes determined by the weighting method have substantially larger errors. This is because the statistics used for the deconvolution method covers all data, while the weighting only has used 1/200th of the statistics for the Λ and 1/10th of the $\bar{\Lambda}$ sample.

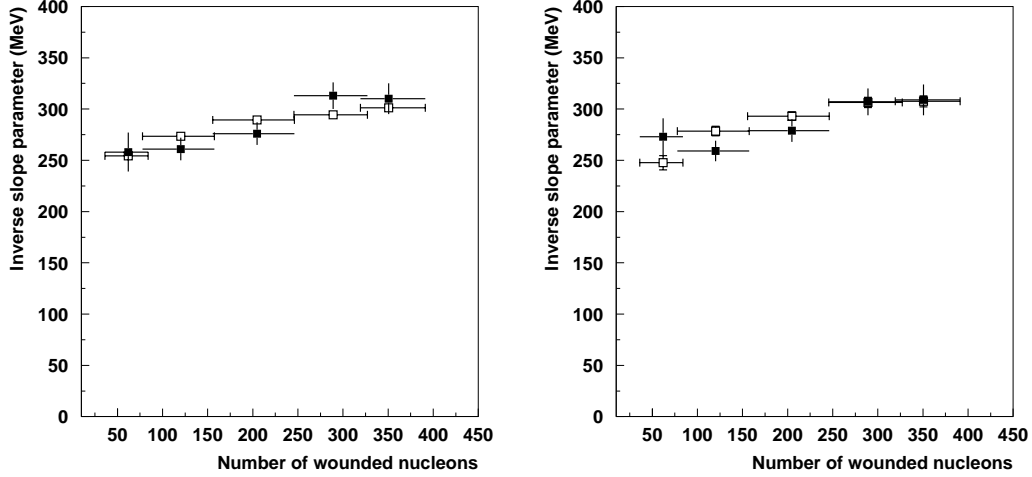


Figure 7.9: Inverse slope parameters for Λ (left) and $\bar{\Lambda}$ (right) particles as a function of the number of wounded nucleons. The results found by using deconvolution (open squares) are compared to those found by using the weighting method (closed squares).

The results shown in the plots are listed in tables 7.1- 7.3. Here also the results from the deconvolution of the WA97 data are shown [67]. Although for the WA97 experiment only the four most central multiplicity classes were looked at, the results for these classes agree also with the results presented in this thesis for the Λ and $\bar{\Lambda}$.

The slopes for the K_S^0 however do not agree very well with the results from WA97. There is a systematic 3σ difference between the slopes found by NA57 and those found by WA97. The reasons for this could be located in the fact that at high values of p_T for the K_S^0 systematic effects tend to dominate, which causes the slopes to be overestimated. The nature of these systematic effects will be looked into in more detail in the next chapter.

Table 7.1: Values for the inverse slope parameters T (in MeV) of the Λ for WA97 and for the two correction methods used in NA57.

	0-IV	0	I	II	III	IV
NA57 (D)	288.0 ± 0.5	254.2 ± 1.7	273.5 ± 1.0	289.4 ± 0.9	294.4 ± 1.1	301.1 ± 1.1
NA57 (W)	284 ± 6	258 ± 19	261 ± 11	276 ± 11	313 ± 13	310 ± 15
WA97 (D)	289 ± 3	-	271.3 ± 3.1	286.2 ± 3.1	302.0 ± 4.0	295.6 ± 4.2

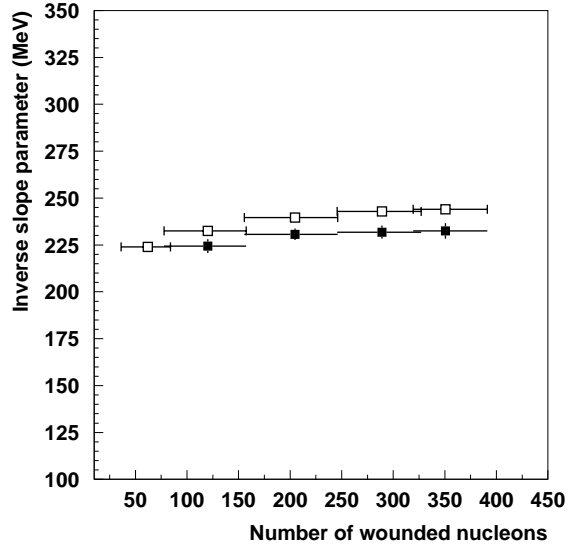


Figure 7.10: Inverse slope parameters for K_S^0 particles as a function of the number of wounded nucleons. The results found by using deconvolution in NA57 (open squares) are compared to those measured in WA97 with the deconvolution method (closed squares).

Table 7.2: Values for the inverse slope parameters T (in MeV) of the $\bar{\Lambda}$ for WA97 and for the two correction methods used in NA57.

	0-IV	0	I	II	III	IV
NA57 (D)	289.9 ± 1.3	247.6 ± 4.4	278.5 ± 3.0	293.0 ± 2.7	306.4 ± 3.2	307.4 ± 3.4
NA57 (W)	286 ± 6	274 ± 18	258 ± 10	279 ± 10	307 ± 13	309 ± 14
WA97 (D)	287 ± 4	-	268.0 ± 4.2	279.8 ± 4.2	299.6 ± 5.0	304.2 ± 6.4

Table 7.3: Values for the inverse slope parameters T (in MeV) of the K_S^0 for WA97 and for the two correction methods used in NA57.

	0-IV	0	I	II	III	IV
NA57 (D)	233.5 ± 0.4	224.0 ± 1.2	232.5 ± 0.7	239.6 ± 0.7	242.9 ± 0.7	244 ± 0.8
NA57 (W)	235 ± 8	-	-	-	-	-
WA97 (D)	230 ± 2	-	224.4 ± 3.7	230.7 ± 3.1	231.8 ± 3.5	232.5 ± 4.1

7.3 Yields

The absolute yields of the strange particles have been determined in the WA97 and NA57 experiment by extrapolating the measured particle yield to the complete region defined by $|y - y^*| < 0.5$ and $p_T > 0$ GeV/c

$$Y = \int_{m_\Lambda}^{\infty} dm_T \int_{y^*-0.5}^{y^*+0.5} dy \frac{d^2N}{dy dm_T}, \quad (7.7)$$

where y^* is the value of y at mid-rapidity and Y is the total particle yield for one unit around mid-rapidity.

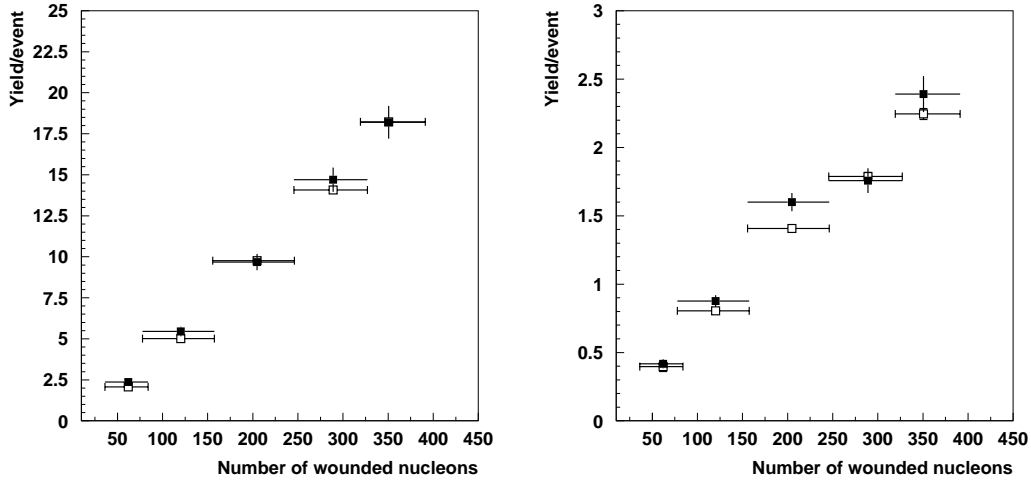


Figure 7.11: Yield per event for Λ (left) and $\bar{\Lambda}$ (right) particles as a function of the number of wounded nucleons. The results found by using deconvolution (open squares) are compared to those found by using the weighting method (closed squares).

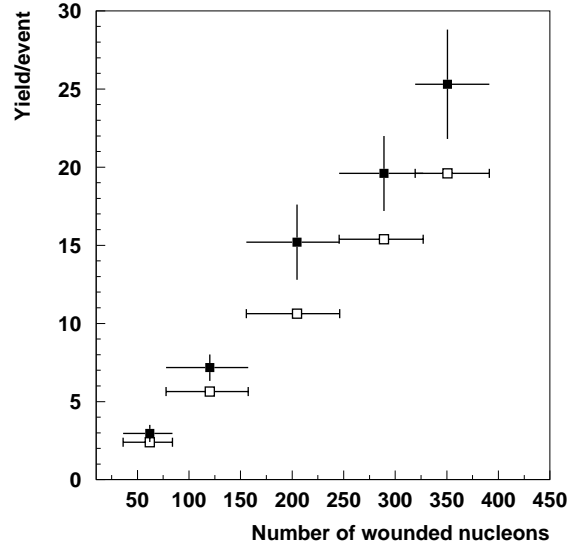


Figure 7.12: Yield per event for K_S^0 particles as a function of the number of wounded nucleons. The results found by using deconvolution (open squares) are compared to those found by using the weighting method (closed squares).

The extrapolation has made use of the inverse slope parameters found by the transverse mass fit, described in the last section. The assumption of a flat rapidity distribution is a good estimate but is not completely correct. This introduces a systematic error for the particle yields which is less than 6% for Λ and 5% for $\bar{\Lambda}$ [62]. The extrapolation can be done in two ways: by first extrapolating over rapidity and then the transverse mass, second by going the other way around. This consistency check gives similar results and the final result is taken as the average with the corresponding error. The value calculated from equation 7.7 is the absolute yield and in order to

Table 7.4: Values for the yields per event for the different centrality classes of the Λ for WA97 and for the two correction methods used in NA57.

	0	I	II	III	IV
NA57 (W)	2.37 ± 0.22	5.45 ± 0.3	9.68 ± 0.5	14.7 ± 0.74	18.2 ± 1.0
NA57 (D)	2.06 ± 0.03	5.02 ± 0.03	9.77 ± 0.04	14.08 ± 0.06	18.22 ± 0.10
WA97 (D)	-	4.41 ± 0.08	8.73 ± 0.15	11.52 ± 0.22	15.22 ± 0.35

get the yield per event, it has to be divided by the number of events taken by the experiment. An overview for all particles yields are given in tables 7.4- 7.6.

In figures 7.11-7.12 the yields per event for each multiplicity class calculated for the deconvoluted data are shown. Again the results found by using the weighting method are also depicted. In this case the preliminary weighted yields of NA57 for the K_S^0 were available [60]. Also for the yields the results for both methods are compatible in case of the Λ and $\bar{\Lambda}$. For the K_S^0 however also here the results do not agree. This could be a direct consequence of the K_S^0 slope results. If these are overestimated the extrapolation will result in an underestimation of the yields.

Strangeness enhancement usually is measured by looking at the yield per event with respect to the yields found for p-Be interactions. This can be pictured best by dividing the yields per event of the Pb-Pb collisions, by the values found for p-Be. The resulting relative yield is divided again by the average number of wounded nucleons in the centrality bin. The final result can be seen in figure 7.13. For comparison the same measurements found by WA97 are also plotted. The results for the Λ and the $\bar{\Lambda}$ are the results of the analysis presented here. The Λ yields show a small increase with respect to the number of wounded nucleons, while the $\bar{\Lambda}$ relative yields are flat. The results for the $\bar{\Lambda}$ do not show a significant drop in the lowest centrality bin, which was seen for the $\bar{\Xi}$. In the common centrality range the results from NA57 and WA97 agree within 20%. The difference has been extensively investigated [70] and it has been understood as due to a bias introduced by the uncertainty in the position of the primary vertex in WA97 [71].

Table 7.5: Values for the yields per event for the different centrality classes of the $\bar{\Lambda}$ for WA97 and for the two correction methods used in NA57.

	0	I	II	III	IV
NA57 (W)	0.42 ± 0.03	0.88 ± 0.04	1.60 ± 0.07	1.76 ± 0.09	2.39 ± 0.13
NA57 (D)	0.40 ± 0.03	0.80 ± 0.03	1.41 ± 0.02	1.79 ± 0.02	2.24 ± 0.03
WA97 (D)	-	0.61 ± 0.02	1.20 ± 0.04	1.71 ± 0.08	2.04 ± 0.09

Table 7.6: Values for the yields per event for the different centrality classes of the K_S^0 for WA97 and for the two correction methods used in NA57.

	0	I	II	III	IV
NA57 (W)	2.96 ± 0.54	7.17 ± 0.85	15.2 ± 2.4	19.6 ± 2.4	25.3 ± 3.5
NA57 (D)	2.39 ± 0.02	5.64 ± 0.03	10.63 ± 0.04	15.39 ± 0.05	19.60 ± 0.05
WA97 (D)	-	7.0 ± 0.17	13.6 ± 0.26	20.8 ± 0.5	22.3 ± 0.7

The results presented in this chapter show that the deconvolution method is able to determine the inverse slope parameters and yields and that it furthermore enables the use of the full statistics. This results in smaller statistical errors than obtained for the weighting method.

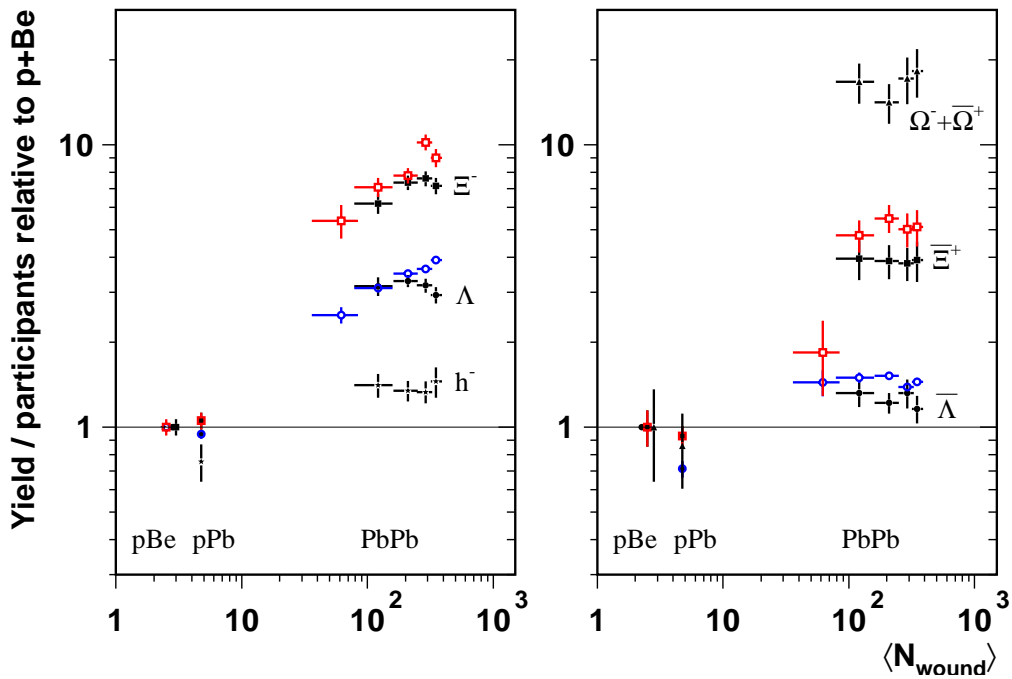


Figure 7.13: The yield per event divided by $\langle N_{\text{W}} \rangle$ and relative to p-Be interactions. The values (open circles) of Λ and $\bar{\Lambda}$ are the results presented in this thesis, the WA97 results are indicated with closed circles.

8

Polarization

Recently for the first time a significant transverse polarization has been measured in high energy heavy ion collisions [5]. This measurement, where the transverse polarization was observed to increase with x_F , showed that even in central Au-Au collisions information of the incoming projectile was retained. It is interesting to investigate whether this is still the case in a lower x_F range for Pb-Pb collisions at 158 AGeV/c. In this region models, which assume no QGP formation, still predict some polarization, while the creation of a QGP could cause the transverse polarization to be reduced. In this chapter the transverse polarization of the Λ s measured in Pb-Pb collisions in the NA57 experiment will be investigated. The polarization can be determined by a study of the angular distributions of the decay products of the Λ . Due to the limited acceptance of NA57, the measured angular distributions are changed and have to be corrected. Analogously to the previous chapter this correction will be applied by deconvoluting the data. The conditions for the deconvolution procedure will be discussed in section 8.1, where only the case for the Λ will be described. Then first the transverse polarization will be determined for K_S^0 in section 8.2, since this particle has no polarization. This analysis gives a rough measure of the false asymmetry due to the geometry of the setup. Then the transverse polarization of the Λ and $\bar{\Lambda}$ will be determined in section 8.3. Parallel to the measurement of the transverse polarization the longitudinal polarization will be derived and systematic effects will be investigated for the Λ . Finally a discussion of the results is given in section 8.4.

8.1 Deconvolution procedure

In this section the conditions for deconvoluting the angular distributions of the decay products will be described. This will be done in the same manner as described in chapter 7, where the conditions for the m_T - y deconvolution were discussed. Since the study of the Λ polarization is the purpose of this chapter, emphasis will be on this particle.

8.1.1 Angular distributions

The NA57 experiment measures Λ production in the channel $\Lambda \rightarrow p + \pi$ by detecting the proton and the pion. Parity violation in this weak decay channel can introduce an asymmetry in the decay angles [73]. The angular distribution of the decay proton in the center of mass frame of a completely polarized Λ is given by [72]:

$$\frac{dN}{d\Omega} = \frac{1}{4\pi} [1 + \alpha \cos \theta], \quad (8.1)$$

where α is the decay asymmetry parameter for this decay channel ($=0.642 \pm 0.013$ [73]) and θ is the angle between the proton of the decaying Λ and the Λ polarization axis. This is schematically shown in figure 8.1. Here the projectile from the beam hits a nucleon in the target and produces a Λ . The production plane is spanned by the beam and the Λ and its normal is defined by:

$$\vec{n} = \frac{\vec{p}_{beam} \times \vec{p}_{\Lambda}}{|\vec{p}_{beam} \times \vec{p}_{\Lambda}|}. \quad (8.2)$$

When the decay of the Λ in its center of mass system is considered, the following coordinate system will be defined: the z-axis is taken in the original direction of the Λ and the y-axis is

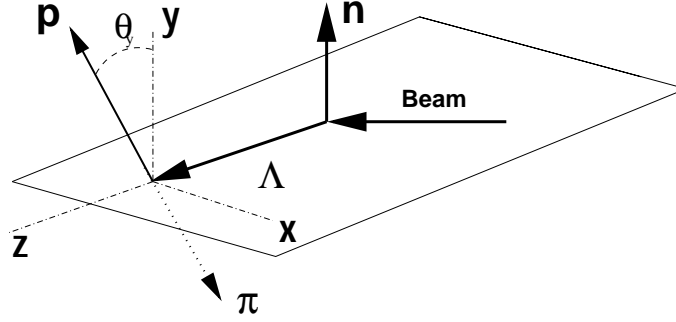


Figure 8.1: Momentum Vector diagram of the production of the Λ and its decay. The decay is shown in the center of mass of the Λ . The y -axis is taken to be parallel to the normal of the production plane.

taken to be parallel to the normal of the production plane. The angle between the proton and the above defined axes is called θ_i , for $i = x, y, z$. The polarization vector \vec{P} then consists of the following components: P_x corresponds to the left-right asymmetry, P_y corresponds to the up-down (transverse) asymmetry and P_z to the forward-backward (longitudinal) asymmetry. The measurement of the transverse polarization and the longitudinal polarizations are the subject of this chapter. Angular momentum conservation in the Λ decay requires the distribution of the decay angle θ to be linear in $\cos \theta$. However due to detector effects the measured angular distribution can be changed. The angular distribution then will be of the form:

$$\frac{dN}{d \cos \theta_i} = \frac{1}{2} A(\cos \theta_i) [1 + \alpha P_i \cos \theta_i], \quad (8.3)$$

in which $A(\cos \theta_i)$ is the acceptance of the detector and P_i is the polarization in direction i .

The acceptance will have a large influence on the angular distributions, which can be seen for the NA57 data. Furthermore selection cuts will distort the distributions even more. The measured angular distributions with respect to the polarization axes for the period with the magnetic field up (negative polarity) are depicted in figure 8.2. The $\cos \theta_x$ distribution shows a drop around zero, which is due to the cut on the internal decay angle ϕ as explained in section 5.1.1. The transverse angular distribution ($\cos \theta_y$) is restricted to the negative region. This is due to the fact that in the V^0 selection only the cowboy decays are selected (see section 4.1). Most of these cowboy decays lie in a plane perpendicular to the magnetic field and since only the positive particle and one field polarity are regarded, this positive particle dominantly points in one direction. The area of the NA57 setup is only small and this implies that a Λ which is measured is always produced in a small polar angular range between of 48 and 97 mrad. This will define the production plane and its normal to have almost always the same orientation, with the normal perpendicular to the magnetic field. This makes that all protons are detected at one side of the angular spectrum for $\cos \theta_y$. Accordingly for the positive polarity this distribution is mirrored.

In the longitudinal distribution a gap around $\cos \theta_z \sim 0.25$ can be seen. This is due to the cut on the K_S^0 mass, applied in the V^0 selection (section 5.1.2). In the Podalanski-Armenteros plot this is roughly represented as a cut the Podalanski-Armenteros variable α , which is equivalent to

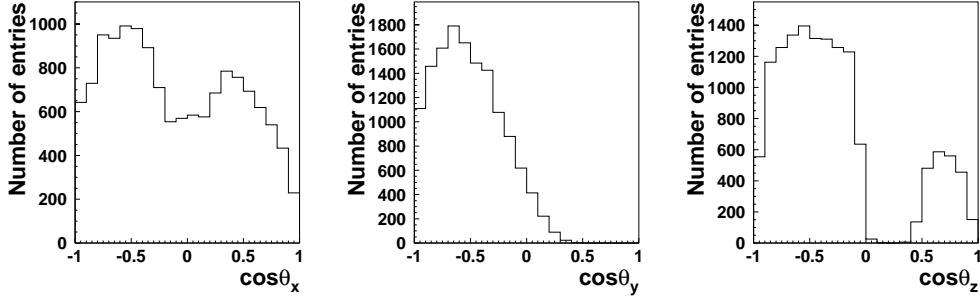


Figure 8.2: The measured angular distributions in all directions of the proton decaying from the Λ w.r.t. the three axes defined in figure 8.1.

a cut in $\cos \theta_z$ (see figure 5.5).

The measured angular distributions for the $\bar{\Lambda}$ are identical to the Λ spectra, except for the $\cos \theta_y$ distribution which is mirrored, due to the measurement of the anti-proton instead of the proton. The K_S^0 mesons have about the same decay topology as the Λ and therefore they also have a similar shape in the $\cos \theta_x$ and $\cos \theta_y$ distributions. For $\cos \theta_z$ however, it is different. The region, in which the K_S^0 mesons overlap with the Λ and $\bar{\Lambda}$ in the Podalanski-Armenteros plot, is near the edge of the distribution and the removal of the Λ and $\bar{\Lambda}$ background causes it to be empty there.

In order to correct for these distortions a deconvolution of the angular distributions is carried out. This is discussed in the next section.

8.1.2 Deconvolution

In this section the procedure used for deconvoluting the angular distributions is described. The description will be focussed on the Λ particles. However the conditions used for the K_S^0 particles are determined in a similar way.

Bin sizes

In section 7.1 the conditions for a deconvolution in m_T and y were described. It was seen that the bin size of the input distributions was determined by the resolution of the detectors and the statistics of the sample. In figure 8.3 the correlation between the generated and reconstructed angular distribution for all three coordinate directions is given for the generated Λ s.

The average resolution for all three directions is of the order of 0.1 in $\cos \theta$. Taking as the bin size about two times the resolution of the entries in the bin, this should give around 10 bins for each distribution. For the distorted $\cos \theta_y$ and $\cos \theta_z$ angular distributions of the experimental data unfortunately some parts of the range are empty, due to the selection cuts. This asks for the clustering of bins there. So for the deconvolution in $\cos \theta_y$ only 5 bins are used and for $\cos \theta_z$ 6. This decreases the number of bins, but this number should still be large enough to be able to reproduce the original distribution. Since the original angular distributions are linear the number of bins chosen is not critical and no loss of accuracy occurs.

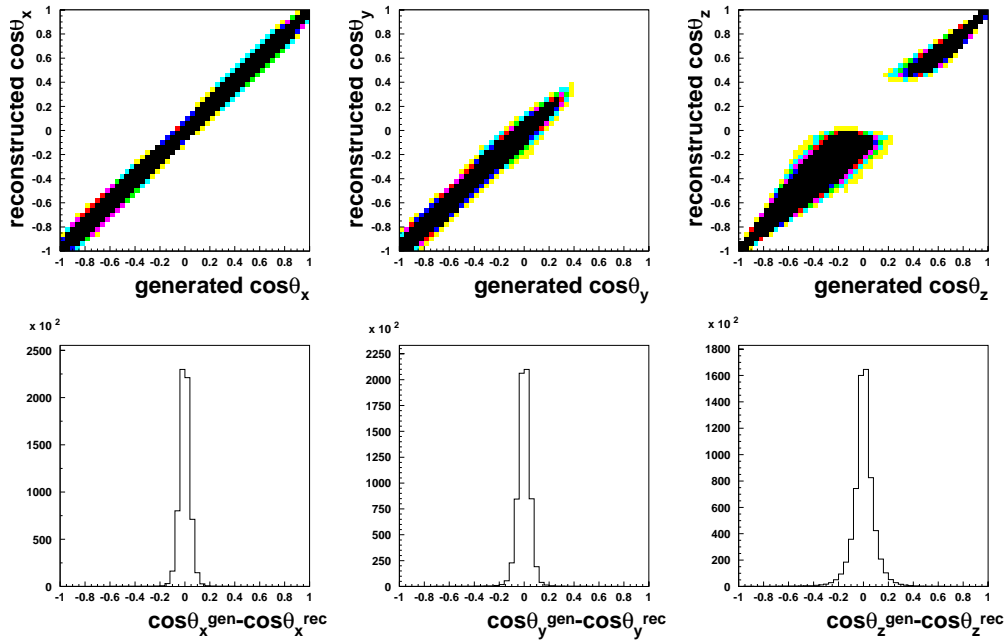


Figure 8.3: The correlation (top) and difference (bottom) between the generated and reconstructed values for the angular distributions of the decay proton.

A good choice of binning removes statistically insignificant contributions from the solution and oscillations can be avoided. In order to check this for each deconvolution solution the coefficients, rotated to the solution which has a covariance matrix equal to unity, should be larger than one. For each of the following results this check was made and all solutions were stable.

In section 8.3 the transverse and longitudinal polarizations are determined for the Λ and $\bar{\Lambda}$ particles. However, first the asymmetry of the K_S^0 decay measured by NA57 will be determined. Since no polarization is expected in the decay of the K_S^0 to two pions, this will determine the false asymmetry due to the geometry and knowledge of the detector setup, which is the dominant source of the systematic uncertainty.

8.2 K_S^0 polarization

The K_S^0 mesons are spin-less and have about the same decay topology as the Λ . Therefore they are a good tool to check biases introduced by detector effects and the reconstruction. First the transverse decay asymmetry is determined, whereafter the asymmetry in the longitudinal direction is investigated as well.

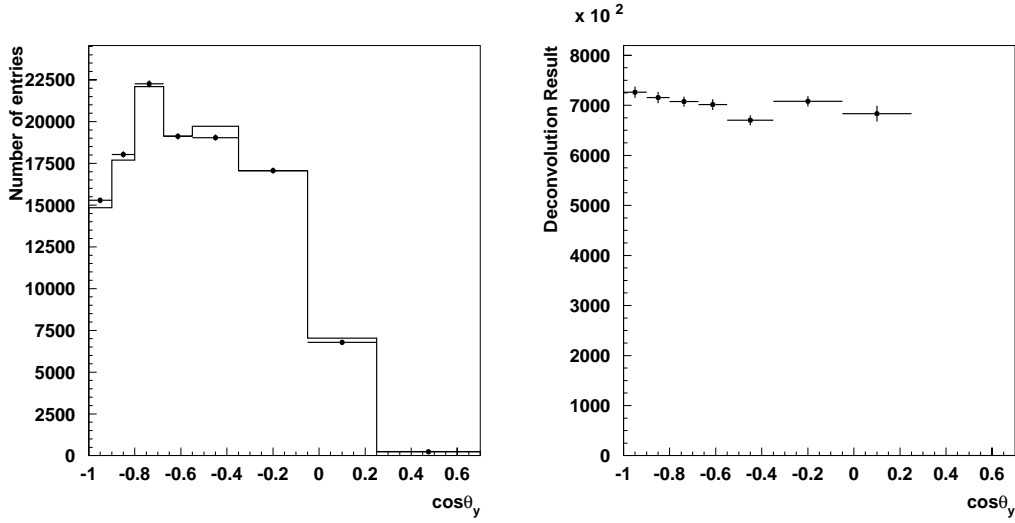


Figure 8.4: Comparison of the $\cos\theta_y$ distribution for data (solid circles) and simulations (histogram) (left) and the result of the deconvolution (right) for the K_S^0 . The deconvolution bin selected is: $1.1 < m_T < 1.25 \text{ GeV}/c$.

8.2.1 Transverse polarization

The transverse Λ polarization is known to be dependent on p_T and x_F . As a check the dependence of the transverse K_S^0 polarization on p_T has been determined. In order to investigate the polarization as function of p_T , a two-dimensional deconvolution in m_T and $\cos\theta_y$ was done. For the binning in m_T the binning used in the m_T - y deconvolution of last chapter was used. Only for values of high m_T , where the statistics is not large enough, some of the bins in that region have been combined. In figure 8.4 an example of the deconvolution for one m_T bin ($1.1 < m_T < 1.25 \text{ GeV}/c$) is depicted for the negative field polarity sample. To the left the (scaled) comparison between data (solid circles) and the simulations (histogram) is plotted and to the right the resultant deconvoluted distribution is given. It can be seen that the latter is asymmetric. The result for the whole p_T range is shown in figure 8.5, where the polarization as function of p_T is depicted for both field polarities. It can be seen that the polarization reaches large values for the low and high p_T region. Furthermore the asymmetries seen are seen to be opposite for the different field polarities. Such an asymmetry is also observed for the two other directions as can be seen in figure 8.6. In the left plot the longitudinal asymmetry and in the right-hand plot the left-right asymmetry are depicted. In both other directions asymmetries are found for the two magnetic field polarities, although for the left-right asymmetry direction this is less pronounced. These asymmetries could be due to the uncertainty of the position of the detectors in the experimental setup. This uncertainty could cause misalignments to occur in the reconstruction of the data, which could lead to over-steering effects seen already in section 4.2.3.

Therefore the transverse asymmetries found for the K_S^0 are considered as a systematic effect,

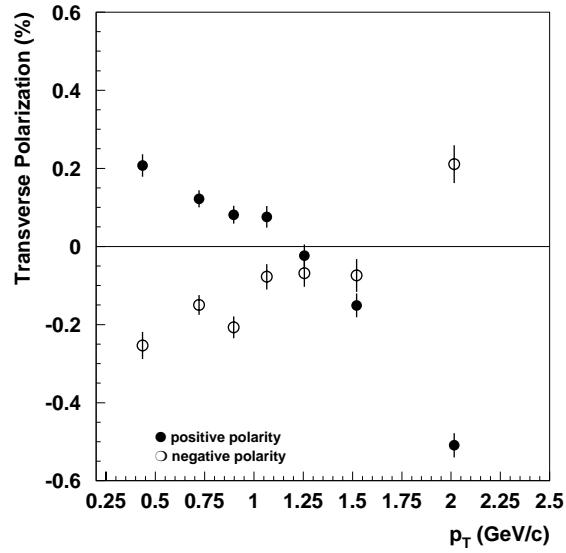


Figure 8.5: The dependence of the transverse polarization on p_T for the K_S^0 . The results for both the positive and negative field polarity are depicted.

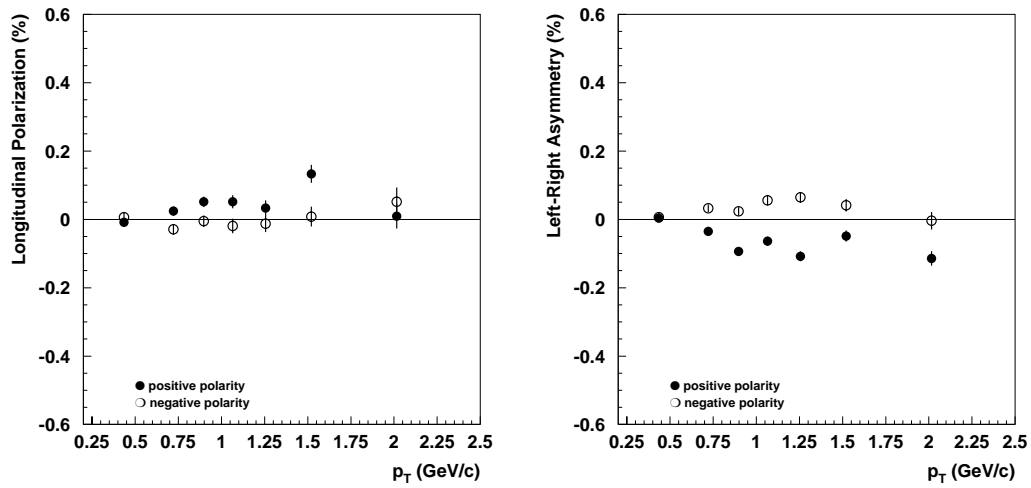


Figure 8.6: The longitudinal (left) and left-right (right) asymmetry versus p_T for the K_S^0 .

which must be taken into account when determining the transverse polarization of the Λ .

8.2.2 Longitudinal polarization

When the longitudinal polarization is determined for both field polarities combined, the result of the one-dimensional $\cos\theta_z$ deconvolution is plotted in figure 8.7. Also here an asymmetry is observed for the K_S^0 . The value found for the corresponding longitudinal K_S^0 polarization parameter P_z from a χ^2 fit of equation 8.3 amounts to: $P_z = 1.6 \pm 0.44\%$. Also here this value is taken as a systematic error in the calculation of the longitudinal Λ polarization.

8.3 Λ and $\bar{\Lambda}$ polarization

In the introduction (chapter 1) it was seen that the transverse polarization of the Λ has been measured to be dependent on p_T and x_F . In this section the dependence of the transverse Λ polarization on p_T and x_F will be investigated for the NA57 experiment. The dependence on x_F will be studied further by considering the influence of systematic effects on the result. Also the longitudinal polarization will be determined.

It was also seen that the transverse polarization of the $\bar{\Lambda}$ has been measured to be zero. In this

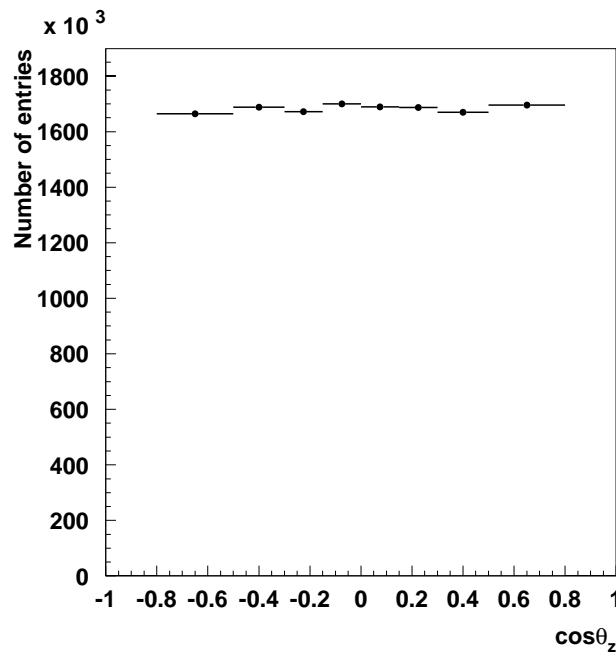


Figure 8.7: The result of the one-dimensional deconvolution in $\cos\theta_z$ for the K_S^0 . The data of both field polarity samples are used.

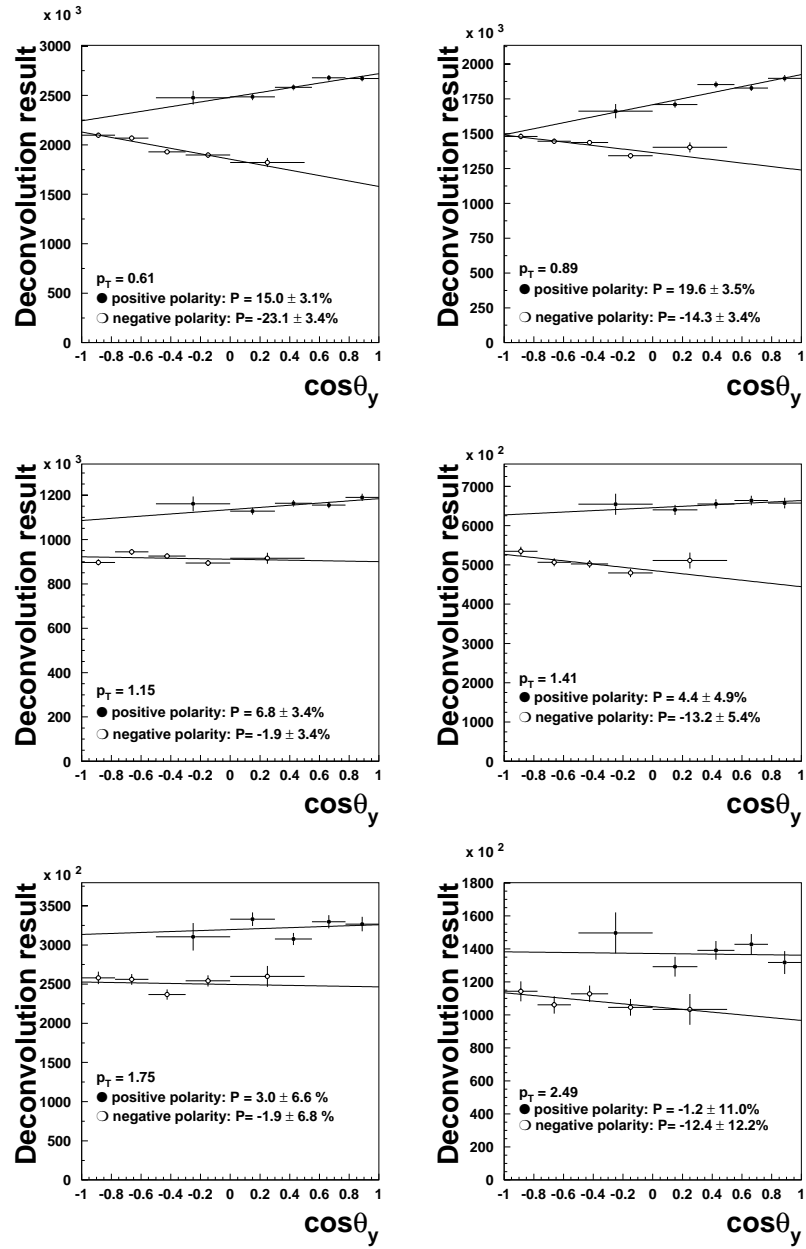


Figure 8.8: The results of the m_T - $\cos\theta_y$ deconvolution for each m_T bin. The corresponding average p_T value is given in the plot together with the results of the fit for the different field polarities.

thesis the dependence of the $\bar{\Lambda}$ polarization on x_F will be determined as well. A more detailed study was not possible due to the lower statistics.

8.3.1 Transverse polarization

P_T -dependence

In the study of the K_S^0 mesons, large polarization asymmetries were found as function of p_T . The same investigation has been done for the Λ . In figure 8.8 the result of the deconvolution is plotted for the various m_T -bins. For each bin deconvoluted result is shown for both field polarities, together with the results of the fit. An overview of the values found for each bin is given in figure 8.9, where the transverse polarization as a function of p_T has been plotted for the different field polarities. Analogously to the K_S^0 the polarization for different field polarities diverges towards lower p_T . However, at high p_T the measurements for the positive and negative field polarities agree within statistical errors. When considering the other angular distributions (longitudinal and left-right) no divergence between the field polarities occur (see figure 8.10). In order to get an indication of the influence of the uncertainty of the position of the detectors the following exercise has been considered. Simulations were run for both field polarities in which a misalignment of 2 cm was introduced for the lever arm. These simulations were then taken as input for the decon-

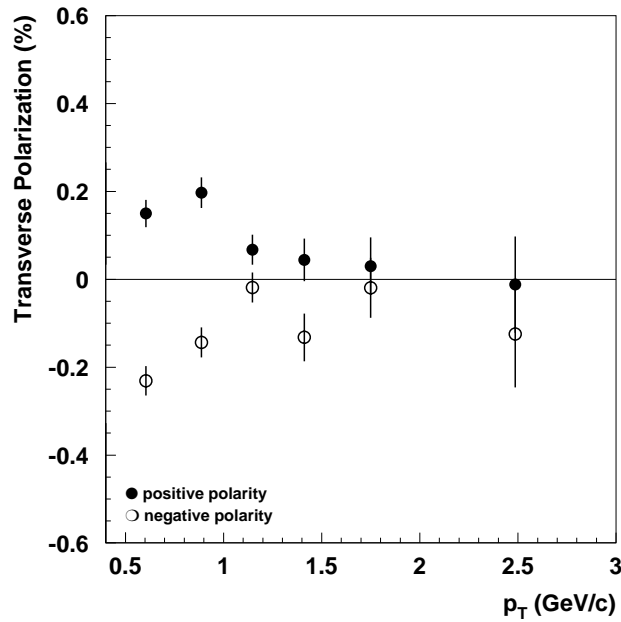


Figure 8.9: The dependence of the transverse polarization on p_T for the Λ . The results for both the positive and negative field polarity are depicted.

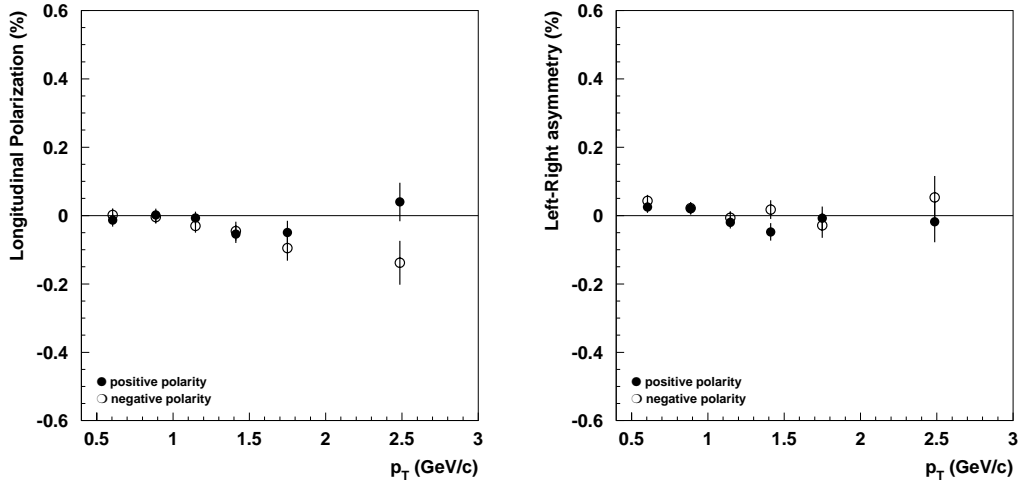


Figure 8.10: The longitudinal (left) and left-right (right) asymmetry versus p_T for the Λ .

volution. The result of this exercise is shown in figure 8.11. As for the data the results for both field polarities diverge, reaching asymmetries of about 30%. Considering the fact that these results are obtained with a shift of 2 cm on an extrapolation distance of 30 cm, a rough estimation of the value of the misalignment in the compact telescope, where the extrapolation distance is around 2 cm, would be of the order of hundreds of micron. This is indeed the uncertainty in the position of the pixel detectors. The influence of the detector geometry will be examined further in the section on the systematic errors.

x_F -dependence

In the introduction of this thesis it was seen that in p-p, p-A and A-A collisions for the region $p_T > 1$ GeV/c the transverse polarization only depends on x_F . The set of measured data shows that the transverse polarization increases almost linearly with x_F . At low x_F , in the region $0.1 < x_F < 0.2$, no data are available and a small value for the transverse polarization is predicted by semi-classical models. However on the magnitude of this value they disagree: the Berlin Model (section 2.2.2) predicts it to be as small as -2%, while the Thomas Precession model and the Troshin-Tyurin model predict the transverse polarization to reach a value of -5 and -8% respectively. NA57 is able to measure in this x_F range and therefore it is interesting to study the dependence of the transverse Λ polarization on x_F .

The x_F dependence of the transverse polarization has been determined by doing a deconvolution in y and $\cos\theta_y$. The choice for the deconvolution in rapidity and not directly in x_F is because the generation of Λ hyperons in a flat distribution has been successful for data correction, e.g. for determining the inverse slopes. Therefore it is convenient also in the bin size definition to start from the binning used in the y - m_T deconvolution. Since the transverse polarization reaches its maximum value for $p_T > 1$ GeV/c, it is interesting to consider only this region. This also makes it possible to compare the results with the world data (shown in fig 1.3). The results of the y

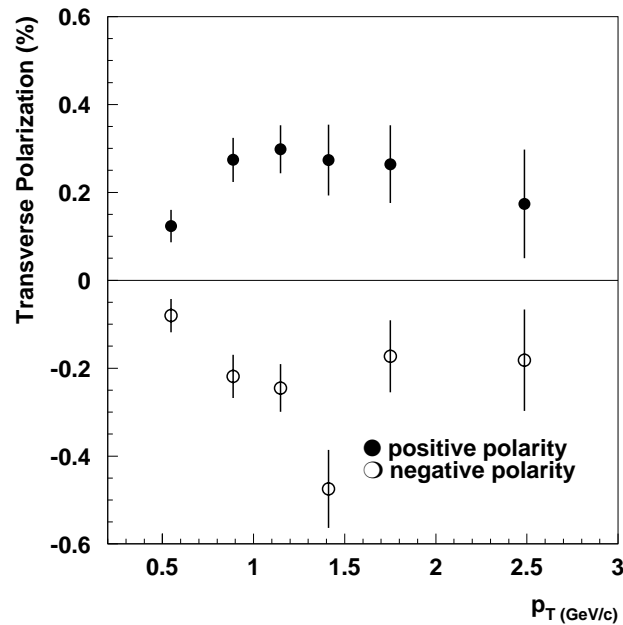


Figure 8.11: The dependence of the transverse polarization on p_T for simulations in which the lever arm has been shifted 2 cm. The results for both the positive and negative field polarity are depicted.

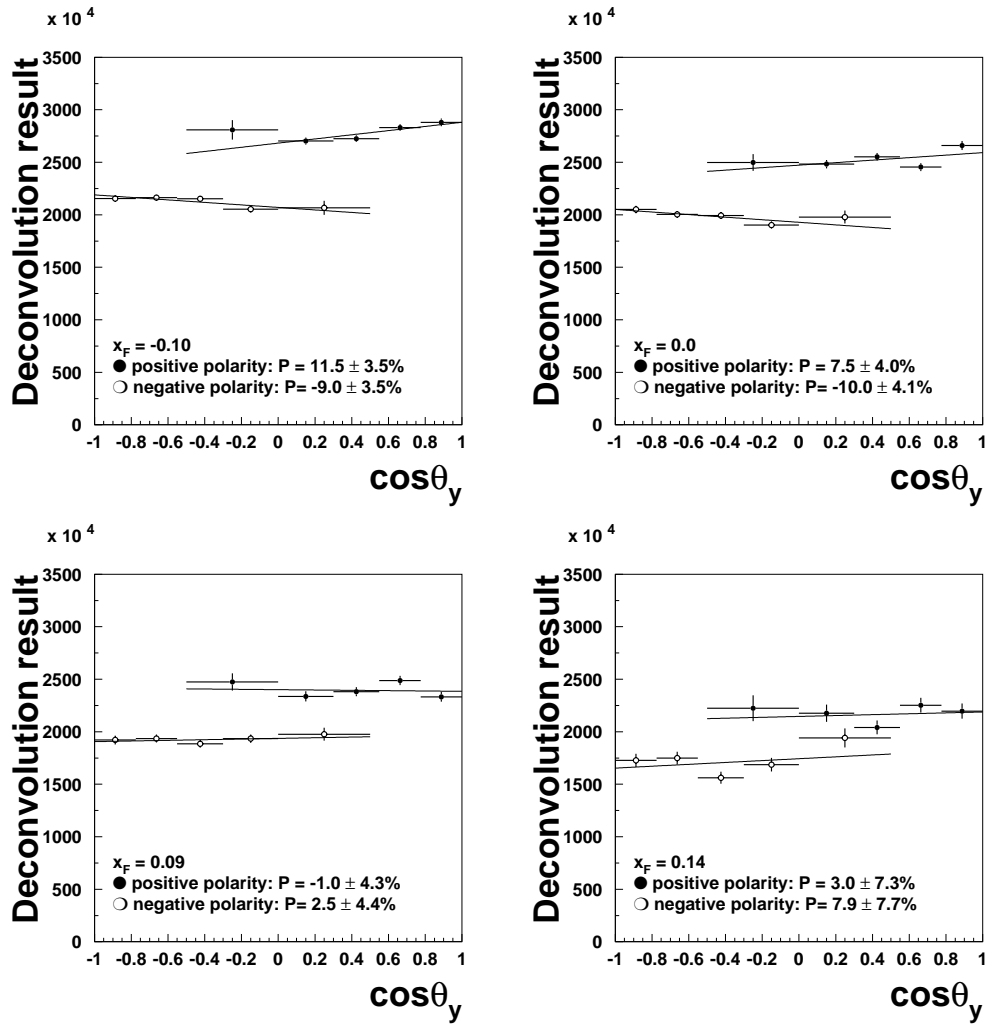


Figure 8.12: The results of the y - $\cos\theta_y$ deconvolution for four rapidity bins. The corresponding average x_F value is given in the plot together with the results of the fit for the different field polarities.

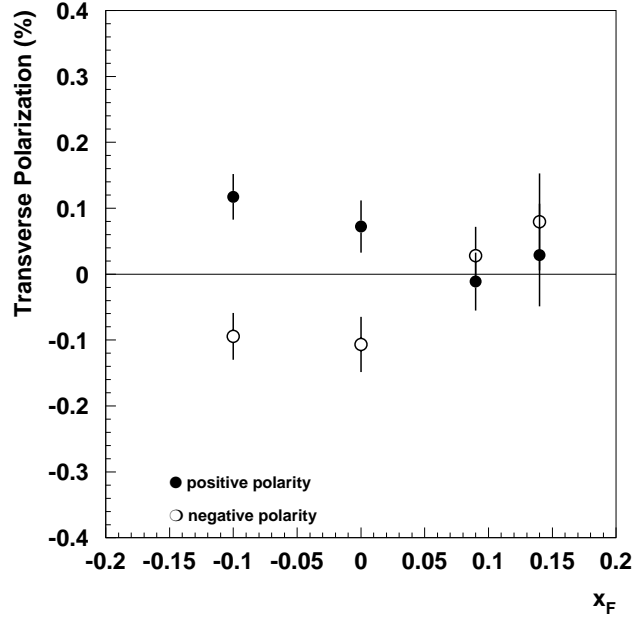


Figure 8.13: Dependence of the transverse polarization of the Λ on x_F .

and $\cos\theta_y$ deconvolution with the requirement $p_T > 1$ GeV/c for four rapidity bins is shown in figure 8.12, where the values for x_F are taken to be the average x_F in the corresponding rapidity bin. The results of the fit are depicted in figure 8.13, where the polarization as a function of x_F is

Table 8.1: Values of the transverse Λ polarization for $x_F > 0$. The results for the positive and negative field polarity are given separately. The errors are only statistical where the first is the statistical error introduced by the data the second by the response matrix uncertainty.

Polarity	N_Λ	$\langle x_F \rangle$	$\langle p_T \rangle$	Transverse polarization
Negative	19984	0.09	1.49	$2.5 \pm 4.4 \pm 2.2$
	6251	0.14	1.70	$7.9 \pm 7.3 \pm 3.2$
Positive	22202	0.09	1.49	$-1.0 \pm 4.3 \pm 1.9$
	7175	0.14	1.70	$3.0 \pm 7.7 \pm 3.9$

plotted. There still exists some asymmetry at $x_F \leq 0$, due to the contribution from the lower p_T Λ s. However the effect is already suppressed and the asymmetry only reaches values of around 10%. At positive x_F the results for positive and negative polarity converge and therefore only these points will be considered further on. The transverse polarization found for the two positive values of x_F for this region are given in table 8.1.

For the measurements at $x_F = 0.09$ and 0.14 also the p_T dependence can be considered. This is shown in the left plot of figure 8.14. There is no significant polarization with respect to p_T . Hence there is no indication that the polarization is increased at low p_T due to the transverse momentum shift introduced by multiple scattering in the nuclear medium [36]. In the right side of plot 8.14 also the dependence on the centrality of the sample is shown, where the sample is divided in two subsamples:

- 1 Central: 0-15 % most central collisions. This sample corresponds to bin (III) and (IV) of centrality definition used in NA57.
- 2 Peripheral: 16-60 % most central collisions. This sample corresponds to bin (0)-(II).

A division in the 5 bins defined by NA57 was not possible due to the limited statistics for deconvolution. Also here no significant difference in polarization for the different centrality samples can be seen.

$\bar{\Lambda}$ polarization

The analysis of the $\bar{\Lambda}$ polarization is identical to the Λ analysis. The transverse asymmetries seen for the Λ are also seen here. The dependence on x_F is plotted in figure 8.15 together with data for

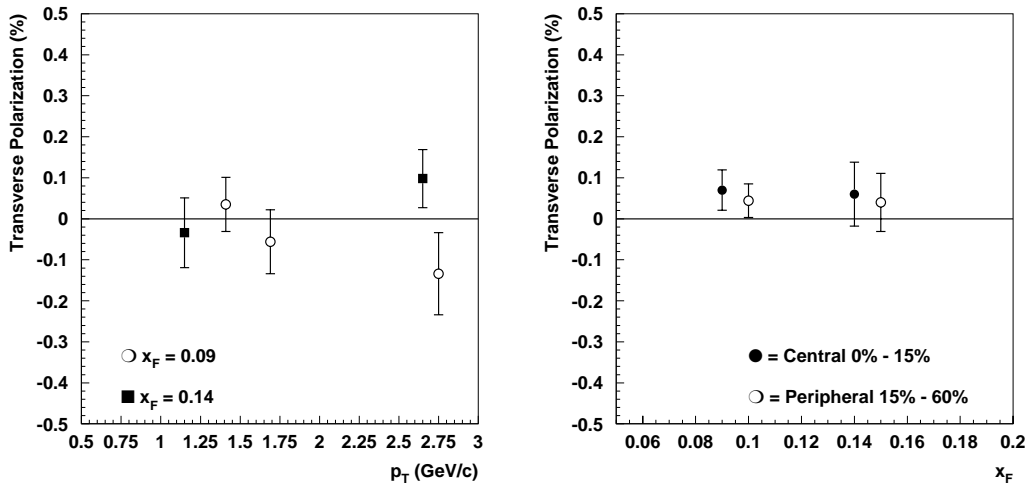


Figure 8.14: Dependence of the transverse Λ polarization on p_T for the two different x_f data points (left) and centrality (right)

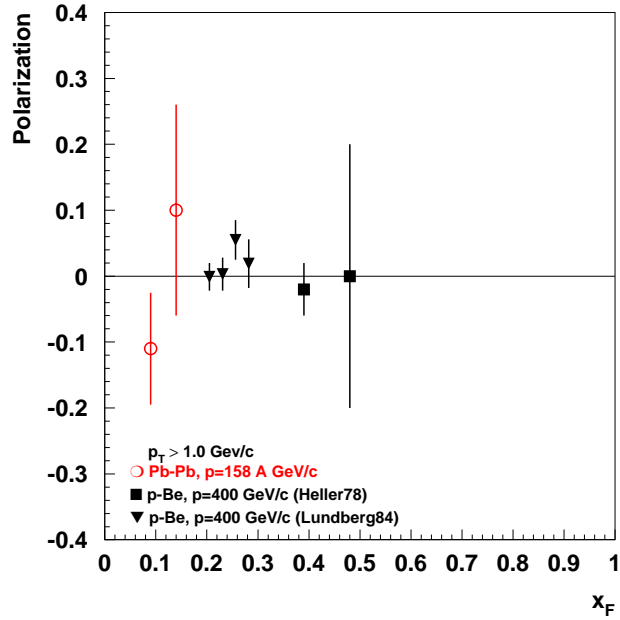


Figure 8.15: Transverse $\bar{\Lambda}$ polarization compared with results for p -Be collisions at 400 GeV/c

p -Be collisions of 400 GeV/c. The values of the $\bar{\Lambda}$ polarization are consistent with zero. This is expected in the scope of the semi-classical models where the remnants of the incoming projectile are crucial for the transverse polarization. The $\bar{\Lambda}$ is created from quarks from the sea and therefore there is no production plane with respect to which the $\bar{\Lambda}$ can be polarized. Since the statistics is lower for the $\bar{\Lambda}$ a more detailed study has not been performed.

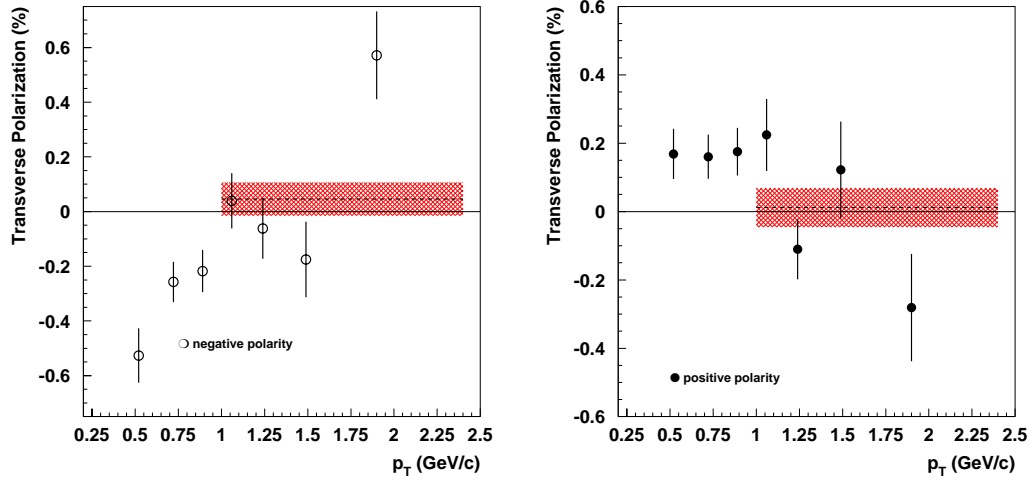


Figure 8.16: Dependence of transverse K_S^0 polarization on p_T for the negative polarity sample (left) and the positive sample (right) for the case $\cos\theta_z > 0.5$. The dashed line gives the value found for the combined region of $p_T > 1.0$ GeV/c and the shaded error is its statistical error.

8.3.2 Systematic effects

In this section the influence of systematic effects on the transverse polarization of the Λ is investigated. This will be done for the region $x_F > 0$. Systematic effects have been estimated to occur for the following cases:

- Error estimated from the K_S^0 asymmetry.
- Definition of the Region-of-good-acceptance.
- Dependence of run period
- Selection cuts
- Chip efficiency
- Feed down

These effects will be described sequentially and their influence is shown. Finally an estimation of the size of these effects on the final result is given.

Error estimated from K_S^0 asymmetry

It was shown that the divergence of the transverse polarization at low p_T was also seen for the K_S^0 . Contrary to the Λ at high p_T the transverse polarization for both field polarities diverged again but

in the opposite direction as for low p_T . This is an important measure of the limitations of the NA57 experiment to determine the transverse polarization. This behavior is considered as a systematic effect due to the uncertainty of the position of the detectors and the resulting misalignments in the reconstruction. In order to take the effect into account for the Λ , it is important to keep in mind that the decay of the K_S^0 is different from the Λ . The Λ decays in a proton and a pion where the proton gets the largest momentum with an average value of 11.4 GeV/c. The pion has a lower average momentum of 2.5 GeV/c. The K_S^0 decay is symmetric, where each pion has an average of around 6.2 GeV/c. In order to have the same acceptance for the K_S^0 and the Λ , those decays of the K_S^0 where the positive pion is faster than the negative pion have to be selected. Therefore the criterium $\cos\theta_z > 0.5$ has been set. This gives a sample of K_S^0 where the positive pion has an average momentum of 9.5 GeV/c and where the negative pion momentum average is 3.0 GeV/c. These values are compatible with the Λ decay momentum values. Furthermore a similar region-of-good-acceptance used for the Λ is taken for the K_S^0 . The p_T dependence of the transverse polarization of the K_S^0 for $\cos\theta_z > 0.5$ is shown in figure 8.16. In this figure on the left only the case for the positive polarity data is shown and on the right the negative polarity plot is given. By selecting only the K_S^0 with the decay characteristics comparable with the Λ also the p_T distributions are similar. Since for the measurements done for the Λ at $x_F > 0$ are taken in the region $p_T > 1$ GeV/c, this same region has to be considered for the K_S^0 . When the transverse asymmetry of the K_S^0 in the region $p_T > 1$ GeV/c is determined the values are +4.6% for the negative field polarity and +1.2% for the positive field polarity. These errors estimated from the K_S^0 asymmetry are depicted in figure 8.16 by the dashed line and its error by the shaded area.

Region-of-good-acceptance

In the above the error estimated from the K_S^0 false asymmetry was studied. This error determines the systematic error due the sensitivity of the K_S^0 polarization on the detector geometry and accordingly about the sensitivity of the transverse Λ polarization on this geometry. In order to prevent geometry related effects a region-of-good-acceptance was defined. Therefore it is also important to check the influence of the definition of this region-of-good-acceptance (as defined in section 7.2) on the transverse polarization for the Λ .

The first effect which has been studied is the definition of the last rapidity bin. Since it is intended to measure up to the highest possible x_F value, the upper limit of the highest rapidity bin has not been chosen to be the same as the limit taken in the definition of the region-of-good acceptance for the inverse slopes and yields. In figure 8.17 this upper limit has been varied in order to check whether this introduces a systematic effect. In the plot the dependence of the transverse polarization on the variation of the upper limit measured for both field polarities is shown. The vertical dashed line indicates the default value of the variable investigated. The horizontal line is the value of the transverse polarization found for this default choice while the shaded band indicates the statistical error contributed by the data. Just as for the error derived from the K_S^0 false asymmetry, the systematic errors found for the different field polarities are regarded as independent contributions to the total systematic error. It can be seen that the variation of the highest bin limit does not introduce large systematics effects. Only for the positive field polarity the lowest chosen upper limit seems to deviate. It is important to keep in mind that by lowering the upper limit the bin size is also decreased. This implies that the sample used has smaller statistics and is only a subset of

the sample used as default. Therefore the result can show a statistical deviation with respect to the larger statistics sample result. This has to be kept in mind when estimating the systematic error.

The next cut used in the definition of the region of good acceptance is the cut on p_T . Since the m_T distribution is asymmetric the minimum and maximum allowed values of p_T have been varied individually. Since the transverse polarization has been measured to be independent on p_T in the interval $p_T > 1$ GeV/c it is interesting to see how the variation of the minimum value of p_T affects the transverse polarization (see figure 8.18). On the left the result for $x_F=0.09$ is depicted where on the right the variation for $x_F=0.14$ is plotted. Note that it is assumed in the following that for $p_T > 1$ GeV/c the transverse polarization does not depend on p_T . It is interesting to see that the transverse polarization determined with the negative field polarity is more sensitive to this cut than the positive field polarity result. This is the most pronounced for the lower x_F point, where the transverse polarization reaches a value of -20% at $p_T^{min}=1.6$ GeV/c. However, this value is obtained with a smaller subset of the default sample and therefore it could be a statistical fluctuation. Therefore the statistical error of the point has been taken into account in determining the systematic error, which is hence estimated to be 10%, amounting to a 5% error on the combined

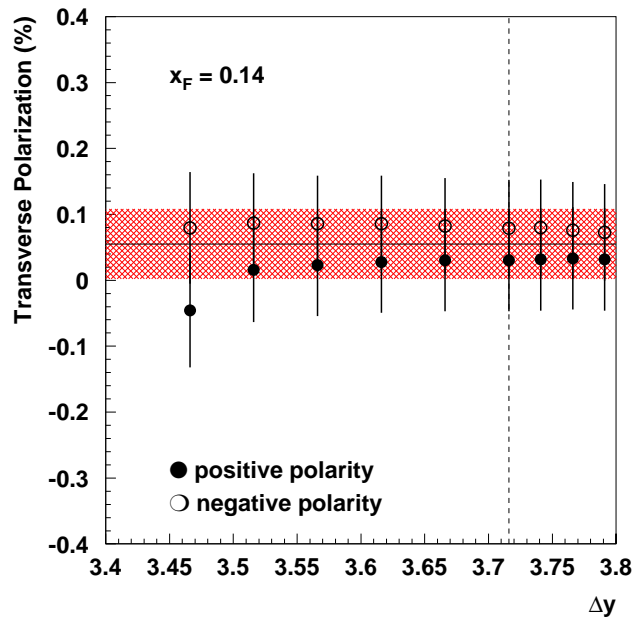


Figure 8.17: Transverse Λ polarization as function of the cut on the upper limit of the highest rapidity bin. The dashed vertical line shows the cut which has been used and the horizontal line renders the value found for this case. The shaded band indicates the statistical error (from the data contribution only).

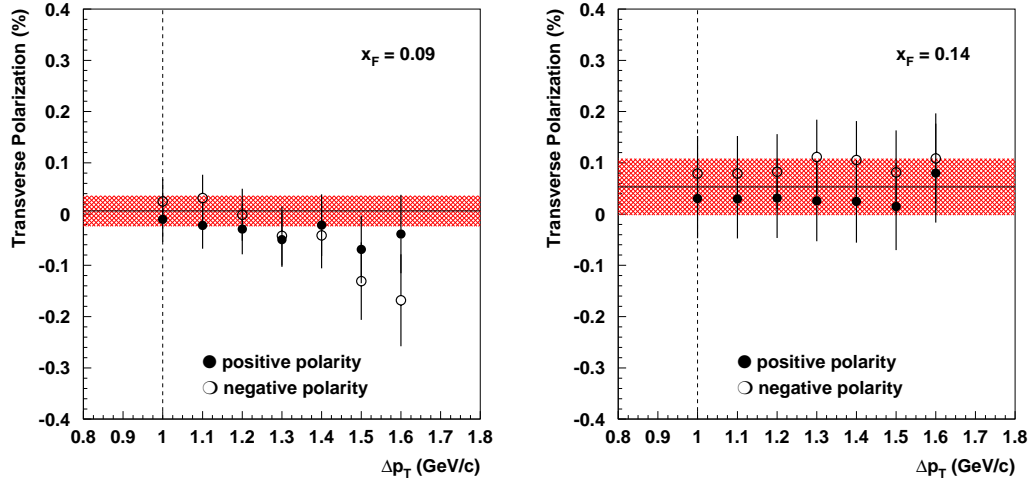


Figure 8.18: Transverse Λ polarization as function of the cut on the minimum p_T .

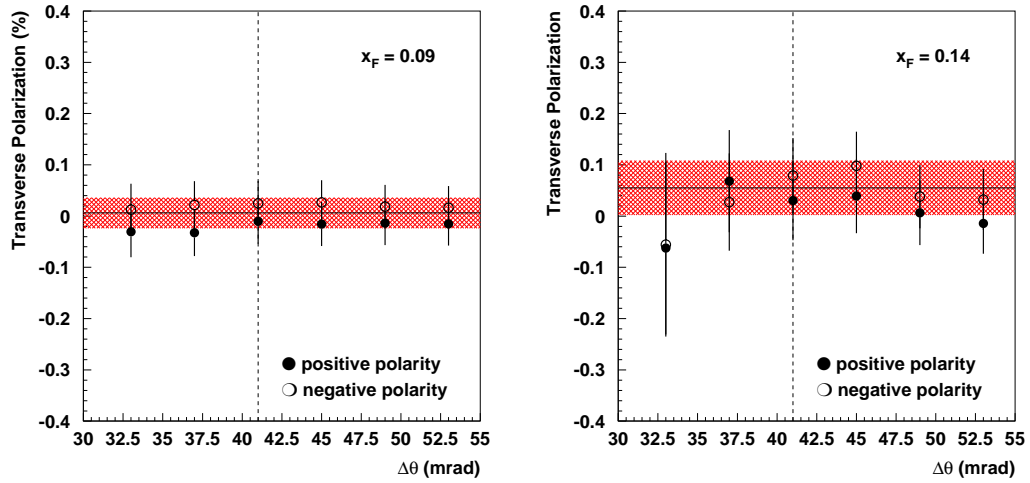


Figure 8.19: Transverse Λ polarization as function of the cut on the angle between Λ and beam axis.

result. The variation of the maximum value of p_T shows no systematic effect.

The variation of the cut on θ was done by changing the window at both sides simultaneously with 2 mrad. This is depicted in figure 8.19. For the lower x_F point the effect is marginal while for the higher point only the smallest window shows a large deviation, which however has a large statistical error and is consistent with the default result.

Dependence on run period

During data taking experimental conditions can change and this can influence the measurements. In order to study this effect the run period was divided in 9 periods. These periods were defined by considering the runs of two consecutive background files. In this way periods with a different detector performance could be selected. The dependence of the transverse polarization on the run period can be seen in figure 8.20. For both x_F points the dependence follows statistical fluctuations and no systematic effect can be seen.

K_S^0 mass cut

The largest part of the background of K_S^0 in the Λ sample has been removed by applying an asymmetric cut on the invariant mass of the reconstructed V^0 . In figure 8.21 the influence of this mass cut on the transverse polarization has been investigated. In this plot the variation of the mass cut is denoted by the upper boundary of the asymmetric mass cut: the value used in the analysis is $34 \text{ MeV}/c^2$ and this is changed by $7 \text{ MeV}/c^2$ for each step. For the lower boundary the default value

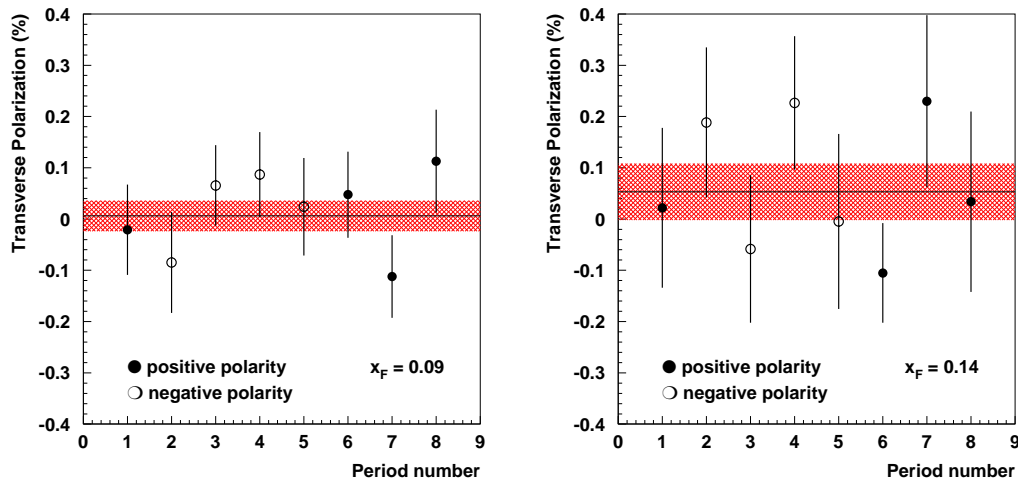


Figure 8.20: Transverse Λ polarization as function of run-period

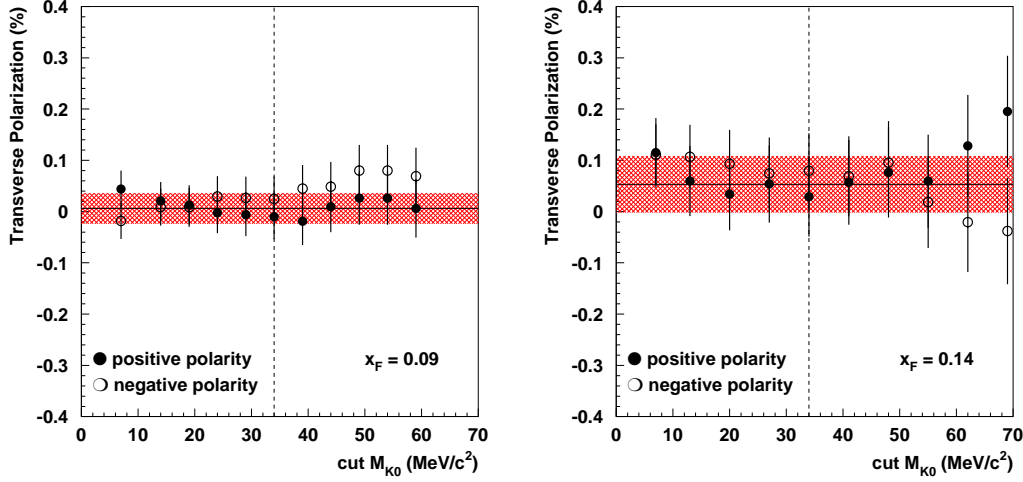


Figure 8.21: Transverse Λ polarization as function of K_S^0 invariant mass cut

was $26 \text{ MeV}/c^2$ and the step size was $5 \text{ MeV}/c^2$ which was changed simultaneously with the upper boundary variation. In this way the number of K_S^0 mesons in the sample is increased gradually and its effect on the transverse polarization can be studied. It can be seen that the dependence of the transverse polarization on the mass cut is not insignificant. For the case $x_F = 0.09$ both polarities show a systematic effect to the positive side of around 3-4 % for the combined result. For $x_F = 0.14$ also some clear systematic effects can be seen when increasing the mass cut to $70 \text{ MeV}/c^2$ or when applying no mass cut at all. These are estimated at most to be of the order of -3% for negative polarity and +3% for the positive polarity.

Chip efficiency

The Λ decaying from the Ξ has a longitudinal polarization of around 29% (see section 2.3.2). It was shown that this value could be retrieved in the NA57 experiment but only when applying the cut $\cos\theta_z > -0.5$ [74]. This cut was introduced because for the protons, pointing backward in the decay, the detection efficiency is different between simulations and data. This is due to the fact that in the simulations efficiencies of a chip are stored globally, while in the experimental setup the efficiencies of the chip are lower at the edge of the chip. In case the proton is directed backward in the center of mass of the Λ , the opening angle between proton and pion in the laboratory frame is small. This V^0 decay then has the probability to have both the decay products reaching one chip and to be both hitting the chips at the edge. This will reduce the detection probability for the data Λ with respect to the simulations. Since this introduces an error of about 3% on the yields this is considered as a small effect for which no correction is made.

In order to investigate the influence of this effect on the transverse polarization measurement,

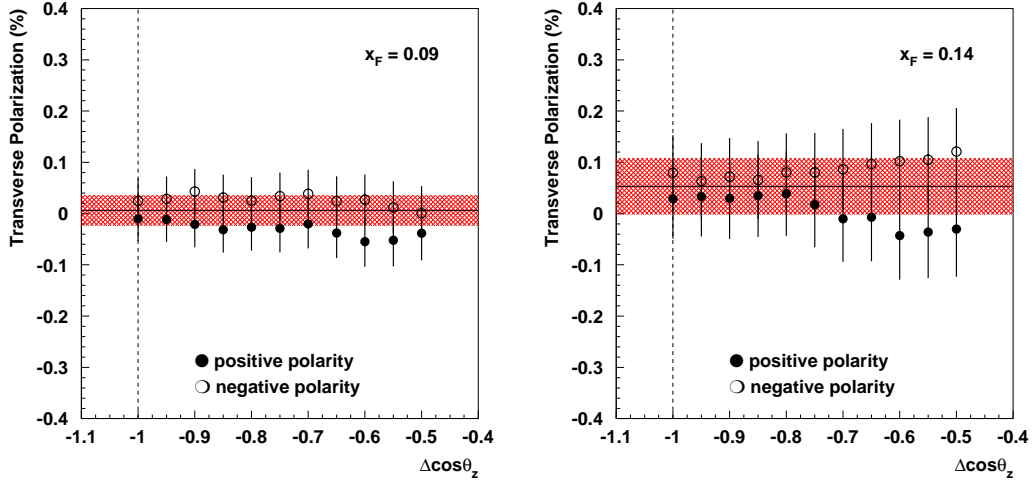


Figure 8.22: Transverse Λ polarization as function of the cut on $\cos\theta_z$.

a variation of the cut on $\cos\theta_z$ has been checked. For $x_F = 0.09$ no large effect is visible and the positive polarity sample is estimated to show a systematic shift of -1.5%. The results for both polarities tend to diverge a little for $x_F = 0.14$ and this has to be taken into account: +1% for the negative polarity sample and -1.5% for the positive polarity.

Feed-down

In NA57 the sample of Λ s measured is not corrected for the feed-down from decays of heavier hyperons like the Ξ , Ω and Σ . The WA97 experiment, which has measured for the same energy and system, has shown that the effect of the feed-down is less than 5% for the Ξ and Ω . Since the setup of NA57 is similar it is reasonable to assume the same influence of the feed-down here. The effect of this on the transverse polarization then would also be of the order of 5% of the measured value of the polarization, which is negligible with respect to the statistical and systematic error. The situation is different for the Σ which has been measured to have a positive transverse polarization of the same order as for the Λ [8]. This would decrease the transverse polarization by the fraction of Λ s coming from the Σ decay. The feed-down originating from this decay is not known in NA57, but it is estimated to be of the order of 20-30% [3]. For the case $x_F = 0.09$ this effect is only 0.3%, while for $x_F = 0.14$ this then would yield a increase of the value of the transverse polarization of about 2.3%.

Overview of the systematic errors

In the study above the following systematic effects have been investigated: the influence of the definition of the region-of-good-acceptance, the K_S^0 mass cut, the dependence of the data taking period, the chip efficiency discrepancy between simulations and data, the feed-down from other particles and the error estimated due to the K_S^0 false asymmetry. The estimation of the total systematic error has been done in the following way: the error introduced by the K_S^0 false asymmetry gives the influence of the detector geometry. The same influence however is studied by the variation of the definition of the region-of-good-acceptance. Hence it is expected that the systematic errors found for these studies are correlated. Therefore the largest error from these two contributions is taken. The resulting error is then added quadratically to the other errors, where the contributions of the different field polarities have been considered as separate entries.

The estimation of the errors introduced by these systematic effects is $^{+6.6}_{-5.6}\%$ for the data point at $x_F = 0.09$ and $^{+6.6}_{-4.4}\%$ for $x_F = 0.14$. The breakdown of these errors for the different effects is given in table 8.2.

Table 8.2: Systematic errors of the transverse Λ polarization for the positive and negative field polarity separately. The sources of the systematic errors are the K_S^0 false asymmetry error ($E_{K_S^0}$), the definition of the region-of-good-acceptance (Δy , Δp_T^{min} , $\Delta\theta$), K_S^0 mass cut $\Delta M_{K_S^0}$, chip efficiency influence $\Delta\cos\theta_z$ and Σ feed-down (Σ F-D). Also the result for the transverse polarization with the total statistical and systematic error is given.

$\langle x_F \rangle$	Polarity	$E_{K_S^0}$	Δy	Δp_T^{min}	$\Delta\theta$	$\Delta M_{K_S^0}$	$\Delta\cos\theta_z$	Σ F-D	P_{trans}
0.09	Negative	+4.6	-	+0.0 -5.0	+0.0 -0.0	+3.5 -1.0	+0.5 -0.5	+0.3	$0.6 \pm 3.4 \pm ^{+6.6}_{-5.6}$
	Positive	+1.2	-	+0.0 -1.0	+0.0 -0.5	+3.0 -0.3	+0.0 -1.5	-0.0	
0.14	Negative	+4.6	+0.0 -0.0	+0.5 -2.0	+1.0 -0.0	+1.3 -3.0	+1.0 -0.5	+2.3	$5.5 \pm 6.0 \pm ^{+6.6}_{-4.4}$
	Positive	+1.2	+0.0 -1.5	+1.0 -1.3	+2.0 -0.3	+3.0 -0.0	+0.5 -1.5	-0.0	

8.3.3 Longitudinal polarization

The longitudinal polarization has been determined by doing a one-dimensional $\cos\theta_z$ deconvolution, where the sample used was the combined statistics of the positive and negative field polarity. The corrected angular distributions for the Λ and $\bar{\Lambda}$ are depicted in figure 8.23. It can be seen that the shape is the same for the Λ and $\bar{\Lambda}$ distributions. For both in the region where the K_S^0 background has been removed still a peak can be seen. Since the simulated sample contains no K_S^0 this could be due to experimentally unremoved K_S^0 mesons. In order to determine the influence of the cut on the K_S^0 invariant mass, this cut has been varied and the resultant longitudinal polarization has been determined. This is seen in the right plot of figure 8.24, where on the left-hand plot the corrected distribution with no invariant K_S^0 mass cut is rendered. It is clear that the choice of the mass cut is critical for the obtained result. Next to this also the chip efficiency effect mentioned in the study of systematic effect of the last section must be taken into account. The drop of the

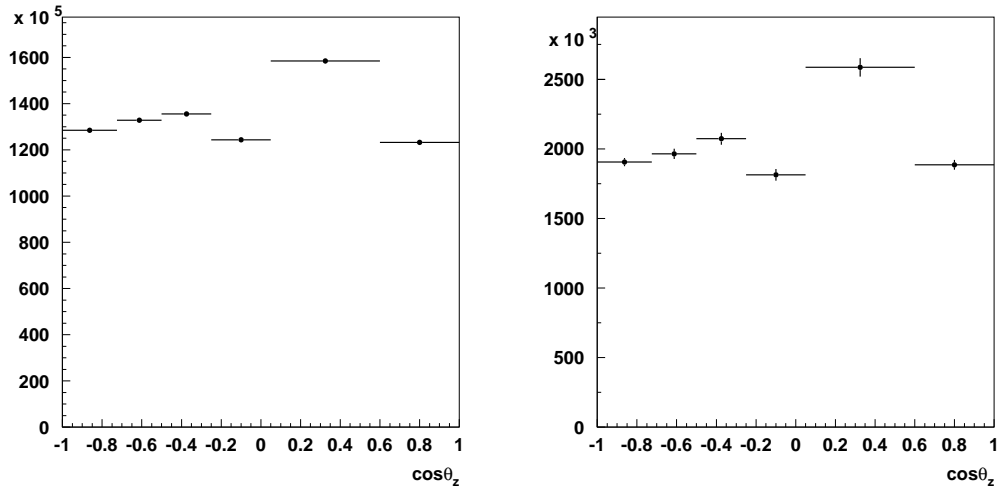


Figure 8.23: Deconvolution result of the longitudinal polarization for the Λ (left) and $\bar{\Lambda}$ (right).

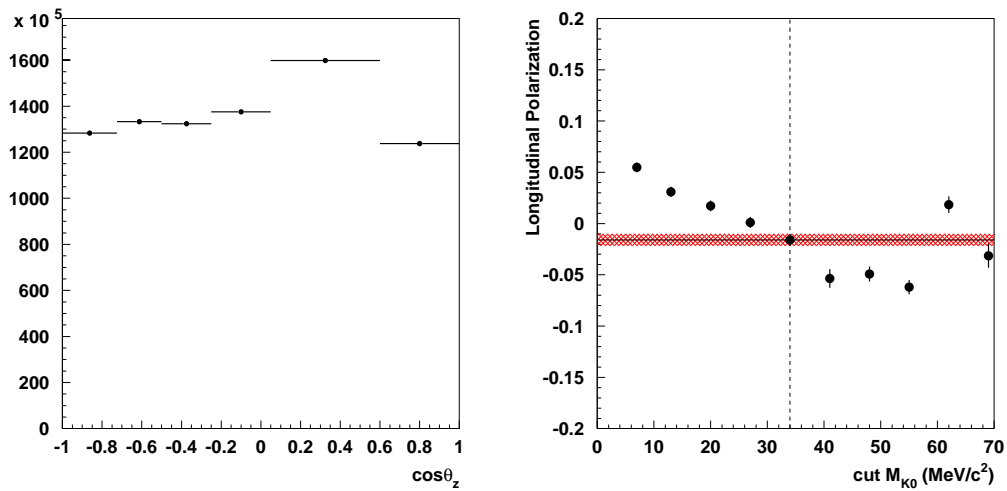


Figure 8.24: Deconvolution results of the longitudinal polarization for the Λ when no K_S^0 mass cut has been applied (left) and the longitudinal polarization as function of the variation of the K_S^0 mass cut (right). The vertical line indicates the mass cut used in the Λ analysis. The horizontal line and band gives the corresponding result and its statistical error.

chip efficiency at its edges, has been shown to cause Λ s with the proton decaying in the backward direction to have a lower probability to be detected. This should cause the corrected angular distribution to show a drop in the region of $\cos\theta_z < -0.5$. This effect indeed can be seen in the deconvoluted angular distribution of the Λ , but it is not clear in what respect this region is also influenced by the K_S^0 mass cut. Furthermore the resolution is such that an increase of the number of bins in that region could cause the result to be unstable.

Taking into account the above mentioned effects, the longitudinal polarization can not be determined very well. It is dominated by systematic effects which are difficult to remove in this setup.

8.4 Conclusion

When the statistical and systematic effects are taken into account the result of the transverse polarization is depicted in figure 8.25. This shows that NA57 is able to measure down to the region $0.1 < x_F < 0.15$. In this region the different semi-classical models predict different values: the DeGrand-Mietinen model predicts a value of -7% for the transverse polarization in this region, while the Turyin-Troshin model estimates it to be around -5%. The Berlin model predicts that the

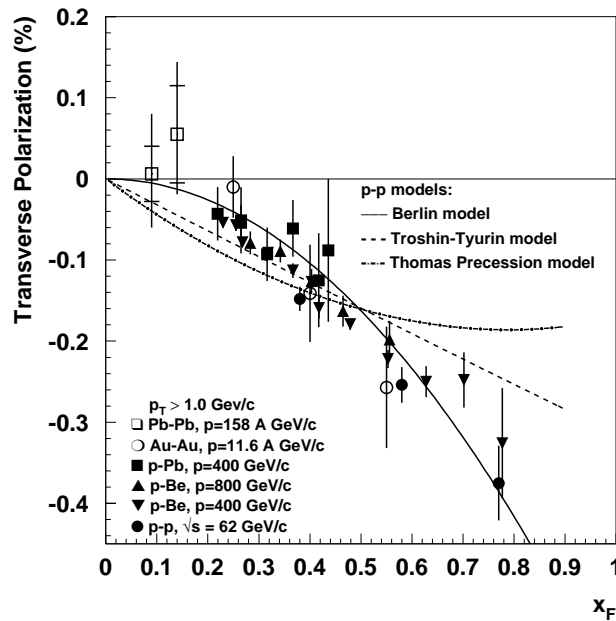


Figure 8.25: The transverse Λ polarization measured in this thesis compared with the results from other experiments. The error given is the combined error, where the horizontal lines indicate the statistical errors only.

value of the transverse polarization is close to 0%. The measurement of NA57 at $x_F = 0.14$ has a value of $+5.5^{+8.9}_{-7.4}\%$. This result is compatible with zero polarization in this region and seems to favor the Berlin model. However the error is unfortunately too large to exclude one of the models. The available statistics for this region makes it also impossible to see a clear dependence on p_T and the centrality of the collisions. The latter study shows there is no dependence on the interaction size of the collision. The zero polarization measured could in principle indicate the creation of a QGP but the error is too large to exclude a small polarization at this region which could prove the contrary. Also the longitudinal polarization of the Λ is dominated by systematic effects like dropping chip efficiencies at the edges and the K_S^0 background. Therefore the longitudinal polarization could not be determined with the method employed here.

The investigation of the K_S^0 false asymmetry shows that a study of polarization effects by the NA57 is extremely sensitive to the uncertainty of the detector geometry. Despite the systematic effects due to the detector geometry it was possible to measure the transverse Λ polarization with a precision of about 9%. The contributions of the statistical and the systematic error to the total error are of the same order. Since the NA57 experiment has taken a second data taking run in 2000 for Pb-Pb collisions at 158 AGeV/c, it is possible to reduce the statistical error. Due to the fact that the statistics of the Pb2000 run was the same as for the Pb1998 run this could reduce the statistical error with a factor of $\sqrt{2}$. Furthermore it is interesting to see to what respect the detector geometry contributes to the systematic error for this run.

In addition to the data taken at 158 AGeV/c, also data have been taken at an energy of 40 AGeV/c. An investigation of the transverse polarization of the Λ s produced in Pb-Pb collisions at this energy not only would give results at the same values of x_F as for the higher energy runs, it also would make it possible to measure up to $x_F \sim 0.35$. In this region the models predict the polarization to be of the order of 10-15%. With a more precise determination of the alignment of the detectors the dominant systematic errors due to detector geometry could be reduced and a measurement in this region could yield a significant polarization result.

Furthermore the investigation of the transverse polarization of Λ produced in p-Be collisions at 40 AGeV/c would make it possible to compare results taken for different collision systems. In this way the influence of the size of the system on the the transverse polarization could be investigated.

A

Appendix

Telescope configurations

In this thesis the data of three lead runs have been used. The detector configurations for all three periods are shown in figures A.1- A.3. In the setup of Pb1998 there were 9 pixel planes in the compact telescope and 4 pixel planes in the lever arm. Furthermore there were 4 double-sided micro-strip detectors added to the lever arm (figure A.1). The compact telescope consisted of alternating Y- and Z-plane pixels, i.e. planes with their best resolution in the Y respectively Z direction (for a description see section 3.2.4).

For the Pb1999 setup an extra Y-plane had been added (figure A.2) at the end of the compact telescope and the lever arm consisted only out of micro-strip detectors.

In 2000 again an extra Y-plane was added in the middle of the compact telescope and in the middle of the lever arm two single-sided detectors were added (see figure A.3).

Chip efficiencies.

The efficiencies of the chips of the double sided micro-strip detectors have been determined with the PLANEFF program. Only those tracks with at least one other hit in the lever arm were taken into account. The efficiencies found are listed in table A.1.

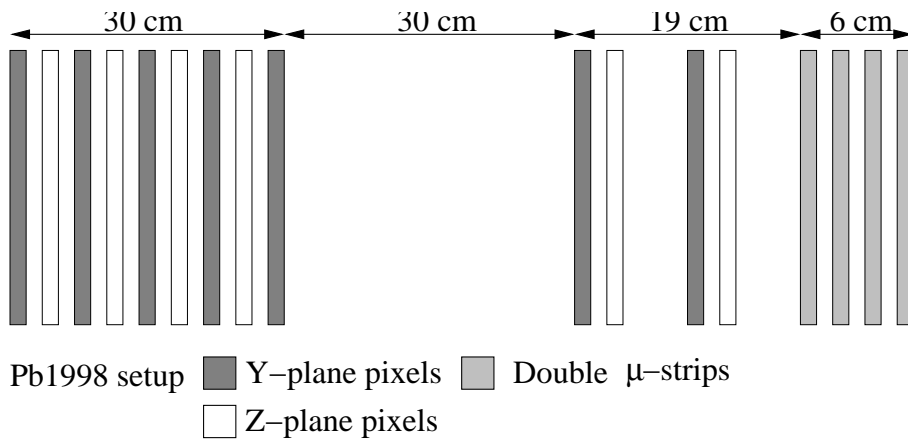


Figure A.1: Configuration of the silicon telescope for the Pb1998 setup.

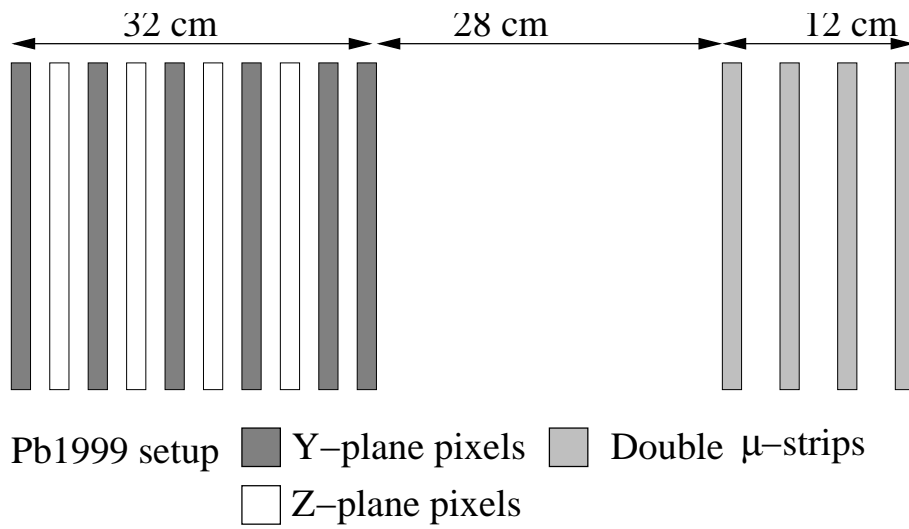


Figure A.2: Configuration of the silicon telescope for the Pb1999 setup.

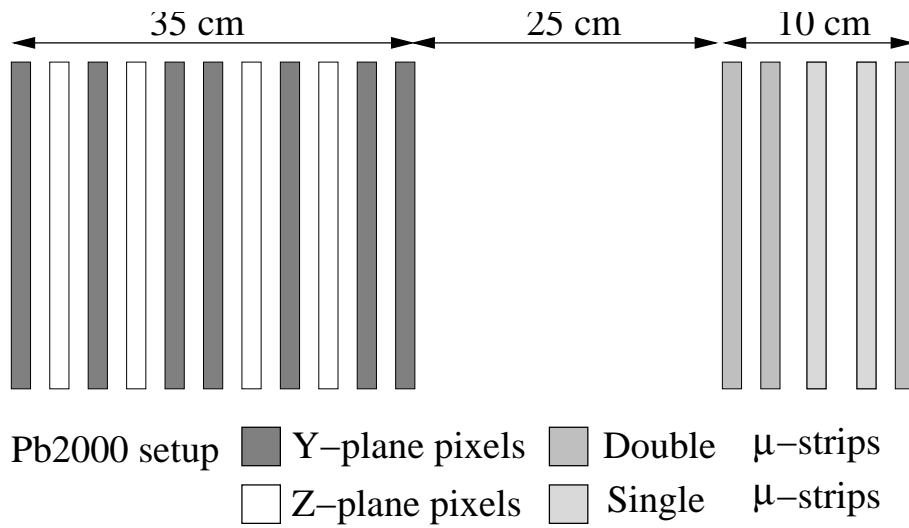


Figure A.3: Configuration of the silicon telescope for the Pb2000 setup.

Table A.1: Chip efficiencies for the detectors used in the Pb2000 run. The errors on the efficiencies listed are of the order of 0.2 %.

Detector number (side)	Eff. (%) Chip 1	Eff. (%) Chip 2	Eff. (%) Chip 3	Eff. (%) Chip 4	Eff. (%) Chip 5	Eff. (%) Chip 6
I (Front)	97.34	97.77	96.09	93.71	95.92	95.88
I (Back)	96.62	96.84	94.53	97.04	97.73	94.23
II (Front)	87.91	94.77	95.66	94.43	95.75	95.83
II (Back)	93.23	95.89	93.94	95.87	96.14	96.49
III (Front)	95.93	94.22	95.42	92.30	93.99	94.01
III (Back)	0.0	91.34	92.17	92.06	93.07	94.64

Bibliography

- [1] G. Bunce *et al.*, “ Λ^0 Polarization in Inclusive Production by 300-GeV Protons on Beryllium”, *Phys. Rev. Lett* **36**, 1113 (1976).
- [2] A.M. Smith *et al.*, “ Λ^0 Polarization in proton-proton interactions from $\sqrt{s} = 31$ to 62 GeV”, *Phys. Lett.* **185B**, 209 (1987).
- [3] B. Lundberg *et al.*, “Polarization in inclusive Λ and $\bar{\Lambda}$ production at large p_T ”, *Phys. Rev.* **D40**, 3557 (1989).
- [4] E.J. Ramberg *et al.*, “Polarization of Λ and $\bar{\Lambda}$ Produced by 800-GeV Protons”, *Phys. Lett.* **338B**, 403 (1994).
- [5] R. Bellwied *et al.*, “The measurement of transverse polarization of Λ Hyperons in relativistic heavy ion collisions”, *Nucl. Phys.* **A698**, 499 (2002).
- [6] T. Henkes *et al.*, “Further evidence for pomeron-quark interactions: observation of large Λ^0 polarizations in $pp \rightarrow (\Lambda K^+)p$ ”, *Phys. Lett.* **B283**, 155 (1992).
- [7] A.D. Panagiotou, “ Λ^0 polarization in hadron-nucleon, hadron-nucleus and nucleus-nucleus interactions”, *Int. J. Mod. Phys A* **5**, 1197 (1990).
- [8] K. Heller, “Spin and High Energy Hyperon Production, Results and Prospects”, *Proceedings of Spin 96, Amsterdam 10-14/10/96*, World Scientific, 23 (1997).
- [9] F. Antinori *et al.*, “Enhancement of Strange and Multi-Strange Baryons in Central Pb-Pb Interactions at 158 GeV/c per Nucleon”, *Nucl. Phys.* **A663**, 717c (2000).
- [10] J. Rafelski and B. Müller, “Strangeness Production in the Quark-Gluon Plasma”, *Phys. Rev. Lett* **48** (1982) 1066–1069;
P. Koch, B. Müller and J. Rafelski, “Strangeness in relativistic heavy ion collisions”, *Phys. Rep.* **142**, 167 (1986).
- [11] NA57 proposal, “Study of strange and multistrange particles in ultrarelativistic nucleus-nucleus collisions”,
CERN/SPSLC/96-40 (1996).
- [12] F.J.M. Geurts, “Neutral meson production in hot matter”,
Ph.D. thesis, Universiteit Utrecht, The Netherlands (1998), ISBN 90-393-1538-8.

- [13] A.D. Panagiotou, “ Λ^0 nonpolarization: Possible signature of quark matter”, *Phys. Rev. C* **33**, 1999 (1986).
- [14] V. Blobel, “Unfolding methods in high energy physics experiments”, Proceedings of the 1984 CERN School of Computing, CERN 85-09, 88 (1985).
- [15] A. Bravar *et al.*, “Analyzing Power Measurement in Inclusive Λ^0 Production with a 200 GeV/c Polarized Proton Beam”, *Phys. Rev. Lett.* **76**, 3073 (1995).
- [16] J. Soffer, “Is the riddle of the hyperon polarizations solved?”, Invited talk at Hyperon 99, Symposium on Hyperon Physics, Bavaria, Illinois, 27-29 Sep. 1999, hep-ph/9911373.
- [17] J. Felix, “On theoretical studies of Λ^0 polarization”, *Mod. Phys. Lett. A* **14**, 827 (1999).
- [18] C. Boros and L. Zuo-Tang, “Single spin asymmetries in inclusive high energy hadron-hadron collision processes”, *Int. J. Mod. Phys. A* **15**, 927 (2000).
- [19] S.M. Troshin and N.E. Tyurin, “Challenge of hyperon polarization”, hep-ph/0201267.
- [20] J.F. Owens, “Large-momentum-transfer production of direct photons, jets, and particles”, *Rev. Mod. Phys.* **59**, 465 (1987).
- [21] G.L. Kane, J. Pumplin and W. Repko, “Transverse Quark Polarization in Large- p_T Reactions, e^+e^- Jets, and Leptoproduction: A Test of Quantum Chromodynamics”, *Phys. Rev. Lett.* **41**, 1689 (1978).
- [22] Y. Kanazawa and Y. Koike, “Polarization in hadronic Λ hyperon production and chiral-odd twist-3 distribution”, *Phys. Rev. D* **64**, 34019 (2001).
- [23] M. Anselmino, D. Boer, U. D’Alesio and F. Murgia, “ Λ polarization from unpolarized quark fragmentation”, *Phys. Rev. D* **63**, 054029 (2001).
- [24] D. Buskelic *et al.*, “Measurement of Λ polarization from Z decays”, *Phys. Lett.* **B374**, 319 (1996).
- [25] B. Andersson, G. Gustafson and G. Ingelman, “A semiclassical model for the polarization on inclusively produced Λ^0 -particles at high energies”, *Phys. Lett.* **B 85**, 417 (1979).
- [26] T.A. DeGrand and H.I. Miettinen, “Models for polarization asymmetry in inclusive hadron production”, *Phys. Rev. D* **24**, 2419 (1981).
- [27] J.D. Jackson, “Classical Electrodynamics”, John Wiley & Sons, New York (1975).
- [28] T.A. DeGrand, J. Markkanen and H.I. Miettinen, “Hyperon polarization asymmetry: Polarized beams and Ω^- production”, *Phys. Rev. D* **32**, 2445 (1985).
- [29] G. Herrera, J. Magnin, L.M. Montaño and F.R.A. Simão, “The Λ^0 Polarization and the Recombination Mechanism”, *Phys. Lett.* **B381**, 337 (1996).
- [30] C. Boros and L. Zuo-Tang, “Hyperon Polarization and Single Spin Left-Right Asymmetry in Inclusive Production Processes at High Energies”, *Phys. Rev. Lett.* **79**, 3608 (1997).
- [31] C. Boros and L. Zuo-Tang, “Hyperon production mechanisms and single-spin asymmetry in high energy hadron-hadron collisions”, *Phys. Rev. D* **53**, R2279 (1996).

- [32] S.M. Troshin and N.E. Tyurin, “Hyperon polarization in the constituent quark model”, *Phys. Rev. D* **55**, 1265 (1997)
- [33] J.Szwed, “Hyperon polarization at high energies”, *Phys. Lett.* **B105**, 403 (1981).
- [34] G. Altarelli and G. Ridolfi, “Understanding the Proton Spin Structure: A Status Report”, *Nucl. Phys. (Proc. Suppl)* **B39**, 106 (1995).
- [35] R. Voss, “Prospects of Spin Physics at HERA”, Proceedings of the Workshop DESY-Zeuthen, Germany, 1995, edited by J. Blümlein and W.-D. Novak, Report No. DESY 95-200, 25.
- [36] A. Ayala, E. Cuautle, G. Herrera, L.M. Montaño, “ Λ^0 polarization as a probe for production of deconfined matter in ultra-relativistic heavy-ion collisions”, *Phys. Rev C* **65**, 24902 (2002).
- [37] M. Jacob and J. Rafelski, “Longitudinal $\bar{\Lambda}$ polarization, $\bar{\Xi}$ abundance and quark-gluon plasma creation”, *Phys. Lett.* **B190**, 173 (1987).
- [38] R.E. Ansorge *et al.*, “Hyperon production at 200 and 900 GeVcm energy”, *Nucl. Phys.* **B 328**, 36 (1989).
- [39] Peter van de Ven, “Centrality dependence of Λ production in Pb-Pb collisions”, Ph.D. Thesis, University of Utrecht, Netherlands 2001.
- [40] M. Campbell *et al.*, “Development of a pixel readout chip compatible with large area coverage”, *Nucl. Instr. Meth.* **A342**, 52 (1994).
- [41] E.H.M. Heijne *et al.*, “First operation of a 72 k element hybrid silicon micropattern pixel detector array”, *Nucl. Instr. Meth.* **A349**, 138 (1994).
- [42] F. Antinori *et al.*, “Experience with a 30 cm² silicon pixel plane in CERN experiment WA97”, *Nucl. Instr. Meth.* **A360**, 91 (1995).
- [43] E.H.M. Heijne *et al.*, “LHC1: A semiconductor pixel detector readout chip with internal, tunable delay providing a binary pattern of selected events”, *Nucl. Instr. Meth.* **A383** 55 (1996).
- [44] “ALICE Technical Design Report of the Inner Tracking System (ITS)”, CERN/LHCC/99-12, 175 (1999).
- [45] F. Antinori *et al.*, “A new VME trigger processor for the NA57 experiment”, Proceedings of *Electronics for LHC experiments*, London (1997) 364–368.
- [46] F. Antinori *et al.*, “The NA57 trigger processor”, Proceedings of *Electronics for LHC experiments*, Rome (1998) 331–336.
- [47] Integrated Detector & Electronics (IDE) AS, “The VA circuit”.
- [48] O. Toker *et al.*, “VIKING, a CMOS low noise monolithic 128 channel frontend for Si-strip detector readout”, *Nucl. Instr. Meth.* **A340**, 572 (1994).
- [49] R. Turchetta, “Spatial resolution of silicon microstrip detectors”, *Nucl. Instr. Meth.* **A335**, 44 (1993).

- [50] E.H. Smith and G.R. Kalbfleisch, “Double-sided silicon charge correlation study: matching multiple track hits”, Nucl. Instr. Meth. **A371**, 428 (1996).
- [51] P.C. de Rijke, “Performance of the microstrip detectors in the NA57 experiment for the lead-99 run”, Student thesis, Universiteit Utrecht, The Netherlands (2001).
- [52] J.-C. Lassalle, A. Michalon and H. Helstrup, “ORHION User’s guide & Reference manual”, Internal note (1999).
- [53] J.-C. Lassalle, “The ST processor of ORHION; User’s guide & Reference Manual”, Internal note (1994).
- [54] CERN program library, “The ZEBRA System”, CERN Program Library Long Writeups Q100 and Q101 (1995).
- [55] H. Wind, “Momentum analysis by using a quintic spline model for the track”, Nucl. Instr. Meth. **115** (1974) 431–434.
- [56] CERN program library, “GEANT: Detector Description and Simulation Tool”, CERN Program Library Long Writeup W5013 (1993).
- [57] CERN program library, “HEPDB: Database Management Package”, CERN Program Library Long Writeup Q180 (1995).
- [58] J. Podolanski and R. Armenteros, “Analysis of V-Events”, Phil. Mag. **45**, 13 (1954).
- [59] P. Norman, “Hyperon production in p-Be interactions at 158 AGeV/c per nucleon at the WA97 CERN experiment”, Ph.D. thesis, University of Birmingham, U.K. (1999).
- [60] G.E. Bruno, “Studio della produzione di particelle strane e della dinamica di espansione in collisioni nucleari ultra-relativistiche all’SPS”, Ph.D. thesis, University of Bari, Italy (2002).
- [61] G.E. Bruno *et al.*, “Results on Λ and Ξ production in Pb-Pb collisions at 160 GeV/c per nucleon from the NA57 experiment”, to be published in the Proceedings of *The XXXVII Rencontres de Moriond on QCD and High Energy Hadronic Interactions*, hep-ex/0207047 (2002).
- [62] E. Andersen *et al.*, “Study of strangeness enhancement in lead-lead collisions at the CERN SPS”, Proceedings of *International Symposium on Multiparticle Dynamics*, Delphi (1998).
- [63] F. Antinori *et al.*, “Determination of the event centrality in the WA97 and NA57 experiments”, Proceedings of *Strangeness 2000*, Berkely (2000).
- [64] N. Carrer *et al.*, “Determination of the number of wounded nucleons in Pb+Pb collisions at 158 AGeV/c”, Nucl. Phys. **A661**, 357 (1999).
- [65] C.-Y. Wong, “Introduction to High-Energy Heavy-Ion Collisions”, World Scientific Publishing, Singapore (1994) 251–264.
- [66] A. Bialas, M. Bleszyński and W. Czyż, “Multiplicity distributions in nucleus-nucleus collisions at high-energies”, Nucl. Phys. **B111**, 461 (1976).

-
- [67] F. Antinori *et al.*, “Transverse mass spectra of strange and multi-strange particles in Pb-Pb collisions at 158 AGeV/c”, *Eur. Phys. J.* **C14**, 633 (2000).
- [68] E. Andersen *et al.*, “Strangeness enhancement at mid-rapidity in Pb-Pb collisions at 158 AGeV/c”, *J. Phys.* **G25**, 181 (1999).
- [69] F. Antinori *et al.*, “First results on strange baryon production from the NA57 experiment”, *Proceedings of Quark Matter 2001*, Long Island (2001).
- [70] K. Fanebust *et al.*, “Results on hyperon production from CERN NA57 experiment.”, *J. Phys.* **G28**, 1607 (2002).
- [71] V. Manzari *et al.*, “Status of the NA57 experiment at CERN SPS.”, *J. Phys.* **G27**, 383 (2001).
- [72] T.D.Lee *et al.*, “Possible Detection of Parity Nonconservation in Hyperon decay”, *Phys. Rev.* **106**, 1367 (1957).
- [73] Particle Data Group, *Phys. Rev.* **D 54**, 1 (1996).
- [74] E.Quercigh, private communication.

Summary

In this thesis the production and polarization of Λ particles produced in Pb-Pb collisions at a beam energy of 158 GeV/c per nucleon are studied. In these collisions nuclear matter is compressed and heated and under these conditions it is possible that a quark-gluon plasma (QGP) is created. In a QGP the boundaries between individual particles disappear and the quarks and gluons can move around freely. One of the probes to study the creation of the QGP is the so-called *Strangeness Enhancement*, which is the enhanced production of strange particles, with respect to the production in proton-induced collisions. Another proposed signature of the QGP is the disappearance of transverse Λ polarization around mid-rapidity. Transverse Λ polarization can occur when the spin of the produced Λ has its preferred direction perpendicular to the production plane. In proton-proton and proton-nucleus collisions a negative transverse polarization has been observed and its magnitude was largest for the Λ s produced in the direction of the beam (i.e. at high x_F). This is an indication that the projectile plays an important role and in semi-classical models the following picture is assumed: in the interaction region a spin-zero ud-diquark from the projectile recombines with a negatively polarized s-quark from the sea. This s-quark also gives transverse momentum (p_T) to the Λ and as a result the polarization is dependent on p_T . Recently it has been shown that also in nucleus-nucleus collisions a negative transverse polarization occurs, so even in large interaction regions the information on the nature of the projectile is kept. In a QGP however this information is lost and no production plane can be defined. This will cause the transverse polarization of the Λ s produced in this region to disappear.

The NA57 experiment at CERN has been designed to measure the production of strange particles in Pb-Pb and p-Be collisions, at the beam energies of 40 and 158 GeV/c per nucleon (provided by the SPS accelerator). In this way the evolution of the strangeness enhancement pattern as a function of the beam energy can be studied. Furthermore the dependence of the enhancement on the interaction volume is investigated by scanning the *centrality* range. The word *centrality* denotes a measure of the type of collision, which ranges from peripheral (glancing collisions) to central (head-on collisions). This scan was already performed by the predecessor of NA57, the WA97 experiment. In this experiment strangeness enhancement was seen in Pb-Pb collisions at 158 AGeV/c, where only collisions with more than 80 participating nucleons were regarded. The NA57 experiment can extend the centrality range by measuring collisions with as few as 40 participating nucleons.

In the experiments performed in 1999 (Pb-Pb collisions at 40 AGeV/c) and 2000 (Pb-Pb collisions at 158 AGeV/c) the experimental setup consisted of double-sided silicon micro-strip de-

tectors, which were developed and built at the institute of Sub Atomic Physics at Utrecht University/NIKHEF. These detectors were prototypes for detectors which will be used in the ALICE experiment. In this thesis the performance of the detectors in the experiments of 1999 and 2000 has been studied. The detectors are shown to have worked with an efficiency of 94-96% per side. When information of the strips (which have a pitch of $95\mu\text{m}$) on the sides is combined three-dimensional points can be constructed and the track residuals of these points are shown for the different detectors to have a resolution of 20 to $28\mu\text{m}$ in the bending direction of the particles. The effect of the inclusion of the lever arm with micro-strip detectors in the data analysis causes the resolution of the invariant mass distributions of strange particles with only two oppositely charged decay tracks to improve with 15-20%.

Another study performed in this thesis is on the production of the Λ , $\bar{\Lambda}$ and K_S^0 particles. This is done by measuring the transverse mass distributions, which are fitted with an exponential function, in order to calculate the inverse slope parameters. However since the directly measured transverse mass distributions are distorted, due to the small acceptance of the Silicon Telescope and selection cuts, they have to be corrected first. This is done by using a deconvolution method, which also takes into account the limited resolution of the detectors. With this method the full statistics was used and the inverse slope parameters as a function of centrality were calculated. The results are compatible with earlier results of NA57, where the statistical error was a factor of 10 larger. Furthermore particle yields are calculated by integrating the corrected momentum distributions and the results for the yields presented in this thesis also show improved errors.

Finally the transverse polarization of the produced Λ s has been measured, where also the deconvolution method was applied. An analysis of the asymmetry of the K_S^0 mesons shows that the measurement of the transverse polarization is very sensitive to the geometry and the knowledge of the detector setup, which hence is the dominant source of the systematic uncertainty. The transverse Λ polarization has been determined around two values of x_F : for $x_F = 0.09$ a value of $+0.6^{+7.4}_{-6.6}\%$ was found and at $x_F = 0.14$ a value of $+5.5^{+8.9}_{-7.4}\%$, where the errors are the combined statistical and systematic error. The latter result is compatible with zero polarization and it seems to favor the Berlin Model. Unfortunately the error is too large to exclude other semi-classical models (which predict a polarization of - 5 to -7%) or to make a statement about the creation of a QGP. However this is the first time that a measurement was done in this region and with this collision system. Keeping these results in mind it would be interesting to see what is the value of the transverse polarization of the Λ s measured by NA57 in Pb-Pb collisions at a lower beam energy of $40\text{ AGeV}/c$. This would not only give results in the same region as measured in this thesis, but it would enable a measurement up to $x_F \sim 0.35$, where polarizations of the order of 10-15% are expected.

Samenvatting

In dit proefschrift zijn de productie en polarisatie van Λ deeltjes bestudeerd, die zijn geproduceerd bij een bundelenergie van $158 \text{ GeV}/c$ per nucleon. In deze botsingen wordt de nucleaire materie samengedrukt en verwarmd, en onder deze omstandigheden is het mogelijk dat een Quark-Gluon Plasma (QGP) gecreëerd wordt. In een QGP verdwijnen de grenzen tussen de individuele deeltjes waardoor de quarks en de gluonen dan vrij kunnen bewegen. Een van de peilers om de creatie van het QGP te bestuderen is de zogenaamde *Vreemdheidstoename*, wat de toename in de productie van vreemde deeltjes inhoudt, ten opzichte van de productie in proton-geïnduceerde botsingen. Een andere voorgestelde aanwijzing voor de creatie van het QGP is de verdwijning van transversale Λ polarisatie rond midden-rapiditeit. Transversale Λ polarisatie kan voorkomen als de spin van de geproduceerde Λ zijn voorkeursrichting loodrecht op het productievlak heeft. In proton-proton en proton-nucleus botsingen is een negatieve transversale polarisatie gemeten, die de grootste waarde had wanneer de Λ 's waren geproduceerd in de richting van de bundel (dat is bij hoge x_F). Dit is een indicatie dat het projectiel een grote rol speelt en in semi-klassieke modellen wordt het volgende concept aangenomen: in het interactiegebied recombineert een spin-nul u-diquark van het projectiel met een negatief gepolariseerde s-quark van de zee. Dit s-quark geeft de Λ tevens een transversale impuls p_T en dit resulteert in een polarisatie die afhankelijk is van p_T . Recentelijk is het aangetoond dat ook in nucleus-nucleus botsingen een negatieve transversale polarisatie optreedt, wat impliceert dat zelfs in grote interactiegebieden de informatie aangaande de aard van het projectiel behouden wordt. In een QGP gaat deze informatie echter verloren en kan er geen productievlak gedefinieerd worden. Dit zorgt ervoor dat de transversale polarisatie van de Λ 's, die in dit gebied geproduceerd zijn, verdwijnt.

Het NA57 experiment op CERN is ontworpen om de productie van vreemde deeltjes in Pb-Pb en p-Be botsingen te meten, bij verschillende bundelenergieën van 40 en $158 \text{ GeV}/c$ per nucleon (geleverd door de SPS versneller). Op deze manier kan de evolutie van het vreemdheidstoenamepatroon als functie van de bundelenergie bestudeerd worden. Verder wordt de afhankelijkheid van de toename van het interactievolume onderzocht door het *centraliteitsgebied* te scannen. Het begrip centraliteit geeft een maat van de soort botsing, die kan variëren van perifeer (schappende botsingen) tot centraal (frontale botsingen). Deze scan was al uitgevoerd door de voorganger van NA57, het WA97 experiment. In dit experiment was vreemdheidstoename gezien in Pb-Pb botsingen bij $158 \text{ AGeV}/c$ waar alleen botsingen met meer dan 80 deelnemende nucleonen beschouwd werden. Het NA57 experiment kan het centraliteitsgebied uitbreiden door botsingen te meten met het kleinere aantal van 40 deelnemende nucleonen.

In de experimenten gedaan in 1999 (Pb-Pb botsingen bij $40 \text{ AGeV}/c$) en 2000 (Pb-Pb botsingen bij $158 \text{ AGeV}/c$) zijn dubbelzijdige silicium detectoren aan de experimentele opstelling toegevoegd, die ontwikkeld en gebouwd zijn op het Instituut voor Subatomaire Physica van de Universiteit Utrecht/NIKHEF. In dit proefschrift zijn de verrichtingen van de detectoren in de experimenten van 1999 en 2000 bestudeerd. Het is aangetoond dat deze detectoren hebben ge-functioneerd met een efficiëntie van 94 tot 96% per kant. Als de informatie van de strips (met een breedte van $95 \mu\text{m}$) van de beide zijden gecombineerd wordt, kunnen driedimensionale punten gemaakt worden. Het is aangetoond, voor wat betreft de verschillende gebruikte detectoren, dat de deeltjesbaanresiduen van deze punten een resolutie hebben van 20 tot $28 \mu\text{m}$ in de buigrichting van de deeltjes. De toevoeging van de lever arm met microstrip detectoren in de analyse zorgt voor een verbetering van 15 tot 20% in de resolutie van de invariante massaverdelingen van vreemde deeltjes met slechts twee tegenovergestelde deeltjesbanen.

Een andere studie, gepresenteerd in dit proefschrift, gaat over de productie van Λ , $\bar{\Lambda}$ en K_S^0 deeltjes. Deze productie wordt gemeten door de transversale massaverdelingen te bepalen, die gefit worden met een exponentiële functie, waarmee de reciproke hellingswaarde (hellingsparameter) berekend kan worden. Daar de direct gemeten transversale massaverdelingen echter veranderd zijn door de kleine acceptantie van de Silicium Telescoop en selectiesneden, zijn ze eerst gecorrigeerd. Dit is gedaan door een deconvolutiemethode te gebruiken, die ook rekening houdt met de beperkte resolutie van de detectoren. Met deze methode zijn alle aanwezige data gebruikt en de hellingsparameters als functie van de centraliteit zijn berekend. De resultaten zijn verenigbaar met eerdere resultaten van NA57, die echter een statistische fout hadden van een factor 10 groter. Tevens zijn deeltjesopbrengsten berekend door de gecorrigeerde transversale massaverdelingen te integreren en ook de resultaten voor de deeltjesopbrengsten laten kleinere fouten zien.

Als laatste is de transversale polarisatie van de geproduceerde Λ hyperonen bepaald, waarbij ook de bovenstaande deconvolutiemethode werd toegepast. Een analyse van de asymmetrie van de K_S^0 mesonen laat zien dat de meting van de transversale polarisatie erg gevoelig is voor de geometrie van de opstelling, die aldus de dominante oorsprong van de systematische onzekerheid is. De transversale polarisatie is bepaald rond twee waarden van x_F : op $x_F = 0.09$ werd een waarde van $+0.6 \begin{smallmatrix} +7.4\% \\ -6.6\% \end{smallmatrix}$ gevonden en op $x_F = 0.14$ een waarde van $+5.5 \begin{smallmatrix} +8.9\% \\ -7.4\% \end{smallmatrix}$, waarin de statistische en systematische fouten gecombineerd zijn. Het laatste resultaat is verenigbaar met een polarisatie van nul en dit lijkt het Berlijn Model te begunstigen. Ongelukkigerwijs is de fout te groot om andere semi-klassieke modellen (die een polarisatie van -5 en -7% voorspellen) uit te sluiten of om een uitspraak te doen over de creatie van een QGP. Dit is echter de eerste keer dat een meting in dit gebied en met dit botsingssysteem is gedaan. Met deze resultaten in gedachte zou het interessant zijn om te zien wat de transversale polarisatie van de Λ 's is, die gemeten zijn door NA57 in Pb-Pb botsingen bij een lagere bundelenergie van $40 \text{ AGeV}/c$. Dit zou niet alleen resultaten opleveren in hetzelfde gebied, als onderzocht in dit proefschrift, maar het zou ook mogelijk zijn om tot $x_F \sim 0.35$ te meten, alwaar polarisaties van de orde van 10-15% zijn gemeten.

Dankwoord

Het doen van een promotieonderzoek en het schrijven van het proefschrift is geen gemakkelijke opgave geweest. Ik heb gedurende mijn onderzoek dan ook de hulp van veel mensen gehad. Bij deze zou ik graag iedereen willen bedanken die me de laatste jaren geholpen en gesteund heeft.

Ten eerste zou ik graag mijn promotor René Kamermans willen bedanken. Zijn advies is vaak belangrijk geweest bij het op de rails krijgen en vooral houden van dit onderzoek. Welke problemen ik ook weer tegenkwam (en dat waren er toch wat, en niet alleen op werktechnisch vlak), na een gesprek met hem leken ze altijd opeens minder erg en kon ik er weer tegen aan. Paul Kuijer, mijn dagelijkse begeleider, wil ik vooral bedanken voor het enthousiasme en de expertise waarmee hij me begeleidt heeft. De vele inhoudelijke gesprekken en discussies over met name Λ polarisatie hebben mijn analyse vorm gegeven en mijn begrip van deze complexe materie vergroot. Daarnaast wil ik de technici binnen de vakgroep SAP bedanken: Arie de Haas, Kees Oskamp, Ton van den Brink, Dirk Balke en Marco Voerman. Door hun inspanningen hebben we uiteindelijk met goed functionerende detectoren kunnen meten. Ik zal nooit vergeten dat bij het belangrijke experiment in 2000 onze beste detector door een ongeluk was gebroken. Binnen een recordtijd van drie dagen (inclusief retourtje Strasbourg) is er toen een nieuwe detector in elkaar gezet, die uiteindelijk het best heeft gefunctioneerd.

Since I was working in the NA57 collaboration many people have contributed to my work. First I would like to thank Federico Antinori, Vito Manzari and Domenico Elia, who as run coordinators helped me during the experimental run periods. For the work on the micro-strips I owe many thanks to Alain Michalon, who helped me in a very difficult period and who kept me going. The work done for the implementation of the micro-strips in ORHION is mainly from his hand. Merci et bien cordialement! For the deconvolution of the data I used a program developed by Roman Lietava. For the opportunity to use his program and also for his help in the understanding of the deconvolution principles I would like to thank him. I also want to thank Emanuele Quercigh for our discussions on Λ polarization, which have increased my understanding of the analysis. For many helpful comments on general NA57 stuff I am indebted to Adam Jacholkowski and Giuseppe Bruno.

Tijdens mijn promotie heb ik ook hulp gehad van verscheidene studenten: Han, PC en Joeri, bedankt! Verder was Nick van Eijndhoven nooit te beroerd om mijn vragen op uiteenlopend vlak te beantwoorden. Ik wil tevens de leescommissie, bestaande uit Thomas Peitzmann, Paul Kooijman en Gerard van der Steenhoven, bedanken voor het corrigeren van mijn proefschrift. Zij hebben me laten zien dat dingen niet altijd zo vanzelfsprekend zijn als ze lijken en hebben daarnaast nog vele kleine foutjes eruit gehaald. Aangaande het proefschrift zelf moet ik ook Garnt hartelijk bedanken voor zijn inspanningen de omslag zo mooi te krijgen, als hij nu is.

Ik heb een leuke tijd gehad bij de vakgroep Subatomaire Physica en daar hebben veel mensen

aan bijgedragen. Ten eerste zijn daar mijn collega AIO's/OIO's: Peter van de Ven, Peter (PC) de Rijke, Garmt de Vries, Eugène van der Pijll, Alexey Sokolov, Hernan Wahlberg en Dani Muigg (was al post-doc). Ik heb met Peter van de Ven veel meegemaakt gedurende de eerste twee jaren. Zo zaten we bij de vele bezoeken aan CERN en bij conferenties veel met elkaar opgescheept, maar dat heb ik altijd als zeer leuk ervaren. Als overzicht van mijn minder professionele ervaringen met jou kom ik al snel op de volgende woorden: groene haren, champagnedouche (die ik notabene betaald had), een gedeeld bed in San Francisco (gelukkig zijn die Amerikaanse bedden groot), een 'geverfde' auto, een astma-aanval en een broodje haring met pinda saus. Helaas brengt onze gezamenlijke interesse ook onze grootste tegenstelling aan het licht: je mag dan wel uit Eindhoven komen, het blijft een prutsclub vol boeren en ja, dat kratje krijg je ooit nog wel eens. Ook PC heeft veel lief en leed gedeeld tijdens de experimenten en andere NA57 beslommeringen. Gelukkig kon ik de ellende altijd met hem wegspoelen middels een biertje. Tevens heeft hij samen met Garmt de laatste maanden van de promotie mijn geklaag aan moeten horen, wat ze altijd geduldig hebben gedaan. Gelukkig heeft Garmt altijd een positieve vrolijke levensinstelling die een goede compensatie was voor mijn gemoed.

Een andere groep collega's die voor een leuke sfeer gezorgd hebben zijn de technici (waartoe naast de eerder genoemde mensen ook Jan en Leo behoren). Zij zijn het kloppend hart van de vakgroep en de koffie- en thee-pauzes waren altijd een prettig rustmoment op de dag. Verder hebben de begrijpende, maar ook gemene, grijnzen als ik weer eens met wallen, na een slapeloze nacht, bij de koffie verscheen me stiekem toch goed gedaan. Ik zal zeker de vele discussies met Kees over ons beider liefde, Ajax, missen (nee, de scheidsrechter heeft het niet altijd gedaan!). Het bezoeken van een wedstrijd van de beste club van Nederland gaat er zeker nog van komen. Helaas kan Dirk dit proefschrift niet meer zien. Zijn dood was een dieptepunt tijdens mijn promotie.

Een bijzondere rol tijdens mijn promotie was weggelegd voor de secretaresses Astrid en Birgit. Zij zijn op emotioneel vlak altijd een steun geweest en waren altijd beschikbaar voor een gezellig praatje. Met Birgit ging dat dan vaak over onze gezamenlijke achtergrond in de kunstgeschiedenis: een leuke afwisseling in het exacte geweld.

Leuke herinneringen bewaar ik ook aan mijn bezoeken aan CERN. De vele gestationeerde AIO's/OIO's hebben voor veel leuke afleiding gezorgd naast het intensieve werk. Nick, Ivo, Martin, Robert, Simon, Henrique, Vinod, Mark, Cathelijne, Rutger, Rutger, Joost, Marco, Sandra en Niels, bedankt voor de gezellige avonden! Met Nick van Remortel was het altijd leuk om onze culinaire interesse te delen, alhoewel zijn kwaliteiten ook op een ander vlak lagen, gezien de zelfbenoemde titel 'nachtburgemeester van St. Genis'. Met Ivo heb ik vanaf het eerste studiejaar veel samen meegemaakt en gedurende het hele traject heb ik altijd veel steun van hem gehad (*Het zijn toch allemaal...*), vaak ook in de vorm van een biertje (of twee....). Verder wil ik hier mijn vrienden van het natuurkundedispuut *Kwarck* bedanken voor de vele jaren buitenfysisch plezier: Tjan, Cel en in het bijzonder mijn paranimfen Sjoerd en Tommie.

Het opvoeden van kinderen en een promotieonderzoek doen is niet de gemakkelijkste combinatie. Daarom zou ik graag Joke en Jacques willen bedanken, aangezien zij vaak hielpen de dagelijkse beslommeringen te verlichten, en er meer ruimte voor het onderzoek kwam. Ook wil ik mijn ouders en andere vrienden bedanken.

Tenslotte kom ik bij de belangrijkste persoon. Nazan, ik weet dat het niet alleen voor mij op momenten afzien geweest is, maar jij bent altijd een geluksfactor in mijn leven geweest. Daarmee heb je me geholpen door de problemen van de promotie heen te bijten. Ik hoop je daar ooit nog eens voor te bedanken, al dan niet in de vorm van die lekkere luiervakantie op een exotisch eiland.

Curriculum Vitae

Ik ben op 24 mei 1973 geboren in Maastricht, waar ik de rest van mijn jeugd heb doorgebracht. Aan alle onschuld komt een einde! En zeker toen ik mijn eindexamen deed in 1991 aan het Sint Maartenscollege. In datzelfde jaar ben ik begonnen aan de studie Natuurkunde aan de Universiteit Utrecht. Nadat ik mijn propedeuse heb gehaald in 1993 besloot ik de richting experimentele natuurkunde in te slaan. Mijn afstudeeronderzoek heb ik gedaan bij de vakgroep Subatomaire Physica, waar ik deel uitmaakte van de HARP-groep. Namens deze groep heb ik meegedaan met het commissioning experiment. Uiteindelijk heb ik een scriptie geschreven over de werking van de scintillatoren tijdens dit experiment 'Calibration of the HARP Calorimeter'. In 1997 ben ik vervolgens afgestudeerd. Via SAP ben ik ook zomerstudent geweest op CERN. De twee maanden bij het experiment OPAL hebben grote indruk op me gemaakt en ik heb daar een leerzame en leuke tijd gehad.

In 1992 ben ik naast Natuurkunde begonnen vakken te volgen bij de studie Kunstgeschiedenis. Van het een kwam het ander en na een excursie naar Florence was ik helemaal verkocht. Ik heb de richting Beeldende Kunst gevolgd en heb uiteindelijk, na mijn afstuderen bij Natuurkunde, een afstudeeronderzoek gedaan naar de invloed van de techniek van de frescoschildering op de compositie. Dit resulteerde in de scriptie 'Fresco's en compositie'. Als onderdeel van dit onderzoek ben ik drie maanden naar het NIKI in Florence geweest. Uiteindelijk ben ik in 1998 ook in de Kunstgeschiedenis afgestudeerd, waarna ik meteen ben begonnen als OIO bij de vakgroep SAP.

Mijn tijd bij SAP stond in het teken van het experiment NA57 op CERN, dat zware ionenbotsingen bestudeert. Ik heb van 1998 tot 2001 actief deelgenomen aan de experimenten, waar ik me ook intensief met de data-analyse van de genomen data heb bezig gehouden. Vanaf 2001 heb ik een afsluitend onderzoek gedaan naar Lambda polarisatie waarvan de resultaten in dit proefschrift beschreven staan. Als OIO hebben zich ook op het persoonlijk vlak veel veranderingen voorgedaan. Zo werd ik aan het begin van mijn promotie verliefd op Nazan. Nu, een paar jaar later, ben ik met haar getrouwd en hebben we twee bloedjes van kinderen, Jasmijn en Oscar.